

Chapter 5

Shock Wave Focusing in Gases



5.1 Introduction

The two-dimensional shock wave focusing is divided into two patterns: the reflection from concave walls and; the convergence of curved incident shock waves, which is called implosion. This is a reverse process of an explosion.

Three-dimensional shock wave focusing is also defined: convergence of a reflected planar shock wave from a concave wall. However, the implosion of a spherical shock wave is, from engineering point of view, difficult to conduct. In 1989 a workshop on shock wave focusing was organized inviting well known researchers in those days. Ten specialists presented their current works on the topics Takayama (1990).

5.2 Two-Dimensional Focusing

5.2.1 Circular Wall

Figure 5.1a–m shows the focusing of reflected shock waves from a 60 mm diameter circular wall installed in the 40 mm × 80 mm conventional shock tube for $Ms = 1.25$ in atmospheric air at 297.0 K. The visualization was conducted in 1980 by a direct shadowgraph. The focusing process strongly depends on the wall shapes, Ms and γ .

The reflection pattern follows all the types of shock wave reflection: at first it is a DiMR including a vNMR and a SMR; it transits to a StMR; and lastly it becomes a IvMR Courant and Friedrichs (1948). With the increase in the wall angle θ_w , the IvMR terminates to a supersonic regular reflection, a SPRR which accompanies a secondary TP as seen in Fig. 5.1a. Figure 5.1d is the enlargement of Fig. 5.1c. The secondary triple point TP, the curved secondary MS and the SL are reflected from the curved wall. In Fig. 5.1, the shock wave reflected from the edge of the concave

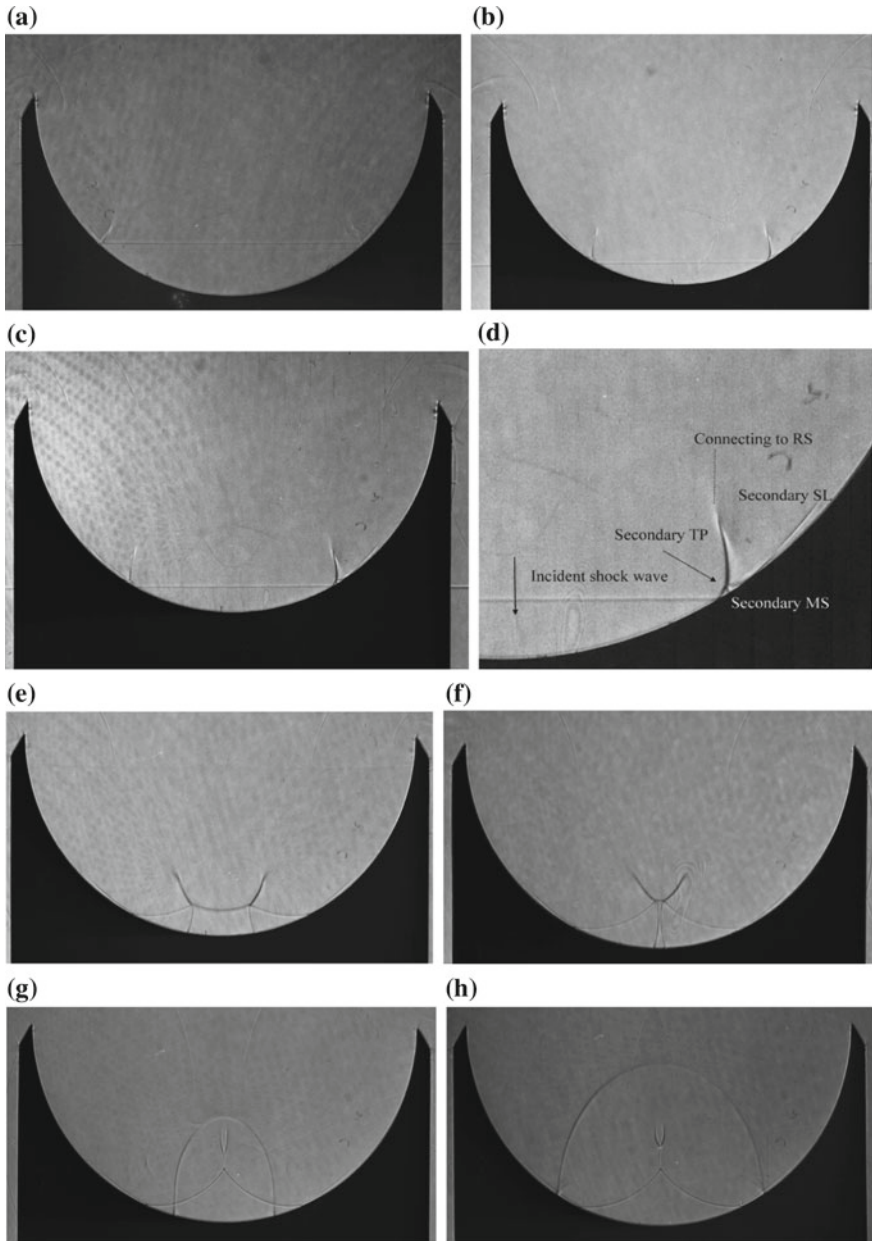


Fig. 5.1 Sequential observation of the focusing from a 60 mm diameter circular wall for $Ms = 1.25$ in atmospheric air at 297.0 K, direct shadowgraph: **a** #80082908, 100 μs from trigger point; **b** #80082909, 100 μs , $Ms = 1.220$; **c** #80082911, 110 μs , $Ms = 1.219$; **d** enlargement of (c); **e** #80082912, 130 μs , $Ms = 1.219$; **f** #80082906, 140 μs , $Ms = 1.218$; **g** #80082905, 160 μs , $Ms = 1.218$; **h** #80082904, 180 μs , $Ms = 1.218$; **i** enlargement of (h); **j** #80082901, 200 μs , $Ms = 1.218$; **k** enlargement of (j); **l** #80082902, 220 μs , $Ms = 1.218$; **m** #80082903, 240 μs , $Ms = 1.218$

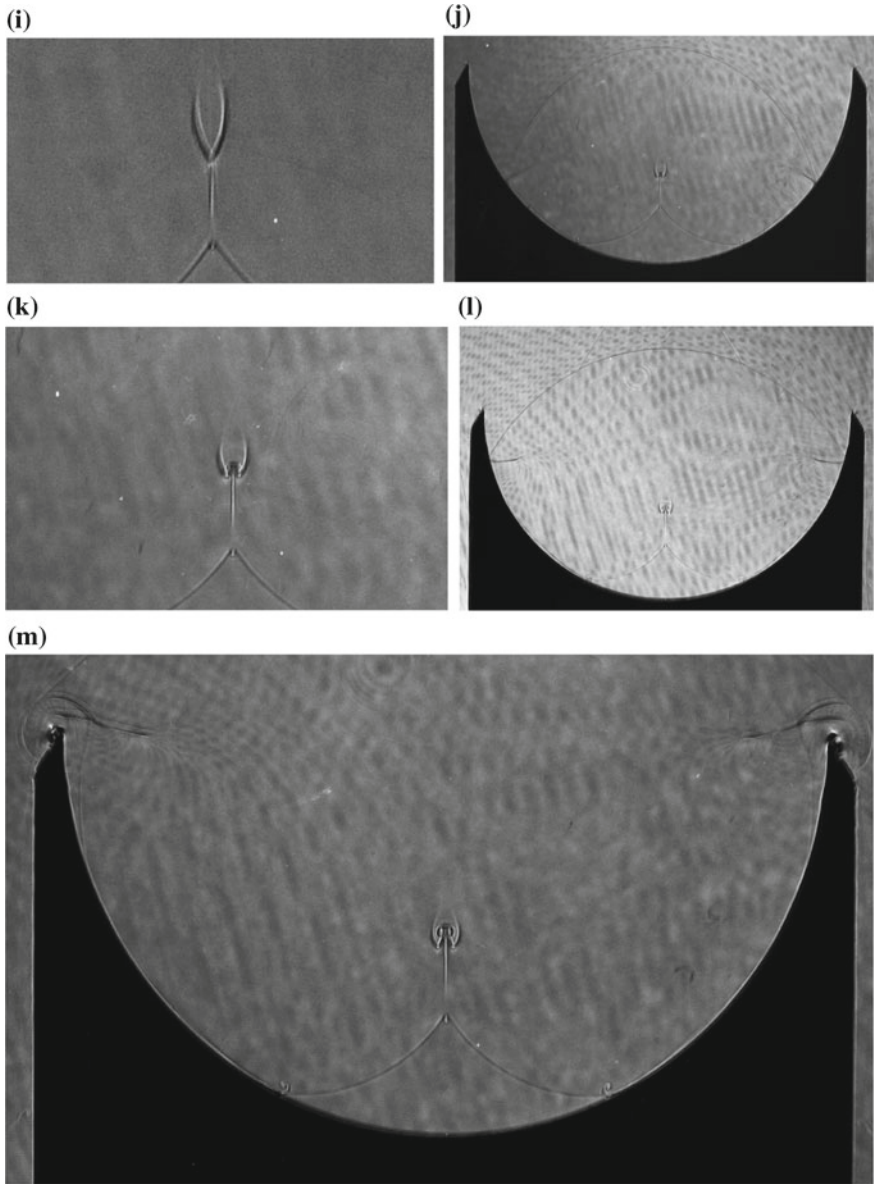


Fig. 5.1 (continued)

wall is so weakened that it is invisible. In the interferograms, the reflected shock wave is visible. In Fig. 5.1e, f, the secondary TP merged at the center and became stagnant. The vortices emanating from the second TP merged and at the same time the dissipation started which smeared out the energy accumulation. In Fig. 5.1i–m,

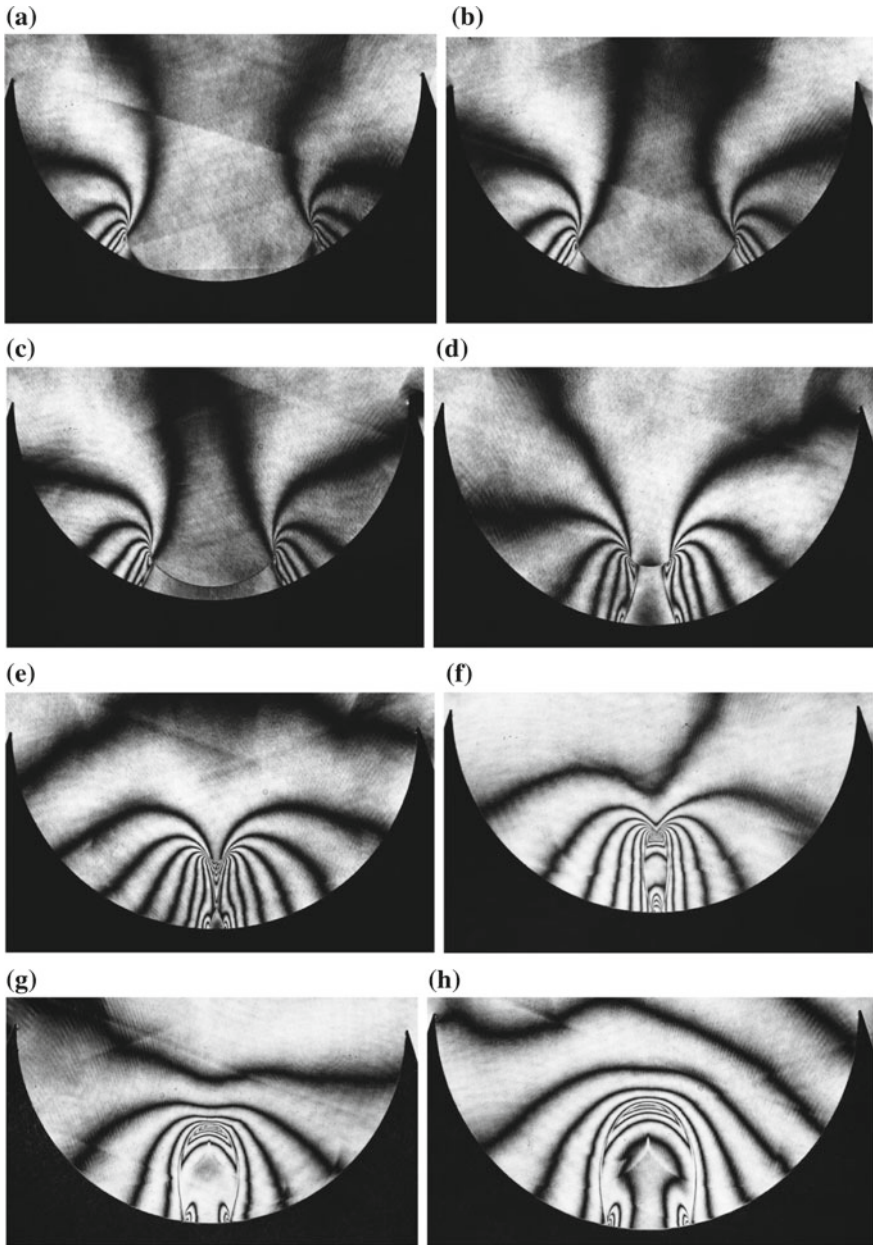


Fig. 5.2 Shock wave focusing from a 120 mm diameter circular wall for $Ms = 1.07$ in atmospheric air at 287.0 K: **a** #86030516, 370 μs from the trigger point, $Ms = 1.072$; **b** #86030515, 380 μs , $Ms = 1.074$; **c** #86030514, 300 μs , $Ms = 1.077$; **d** #86030510, 430 μs , $Ms = 1.070$; **e** #86030511, 440 μs , $Ms = 1.073$; **f** #86030602, 450 μs , $Ms = 1.071$; **g** #86030604, 470 μs , $Ms = 1.072$; **h** #86030605, 480 μs , $Ms = 1.072$; **i** #86030609 550 μs , $Ms = 1.075$; **j** #86030611, 650 μs , $Ms = 1.068$

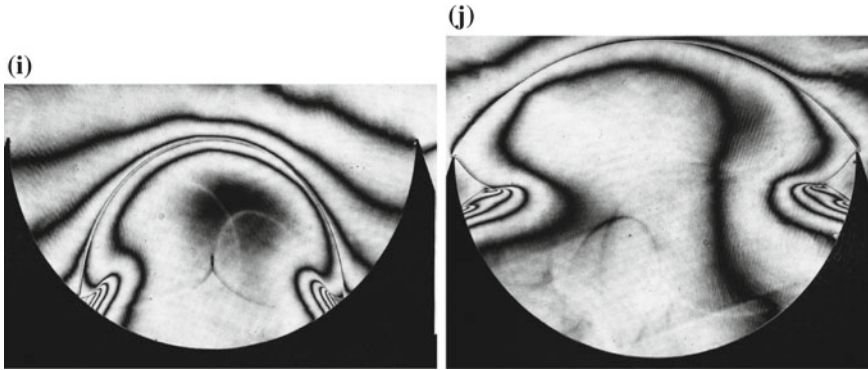


Fig. 5.2 (continued)

the contrast of slip lines emanating from the TP became faint showing the dissipation of density jump across the SL. The time attached to individual figures indicates the delay time when the second exposure was conducted. The trigger point was the position the pressure transducer was installed at some distance before the test section.

Figure 5.2 shows the evolution of shock wave focusing from a 120 mm diameter circular reflector installed in the 60 mm \times 150 mm conventional shock tube for $M_s = 1.07$ in atmospheric air. Figure 5.2a–c shows a SPRR and its reflection. Figure 5.2d–f shows the intersection of the secondary triple points and their merger with the secondary Mach stems. The reflection pattern leaning steeply forward is SuRR in Fig. 5.2j. In Fig. 5.2h, i, the remains of the slip lines SL is visible. The density jump across the SL gradually disappears. The pressures and the density focused at the area at which fringes concentrated but the temperature was not necessarily high.

Figure 5.3 shows sequentially shock wave focusing for $M_s = 1.47$ in air. Experiments were conducted in a 60 mm \times 150 mm conventional shock tube. Figure 5.3a shows a reflection of a SPRR from the circular wall. The two triple points just reflected at the center and the curved secondary Mach stems are moving outward in Fig. 5.3b. The merger of the secondary TP and the secondary Mach stems created the intersection of the slip lines. The waves are moving outward as seen in Fig. 5.3c–f. The slip lines merged and formed the vortices accumulation at a localized spot as seen in Fig. 5.3c–f. The accumulation of vortices is disconnected from the wave motion and is stagnant in a localized area as seen in Fig. 5.3g–j. The initial sharply accumulated fringe distribution became loosed and the fringe number decreased with the elapsed time as seen in Fig. 5.3g–j. During these wave interactions, the pressure just fluctuates and nearly constant and the fringe number also unvaried. Hence the temperature did not increase high.

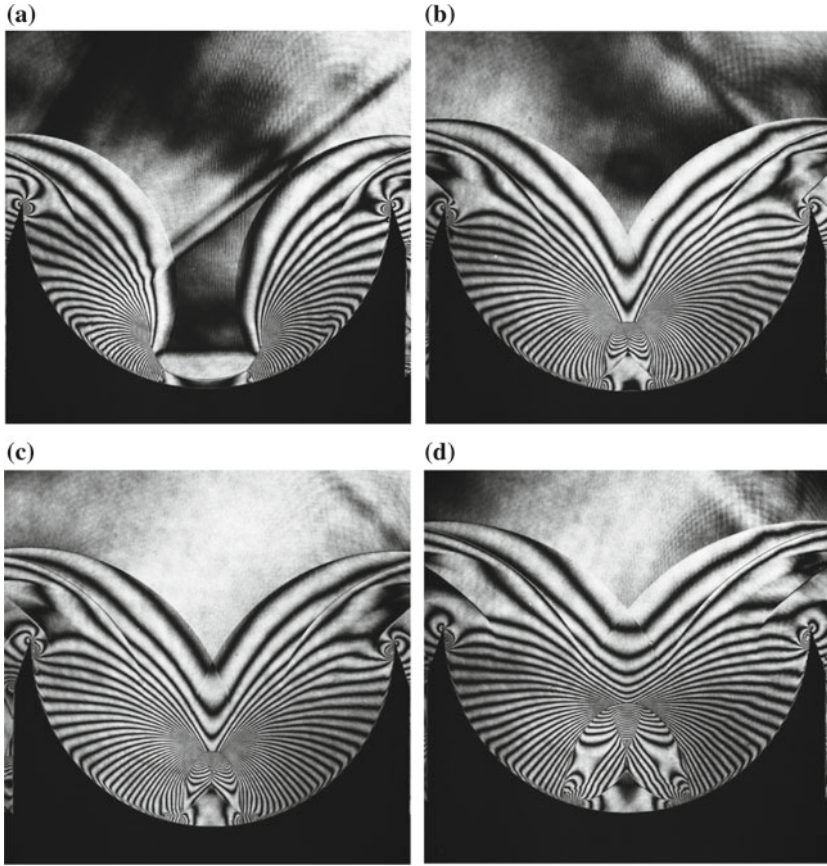


Fig. 5.3 Evolution of shock wave focusing from a 120 mm diameter circular wall in stalled in the 60 mm \times 150 mm conventional shock tube for $M_s = 1.46$ in air at 800 hPa, 289.5 K: **a** #84042628, 120 s from the trigger point, $M_s = 1.468$; **b** #84042624, 70 s, $M_s = 1.480$; **c** #84042623, 80 μ s, $M_s = 1.471$; **d** #84042620, 100 s, $M_s = 1.465$; **e** #84042619, 110 s, $M_s = 1.454$; **f** #84042618, 130 s, $M_s = 1.468$; **g** #84042615, 160 s, $M_s = 1.468$; **h** #84050209, 200 μ s, $M_s = 1.475$; **i** #8405210, 144 s, $M_s = 1.468$; **j** #84050211, $M_s = 1.481$

Figure 5.4 shows the evolution of the reflected shock wave focusing from a 120 mm circular wall installed in the 60 mm \times 150 mm diaphragm-less shock tube for $M_s = 2.02$ in air at 450 hPa, 290 K. The pattern of focusing is similar to that shown in Fig. 5.3.

Figure 5.5 show the reflection and focusing from the 120 mm diameter reflector for $M_s = 3.0$ in air at 60 hPa, 291 K. Figure 5.5a shows a transitional Mach reflection, TMR. With increasing the wall angle, the reflection pattern transits to a

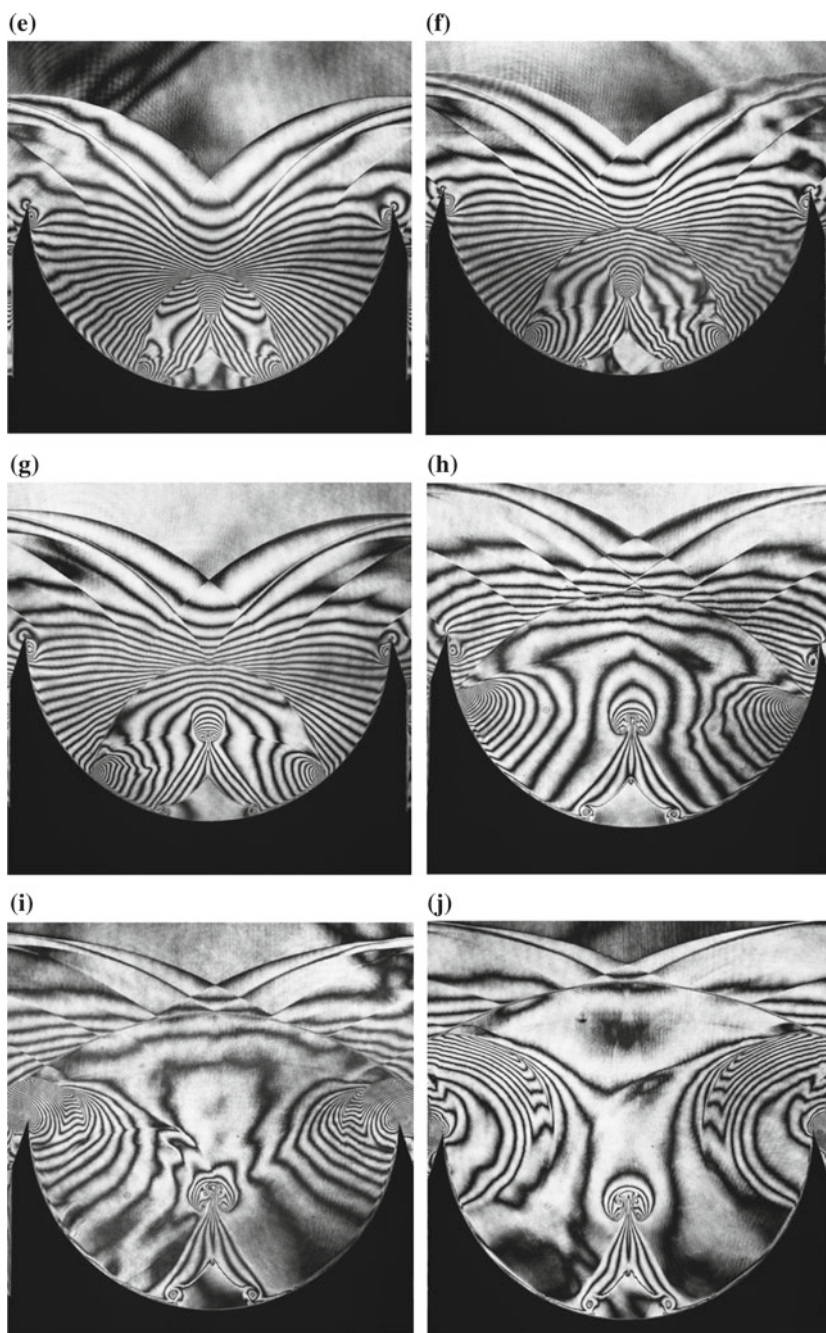


Fig. 5.3 (continued)

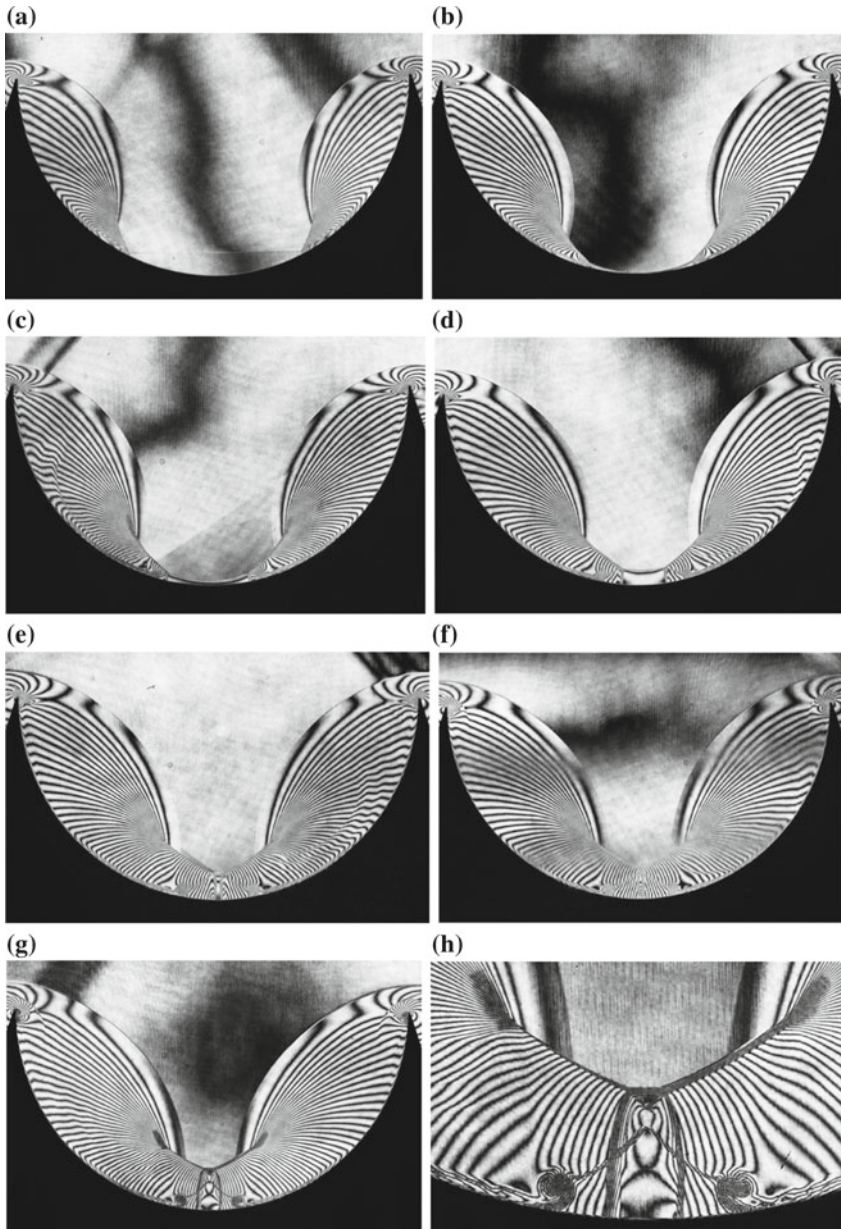


Fig. 5.4 Shock wave focusing from a 120 mm diameter circular wall for $Ms = 2.02$ in air at 450 hPa, 290 K: **a** #86030615, 265 μs , $Ms = 2.033$; **b** #86030618, 280 μs , $Ms = 2.030$; **c** #86030701, 300 μs , $Ms = 2.020$; **d** #86030617, 275 μs , $Ms = 2.030$; **e** #86030704, 315 μs , $Ms = 2.010$; **f** #86030619, 290 μs , $Ms = 2.015$; **g** #86030707, 330 μs , $Ms = 2.002$; **h** enlargement of (g); **i** #86030706, 325 μs , $Ms = 2.025$; **j** #86030708, 335 μs , $Ms = 2.030$; **k** #86030711, 350 μs , $Ms = 2.019$; **l** #86030713, 360 μs , $Ms = 2.011$; **m** #86030716, 395 μs , $Ms = 2.035$; **n** #86030718, 430 μs , $Ms = 2.026$; **o** enlargement of (n)

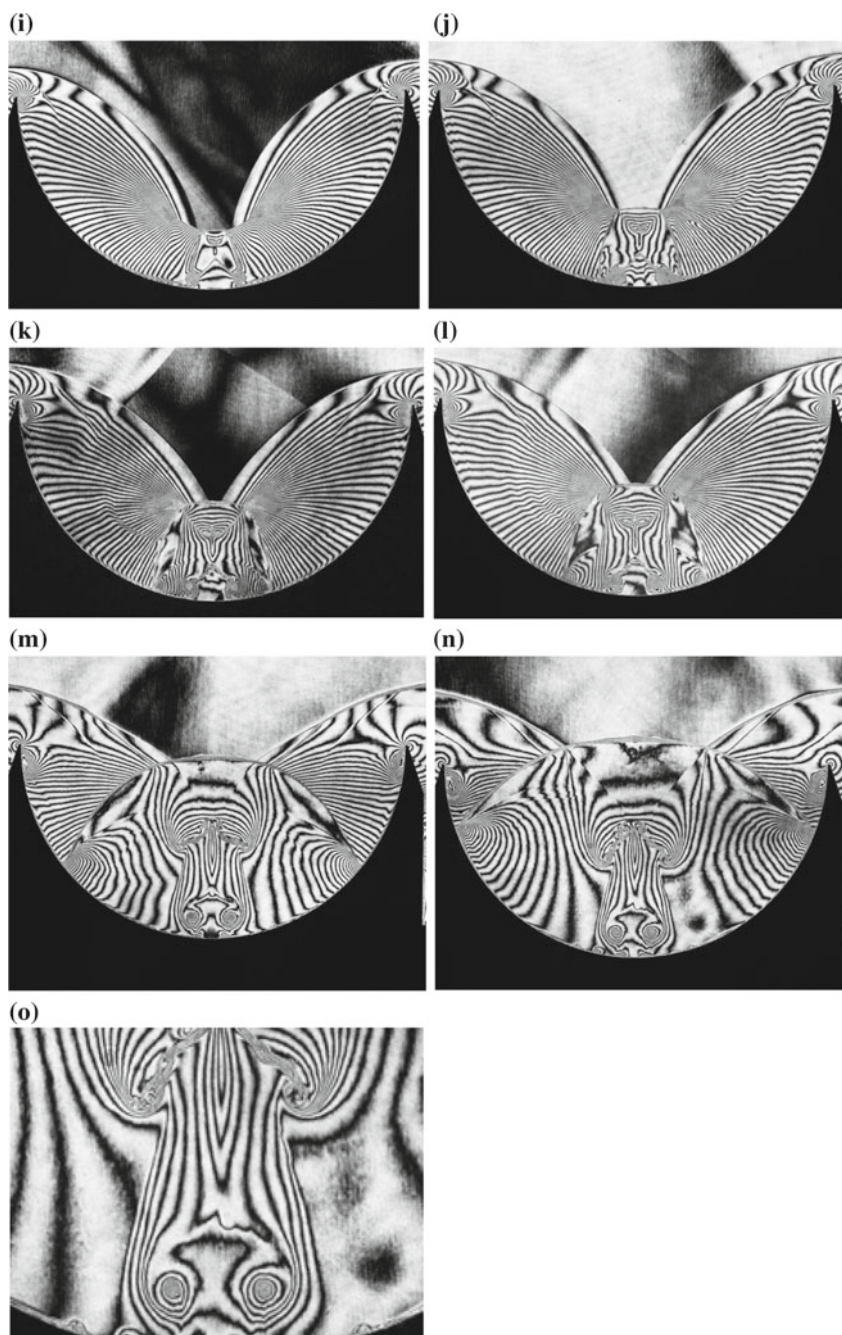


Fig. 5.4 (continued)

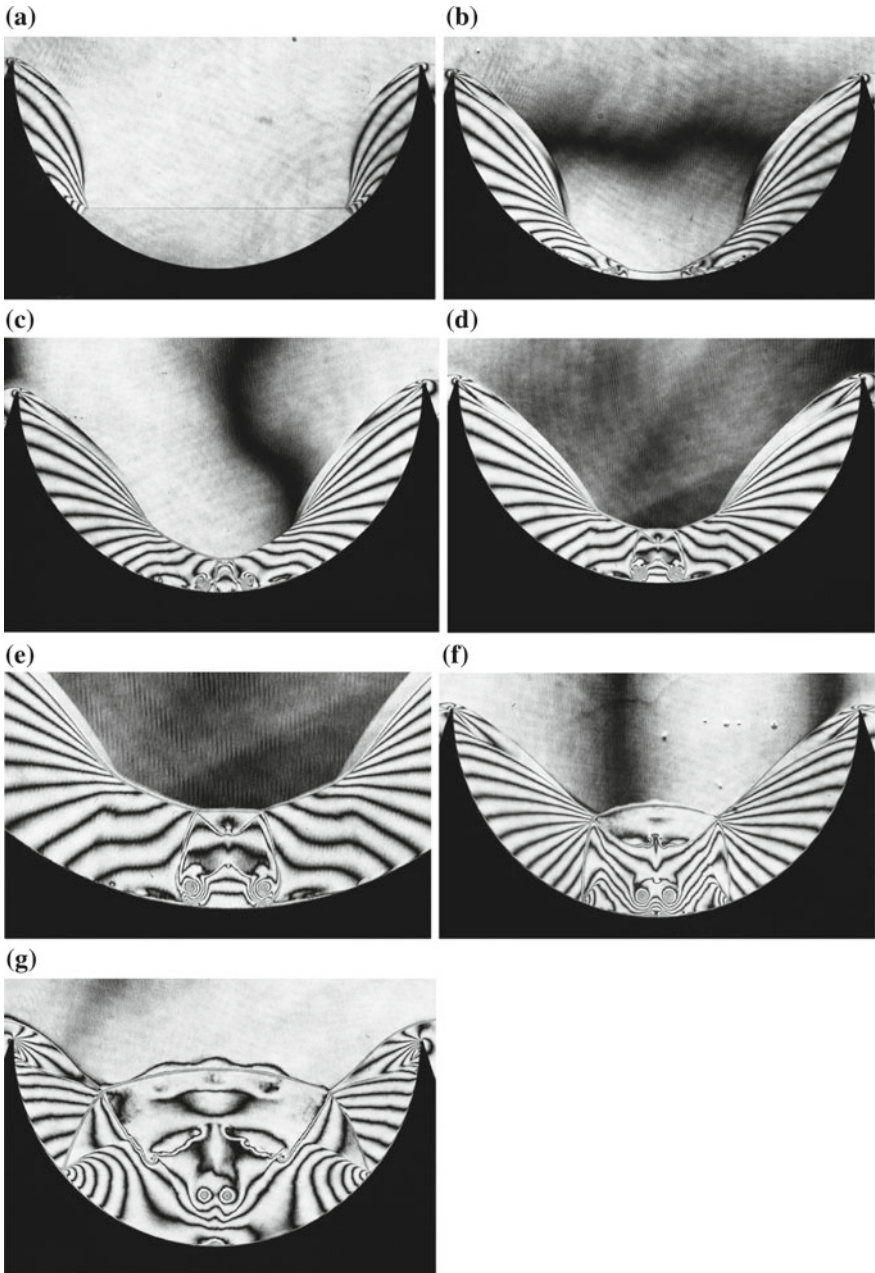


Fig. 5.5 Shock wave focusing from a 120 mm diameter circular wall for $M_s = 3.0$ in air at 60 hPa, 291 K: **a** #86031303, 100 μs from the trigger point, $M_s = 2.966$; **b** #86031305, 120 μs , $M_s = 2.954$; **c** #86031407, 105 μs , $M_s = 3.015$; **d** #86031408, 110 μs , $M_s = 3.054$; **e** enlargement of **(d)**; **f** #86031001, 50 μs , $M_s = 3.013$; **g** #86031505, 180 μs , $M_s = 3.027$

DMR and successively becomes an IvMR. Figure 5.5b shows a reflection of the resulting SPRR. The secondary Mach stems moving from the both sides move toward the center and eventually intersect with each other at the center. A symmetrical interaction of slip lines is observed in Fig. 5.5c, d as the initial pressures is reduced, the pattern observed so far formed coincidentally an exotic human face as seen in Fig. 5.5d. In Fig. 5.5g the bifurcated reflected shock wave induced by its interaction with the sidewall boundary layer, the figure that looks like a crown attached to the human face.

5.2.2 *Closed Circle*

A 30 mm × 300 mm diameter test section was connected the 30 mm × 40 mm conventional shock tube, which became a closed circular test section. Unlike previous truncated cylinders, this closed circular test section had no singular geometry. Figure 5.6 shows the evolution of shock wave propagating and reflecting inside the closed circular test section for $M_s = 1.5$ in atmospheric air at 290 K. In Fig. 5.6a, b, the incident shock waves is diffracting at the entrance corner and generating a pair of twin vortices. The transmitting shock waves continuously change their reflection patterns as discussed in the Sect. 5.1.1. The reflected patterns eventually became IvMR as seen in Fig. 5.6c. The secondary Mach stems interacted as is successively observable in Fig. 5.6d–f. Meantime, the vortices generated at the entrance corners developed with increasing time and started interacting with the reflected waves as seen in Fig. 5.6g–l.

The early stage of focusing is similar to that seen from concave walls but at later stage the interactions with the vortices generated at the entrance corner appeared (Sun 2005).

5.2.3 *Effects of Entrance Angles on Focusing*

Focusing of shock waves from a concave wall is affected by the initial angle of the curved walls. Therefore, Fig. 5.7 shows a reflector having initial angles of $\theta = 75^\circ$, 45° , 30° , and 15° installed in the 40 mm × 80 mm conventional shock tube.

5.2.3.1 *Wall Angle 75°*

Figure 5.8 shows the evolution of a weak shock wave reflected from a circular reflector having a wall angle 75° and a radius of 154.6 mm for $M_s = 1.13$ in atmospheric air at 295.0 K. The initial reflection pattern is SPRR. Then the two SPRR propagating along the upper and the lower walls intact with each other and the final reflection pattern becomes a vNMR as seen in Fig. 5.8e–f.

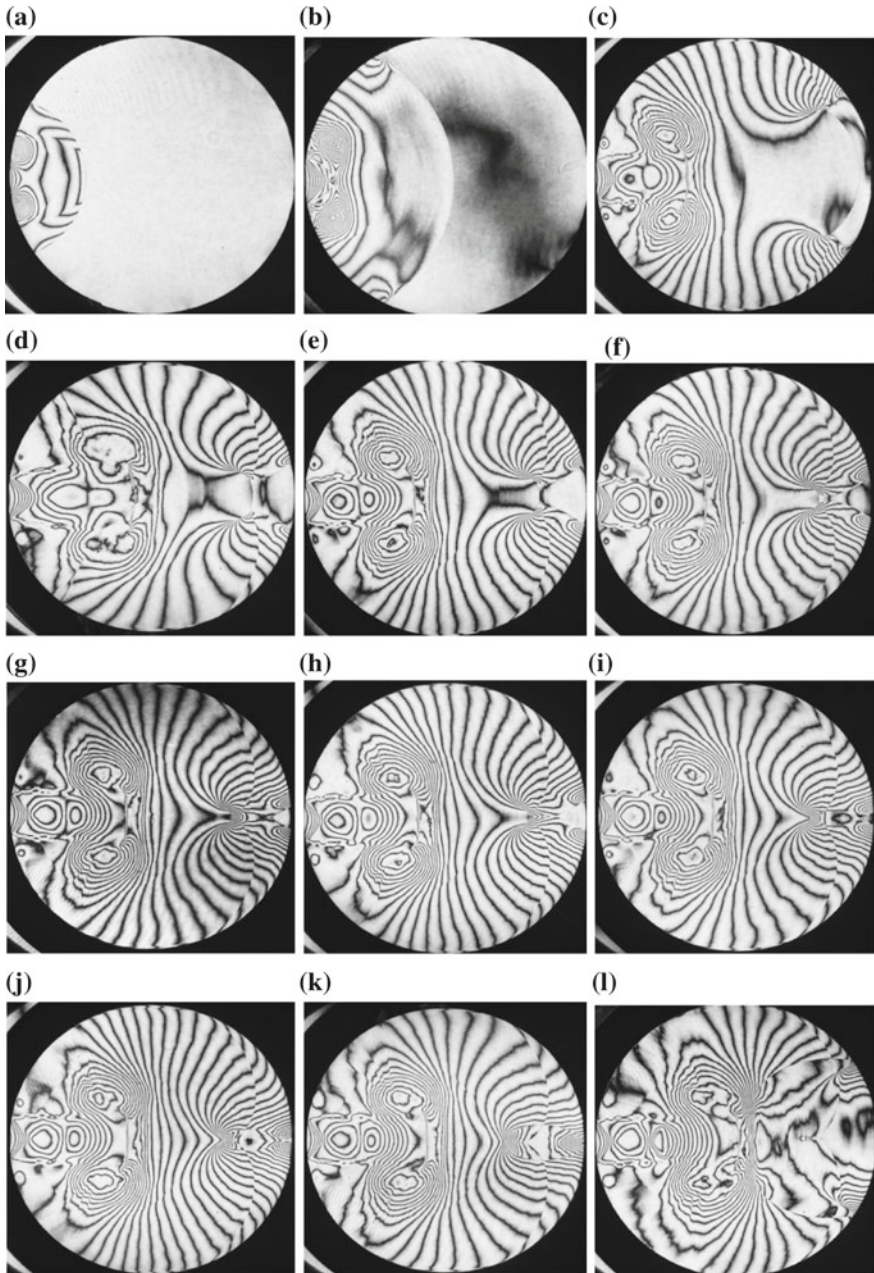
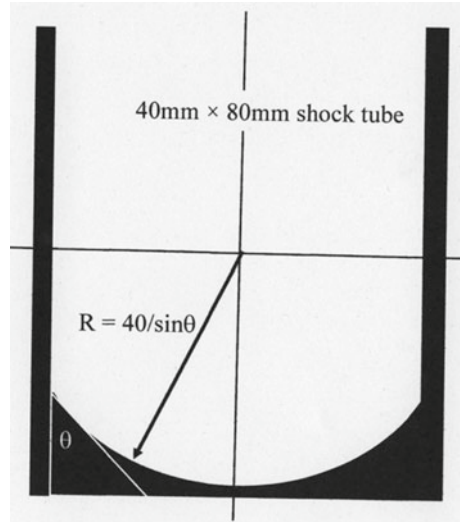


Fig. 5.6 Shock wave focusing from a 300 mm diameter circular wall for $Ms = 1.5$ in atmospheric air at 290 K (Sun et al. 2005): **a** #95100401; **b** #95100507; **c** #95100403; **d** #95100408; **e** #95100405; **f** #95100504; **g** #95100404; **h** #95100509; **i** #95100510; **j** #95100505; **k** #95100406; **l** #95100506

Fig. 5.7 A reflector of radius $R = 40/\sin\theta$ mm installed in a $40\text{ mm} \times 80\text{ mm}$ shock tube, where θ is the wall angle



5.2.3.2 Wall Angle 45°

Figure 5.9 shows the evolution of the reflected shock wave focusing from concave wall angle of 45° for $M_s = 1.13$ in atmospheric air at 295.0 K . The IvMR transits to SuRR which accompany a secondary TP. Then, the secondary triple points contribute to the final reflected shock wave pattern. The vortices remain at the end wall, see in Fig. 5.9d–f. The effect of the initial wall angle 45° on the reflection pattern is similar to that observed in the case where the initial wall angle was 75° .

5.2.3.3 Wall Angle 30°

Figure 5.10 shows the evolution of the reflected shock wave focusing from the concave wall set angle at 30° for $M_s = 1.13$ in atmospheric air at 295.0 K . The reflection pattern is almost identical to the one observed in the case where the wall angle was 45° . The reflection pattern transits from an IvMR to a SPRR.

5.2.3.4 Wall Angle 15°

The evolution of the reflected shock wave focusing from a concave wall angle set at 15° for $M_s = 1.07$ in atmospheric air at 295.0 K . The inverse Mach reflections, IvMR, merge at the center as seen in Fig. 5.11a, b. The shock waves reflected from the corner are now so weakened that the waves are not observable as seen in Fig. 5.11e–g.

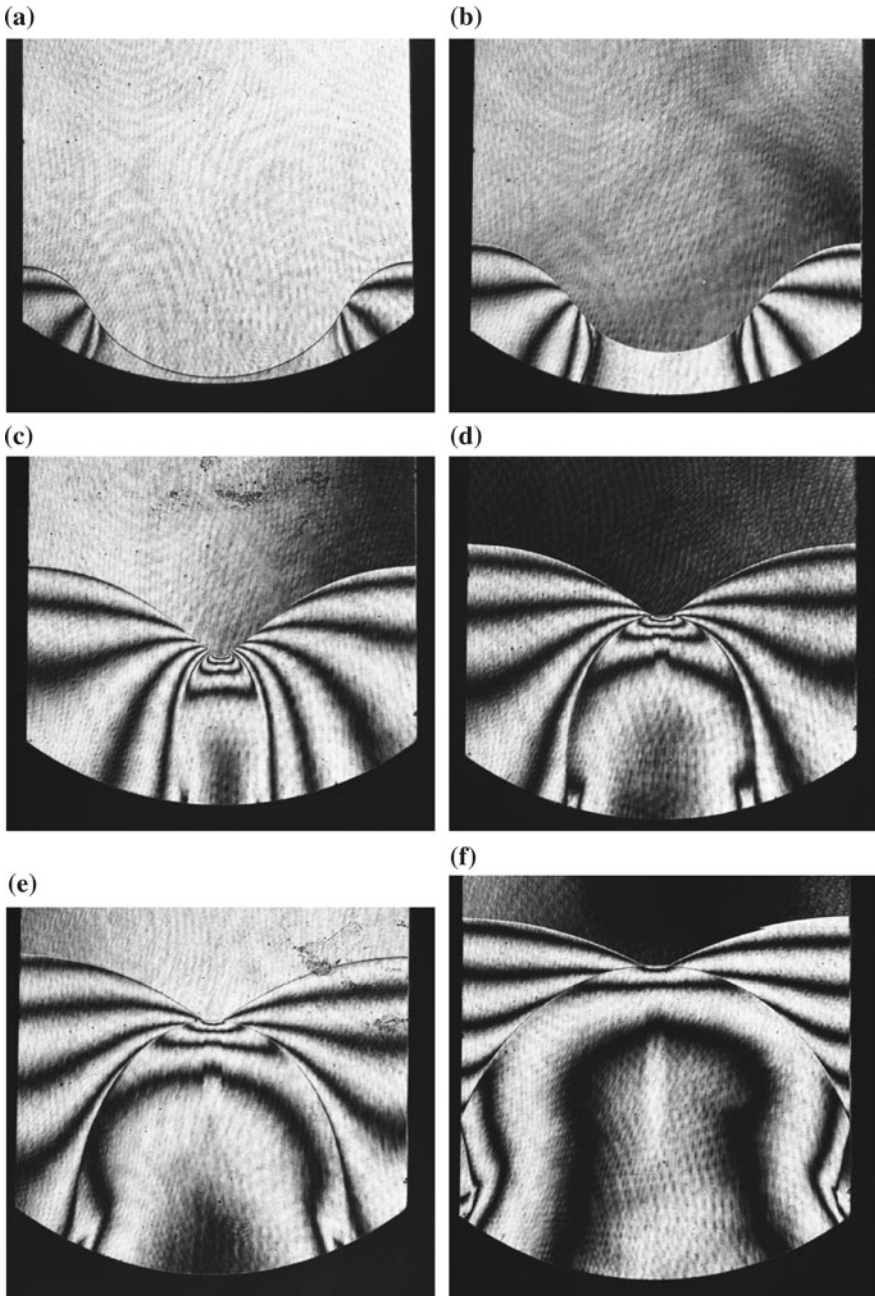


Fig. 5.8 The evolution of the reflected shock wave focusing from concave wall angle of 75° for $M_s = 1.13$ in atmospheric air at 295.0 K: **a** #81061904, 50 μs from trigger point, $M_s = 1.131$; **b** #81061906, $M_s = 1.136$; **c** #81061909, 100 μs , $M_s = 1.136$; **d** #81061910, 110 μs , $M_s = 1.148$; **e** #81061911, 130 μs , $M_s = 1.148$; **f** #81061913, 200 μs , $M_s = 1.137$

5.2.3.5 Entrance Angle 40°

Circular reflectors with various wall angles of 40°, 50°, 60°, and 70° were placed in the 60 mm × 150 mm conventional shock tube for visualizing the evolution of shock wave focusing for $M_s = 1.30$ (Fig. 5.12).

Figure 5.13a shows the wall angle of $\theta = 40^\circ$ and $M_s = 1.30$. The radius R of the circular wall is given by $R = 30/\sin\theta$ in mm. The initial reflection pattern was a SMR which eventually transited to an IvMR. Figure 5.13a shows the resulting regular reflection SuRR. A pair of secondary triple points and curved Mach stems merged between Fig. 5.13b, c. Figure 5.13d–f shows the situation at later stages.

5.2.3.6 Entrance Angle 50°

Figure 5.14 shows the evolution of the shock wave reflection from the circular wall when it is set at a wall angle of 50°. The reflection pattern is SuRR. In Fig. 5.14c, d, the triple points merged at the center and reflected. Meantime, the high-pressure area coalesced into a shock wave. This is a focusing sequence from a shallow reflector. In Fig. 5.14c, d, the flattened part of the reflected shock wave is gradually enlarged and the resulting reflection pattern is SMR.

5.2.3.7 Entrance Angle 60°

Figure 5.15 shows the reflection pattern of SuRR. The entire sequences of focusing are similar to that shown in Fig. 5.14.

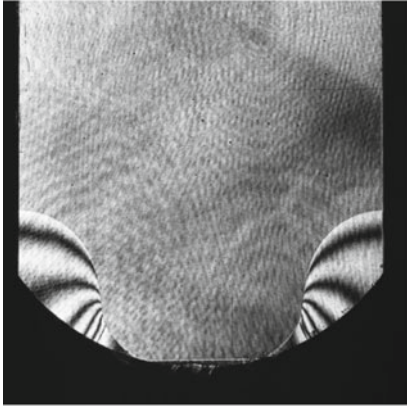
5.2.3.8 Entrance Angle 70°

The reflection pattern is SuRR. The sequence of focusing is very similar to that observed in Fig. 5.15. The general trend is that the reflection pattern approaches to the reflection from a slightly perturbed plane wall (Fig. 5.16).

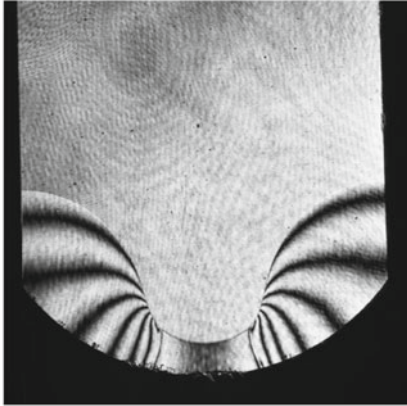
5.3 Shock Wave Reflection from Convex and Concave Walls

A combination of convex and concave reflectors as illustrated in Fig. 5.17 is installed in the 60 mm × 150 mm conventional shock tube. Sequence of focusing was observed for the varying radius R . For the given depth H of the reflectors, R is determined by $2R = (L^2 + H^2)/(4H)$, where L is the width of test section $L = 150$ mm.

(a)



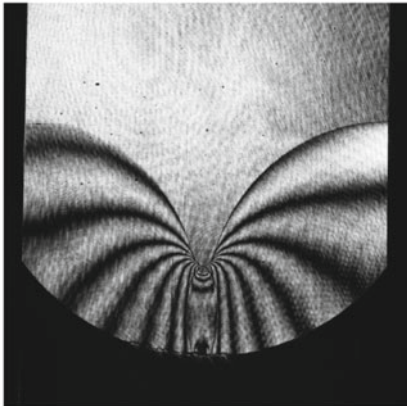
(b)



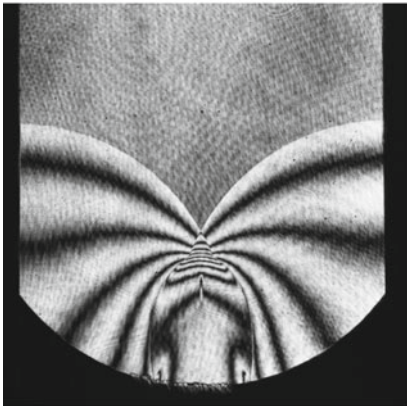
(c)



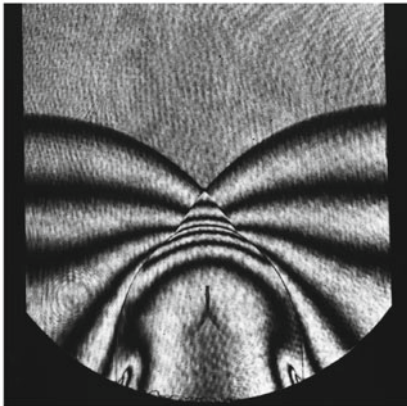
(d)



(e)



(f)



◀**Fig. 5.9** Evolution of reflected shock wave focusing from concave wall angle of 45° for $M_s = 1.13$ in atmospheric air at 295.0 K: **a** #81061924, 50 μs from trigger point, $M_s = 1.135$; **b** #81061923 70 μs , $M_s = 1.140$; **c** #81061922, $M_s = 1.147$; **d** #81061921, 110 μs , $M_s = 1.139$; **e** #81061920 130 μs , $M_s = 1.133$; **f** #81061919, 150 μs , $M_s = 1.137$; **g** #81061918, $M_s = 1.109$; **h** #81061917, $M_s = 1.137$

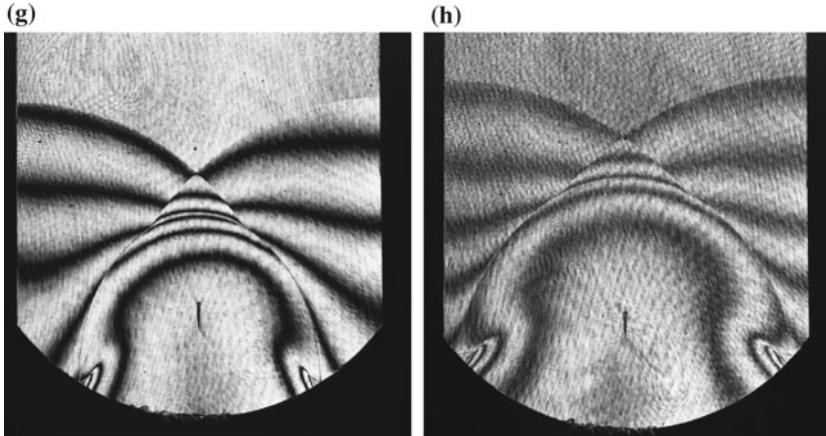


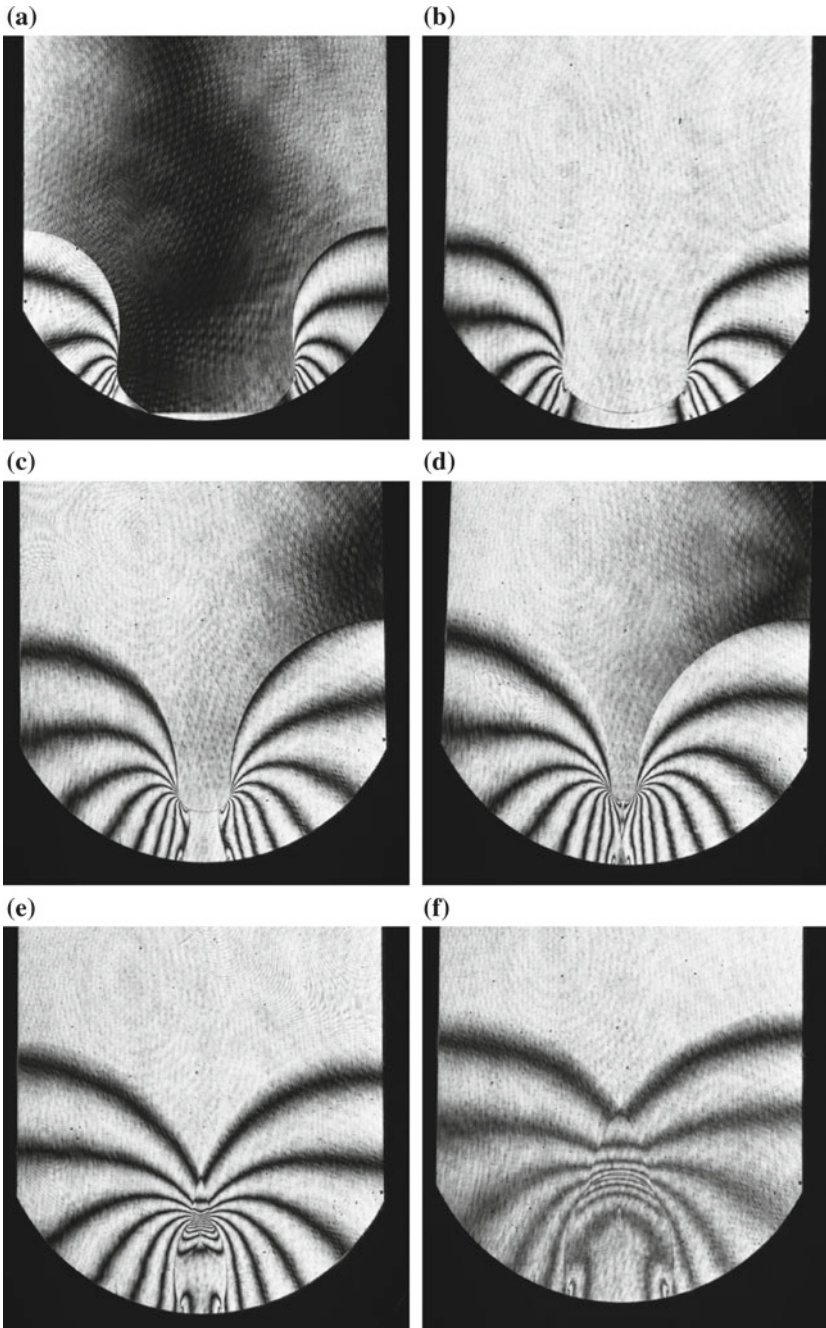
Fig. 5.9 (continued)

5.3.1 75 mm Depth

For a given depth of 75 mm, the radius R is 37.5 mm. Figure 5.18 shows the evolution of the reflection and focusing for $M_s = 1.40$, in atmospheric air at 297 K. The circular entry shape decisively affected the process of the propagation and focusing of the transmitting shock wave. Figure 5.18a–h showed the sequence of focusing. The waves reflected from the upper and lower walls affected the sequence of focusing. The focusing of slip lines observed in Fig. 5.18g, h is very similar to the pattern as seen in Fig. 5.3. Mean time during the shock vortex interaction, wave patterns with exotic shapes appeared. The comparison between the present experimental findings and an appropriate numerical simulation would be a challenging task for nfor code validation.

5.3.2 Depth 57 mm

Figure 5.19 shows a reflection from a convex and concave reflector of $H = 57$ mm and $R = 56.5$ mm for $M_s = 1.44$. The reflection pattern is, at first, a RR and along a concave section, transits to a SMR in Fig. 5.19a and eventually becomes a SuRR in Fig. 5.19b. Then repeating the wave interactions, the focusing is terminated in Fig. 5.19d.



◀**Fig. 5.10** The evolution of the reflected shock wave focusing from a concave wall angle of 30° for $M_s = 1.13$ in atmospheric air at 295.0 K: **a** #81062002, 50 μs after the trigger point, $M_s = 1.139$; **b** #81062004, 70 μs , $M_s = 1.136$; **c** #81062005, 90 μs , $M_s = 1.149$; **d** #81062009, 97 μs , $M_s = 1.136$; **e** #81062006, 110 μs , $M_s = 1.150$; **f** #81062007, 130 μs , $M_s = 1.138$; **g** #81062009, 140 μs , $M_s = 1.136$; **h** #81062009, 150 μs , $M_s = 1.136$

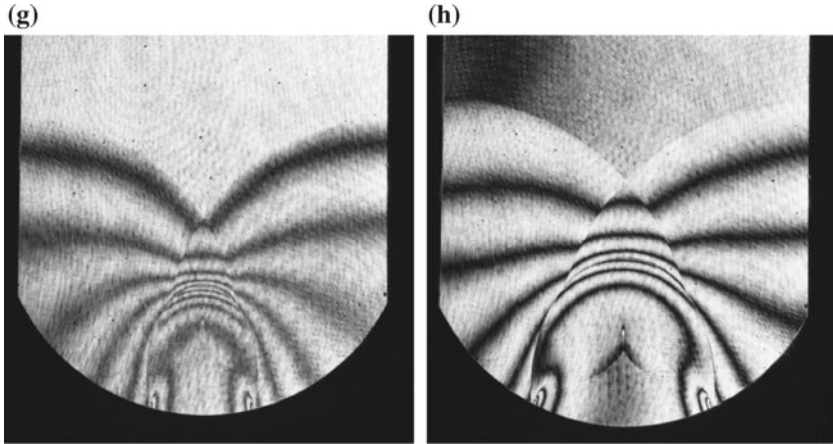


Fig. 5.10 (continued)

5.3.3 Depth 42 mm

Figure 5.20 shows the evolution of the shock wave reflection from a combined reflector having $R = 72.2$ mm and $H = 42$ mm for $M_s = 1.43$ in atmospheric air at 297.6 K. In Fig. 5.20a, the reflection pattern is SuRR accompanying a secondary shock wave. The sequence of shock wave reflections from a shallow reflector is similar to that observed in the case of shallow entrance angles. The reflection pattern shown in Fig. 5.20f is similar to that shown in Fig. 5.19f.

5.3.4 Depth 31 mm

Figure 5.21 shows the shock wave reflection from a shallow reflector of $R = 94.6$ mm and $H = 31$ mm for $M_s = 1.42$ in atmospheric air at 293.0 K. The reflection and focusing from the shallow reflector shown in Fig. 5.21 is similar to the focusing of IvMR and similar to the reflection from the shallow reflectors seen in Figs. 5.8 and 5.25.

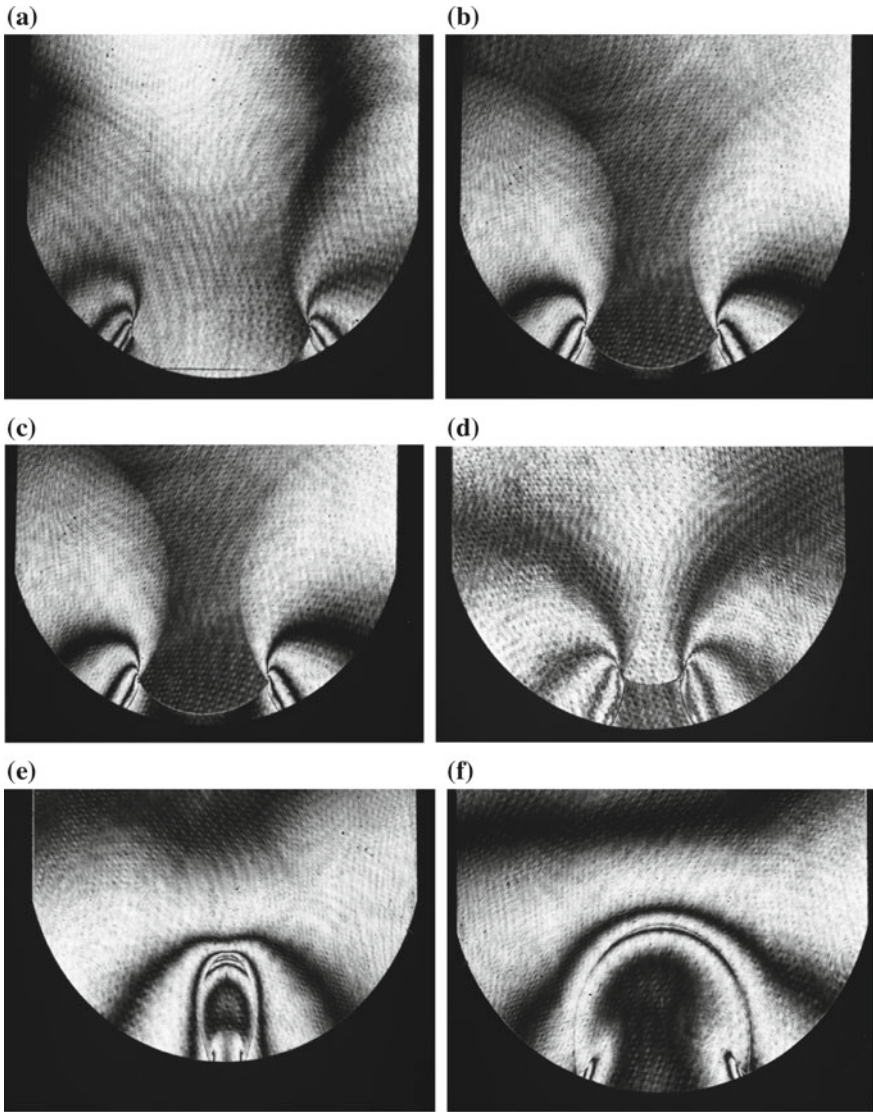


Fig. 5.11 The evolution of the reflected shock wave focusing from concave wall angle of 15° for $M_s = 1.07$ in atmospheric air at 295.0 K: **a** #81062307, 140 μs , from trigger point $M_s = 1.062$; **b** #81062306, 80 μs , $M_s = 1.081$; **c** #81062305 100 μs , $M_s = 1.069$; **d** #81062304, 120 μs , $M_s = 1.060$; **e** #81062303, 150 μs , $M_s = 1.060$; **f** #81062309, 180 μs , $M_s = 1.063$; **g** #81062301, 200 μs , $M_s = 1.048$

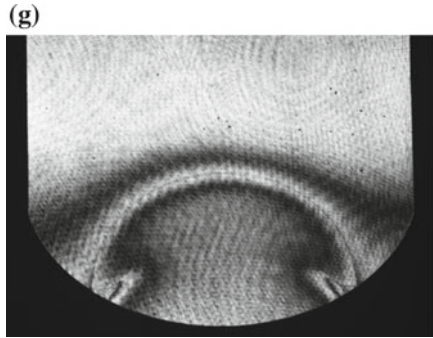
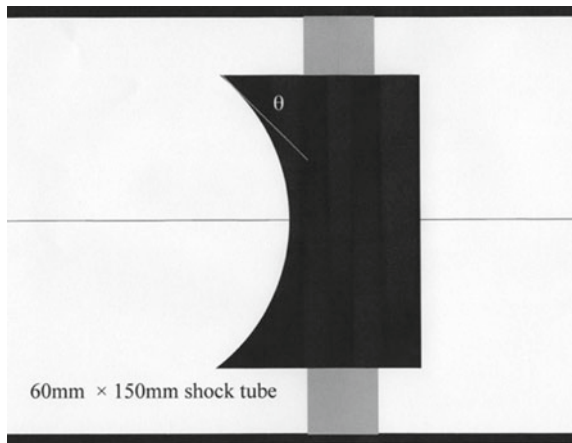


Fig. 5.11 (continued)

Fig. 5.12 Circular reflector of wall angle θ installed in a 60 mm \times 150 mm conventional shock tube



5.4 Focusing from a Logarithmic Spiral Shaped Area Convergence

Shock waves are focused while passing along a duct having area convergence or reflected from concave walls. However, such a shock wave focusing is always associated with wave interactions. If a planar shock wave could be focused on a localized area while propagating along a specially shock tube having a special shape, it would have been wonderful. Milton et al. (1975) proposed a logarithmic spiral shaped passage in which a planar shock wave can be focused to a spot and thereby generating high pressures and temperatures. The theory was based on Whitham's ray shock theory (Whitham 1959).

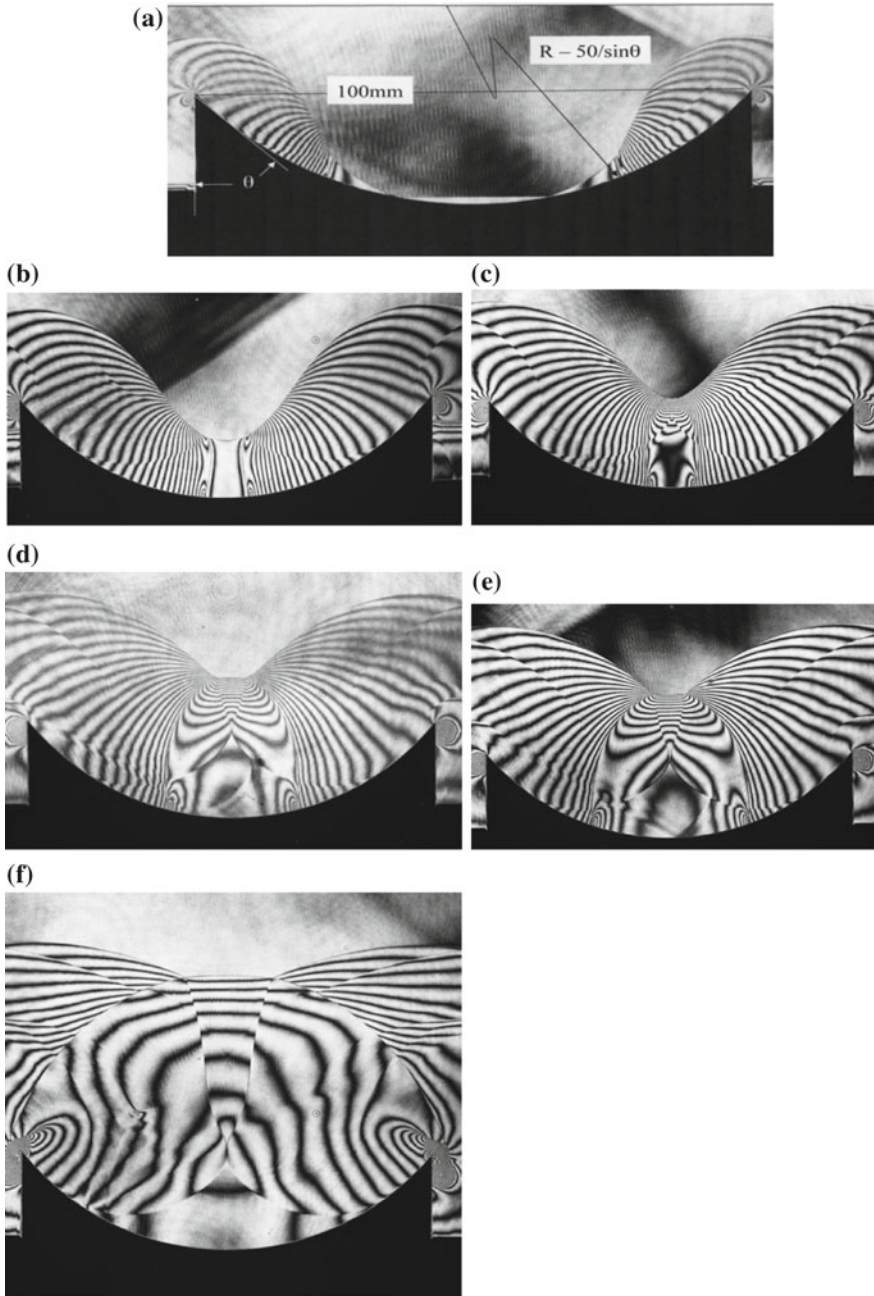


Fig. 5.13 Effects of the wall angle of 40° for $M_s = 1.30$, in atmospheric air at 286.4 K: **a** #84042515, 120 μs from trigger point, $M_s = 1.304$; **b** #84042521, 170 μs , $M_s = 1.306$; **c** #84042513, 240 μs , $M_s = 1.304$; **d** #84042519, 320 μs , $M_s = 1.315$; **e** #84042513, 240 μs , $M_s = 1.304$; **f** #84042519, 320 μs , $M_s = 1.315$

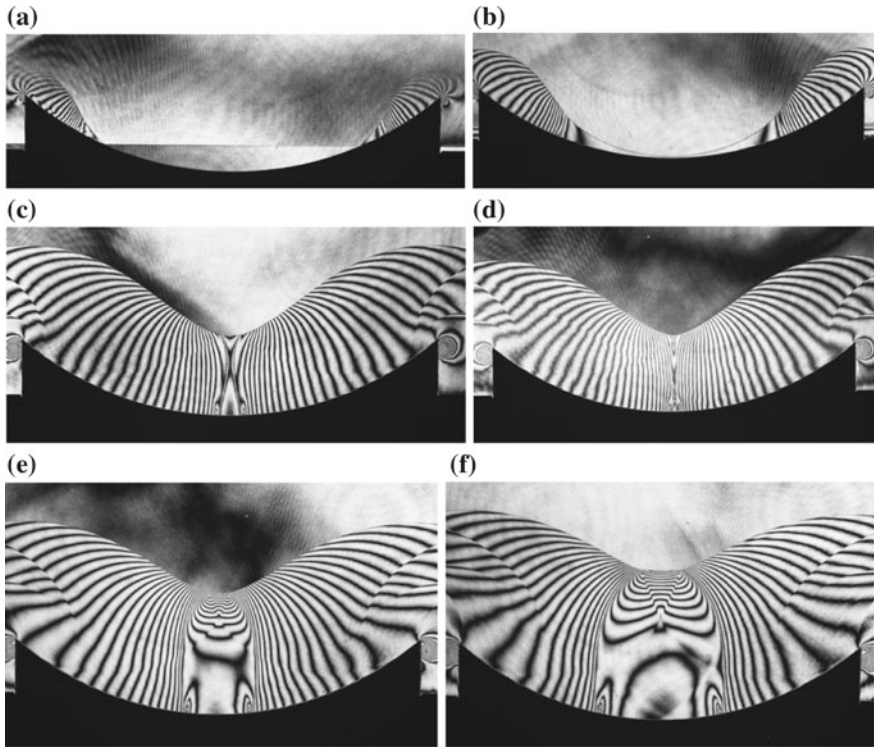


Fig. 5.14 Effects of the wall angle of 50° for $Ms = 1.30$ in atmospheric air at 286.4 K; **a** #84042509, 110 μs from trigger point, $Ms = 1.306$; **b** #84042507, 130 μs , $Ms = 1.301$; **c** #84042504, 160 μs , $Ms = 1.306$; **d** #84042501, 200 μs , $Ms = 1.306$; **e** #84042506, 220 μs , $Ms = 1.308$; **f** #84042508, 240 μs , $Ms = 1.311$

Such a configuration is a logarithmic spiral defined in the (r, θ) -plane as:

$$r = R \exp\{(\chi - \theta) / \tan \chi\}$$

where R and χ are given for specifying the Ms and the value of γ (Milton et al. 1975) and indicate the radius of the starting point of log-spiral shape from the origin and the initial angle between the sidewall and the line from the origin to the starting point as shown in Fig. 5.22, respectively.

The logarithmic spiral shape is determined for specified values of Ms and the specific heats ratio of the test gas of γ and hence a given R and χ .

For specified values of Ms and χ , log-spiral shaped models having 129 mm long and 30 mm wide were manufactured and installed in the 60 mm \times 150 mm conventional shock tube. The models had 30 mm long straight entry and 99 mm long log-spiral section. The Mach number, Ms , ranged from $Ms = 1.4$ to 2.7 in air (Milton 1989). Figure 5.23 shows the evolution of a shock wave focusing in a

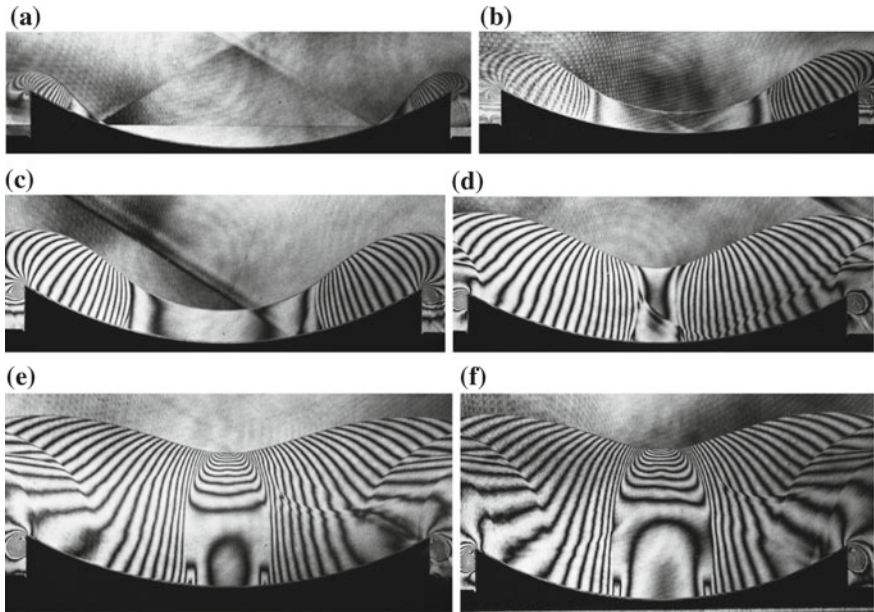


Fig. 5.15 Effect of wall angle of 60° for $Ms = 1.30$ in atmospheric air at 286.4 K: **a** #84042406, $400 \mu s$ from the trigger point, $Ms = 1.303$; **b** #84042405, $400 \mu s$, $Ms = 1.311$; **c** #84042407, $450 \mu s$, $Ms = 1.303$; **d** #84042409, $490 \mu s$, $Ms = 1.308$; **e** #84042411, $530 \mu s$, $Ms = 1.311$; **f** #84042412, $550 \mu s$, $Ms = 1.308$

logarithmic spiral shaped passage manufactured for specially for $Ms = 1.40$ and their enlargements for $Ms = 1.40$ in atmospheric air at 294.8 K.

Figure 5.23a shows the early stage of focusing. The IS's foot is always perpendicular to the log-spiral wall so that at the earlier stage, the shock wave in the vicinity of the foot of the IS on the log-spiral is curved smoothly. This trend was observed previously when discussing the IS propagation along a concave wall, for example see in Fig. 5.3. The shock wave smoothly converges keeping the triple point position initially at its glancing incidence angle. The foot of the is always perpendicular to the log-spiral wall and the central part of the transmitted shock wave is perpendicular to the central plane of the shock tube.

In Fig. 5.23a, even though the fringe number increased, the transmitting shock wave still curved continuously connecting smoothly with its foot. This trend became enhanced as seen in Fig. 5.23b. When the fringe concentration was maximal along the smoothly curved transmitted shock wave, a distinct triple points appear as seen in Fig. 5.23c. The reflection pattern quickly turned into an IvMR and merged at the center. The resulting focusing was a merger of vortices shown in Fig. 5.23d. Anyway, the merit of the log-spiral shape was effective in focusing of a planar shock wave to a point while minimizing the generation of undesirable wave interactions. At a later stage of focusing, the reflection pattern was similar to the one observed in the case of shock wave focusing from a concave reflector, the

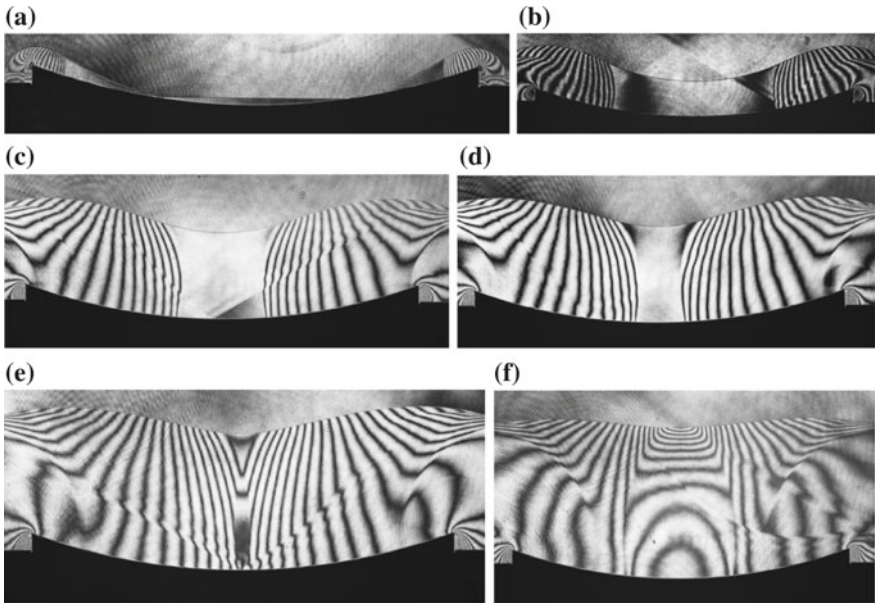
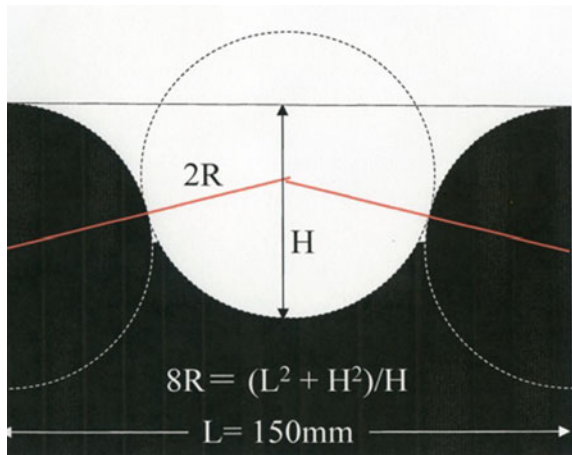


Fig. 5.16 Effects of wall angle of 70° for $Ms = 1.30$, in atmospheric air at 286.4 K: **a** #84042005, 120 μs , $Ms = 1.314$; **b** #84042009, 160 μs , $Ms = 1.320$; **c** #84042013, 200 μs , $Ms = 1.320$; **d** #84042014, 220 μs , $Ms = 1.311$; **e** #84042015, 240 μs , $Ms = 1.311$; **f** #84042017, 280 μs , $Ms = 1.313$

Fig. 5.17 A concave and convex wall



accumulation of vortices played an important role during a later stage of focusing. In Fig. 5.23d, the dense accumulation of fringes turned into vortices. After the vortex interaction, the flow fields become more or less similar to the case of shock wave reflections from circular reflectors. When the vortices converged at the end of the log-spiral reflector as seen in Fig. 5.23d and in its enlargement in Fig. 5.23h, the

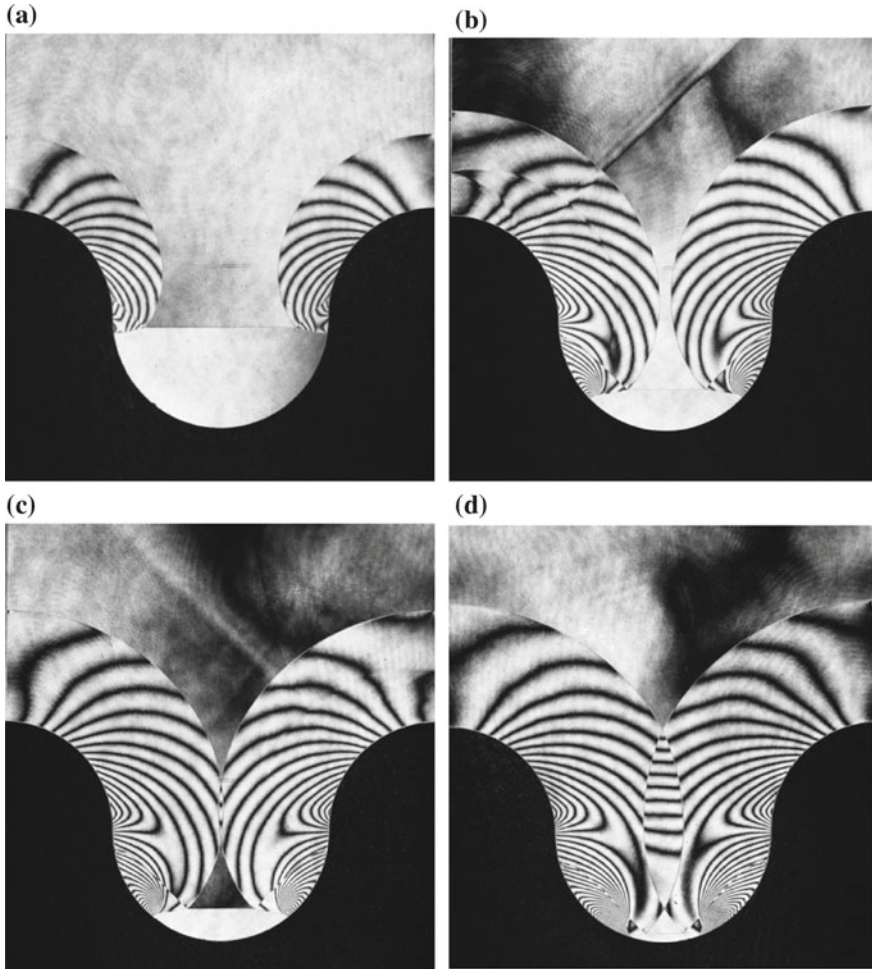


Fig. 5.18 Effect of convex and concave walls on focusing, 75 mm depth for $M_s = 1.40$, in atmospheric air at 297 K: **a** #86091816, $M_s = 1.427$; **b** #86091810, $M_s = 1.435$; **c** #86091803, $M_s = 1.411$; **d** #86091806, $M_s = 1.416$; **e** #86091803, $M_s = 1.411$; **f** #86091805, 310 μs , $M_s = 1.414$; **g** #86091811, $M_s = 1.433$; **h** #86091801, $M_s = 1.407$

temperature would be enhanced as to emit luminosity from the spot where the vortex focused. In holographic interferometry, the luminous emissions are not observable because the sensitivity of holographic films could not detect the luminosity but Milton et al. (1975) used direct shadowgraph and observed the luminosity.

Figure 5.24 shows the evolution of a shock wave focusing from a log-spiral passage for $M_s = 1.480$ in air at 900 hPa, 292.5 K. Each image is compared with its enlarged one. This log-spiral shape gradually curved the IS and eventually focused it at the tip of the log-spiral.

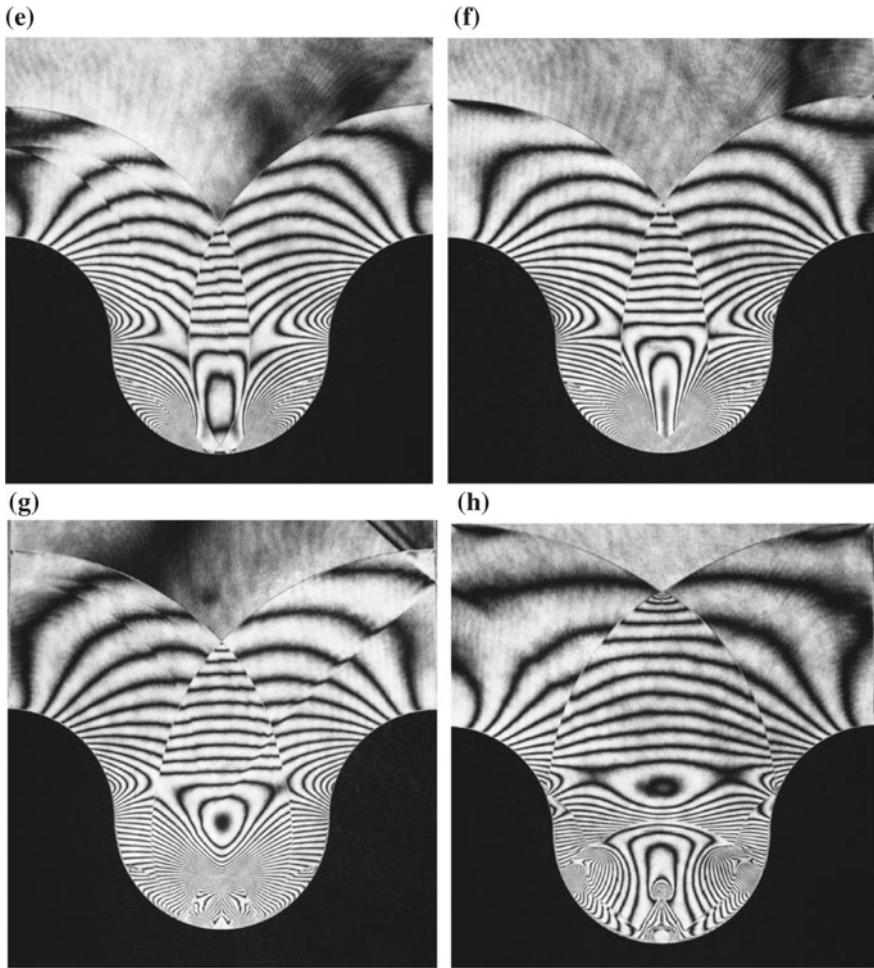


Fig. 5.18 (continued)

Figure 5.25 shows the evolution of shock wave focusing from a log-spiral passage for $Ms = 2.70$ in air at 110 hPa, 287.0 K. Figure 5.25a, c, e, f offer comparisons between recorded observations taken at a different test time with appropriate numerical simulations (Inoue et al. 1995). Figure 5.25g shows a magnified view of Fig. 5.25f. Figure 5.25d, e shows the fringe accumulation, and convergence of the vortices at its the tip of the log-spiral passage. The convergence resulted in temperature enhancement. Milton reported (Milton et al. 1975) spontaneous luminous emission due to the generation of high temperature at the tip.

As seen in Fig. 5.25, the numerical simulation agreed well with the experimental findings. Using very fine adoptive meshes, the present numerical simulation succeeded in reproducing the shock wave focusing along the log-spiral passage.

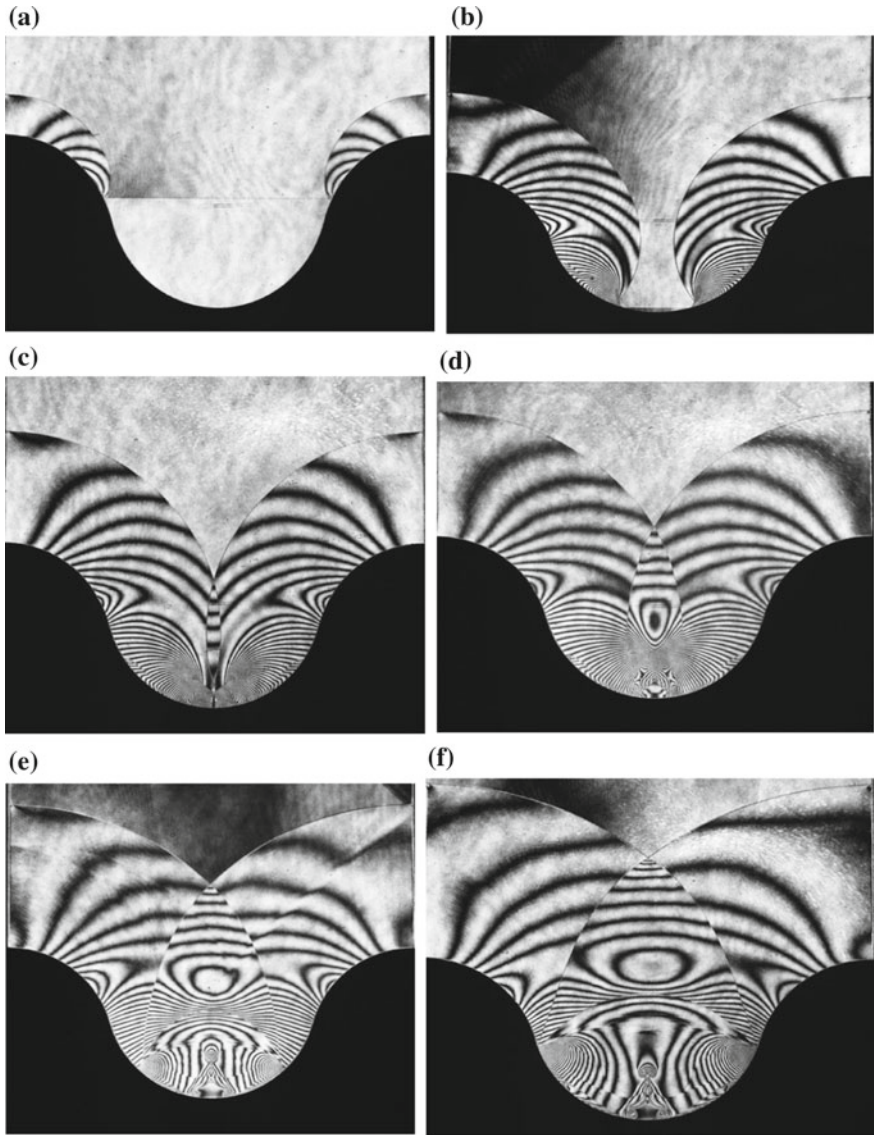


Fig. 5.19 Evolution of shock wave reflection from a convex and concave wall of 57 mm depth for $M_s = 1.43$ in atmospheric air at 293.0 K: **a** #86093006, 340 μs from trigger point, $M_s = 1.439$; **b** #86093002, $M_s = 1.432$; **c** #86092908, 385 μs , $M_s = 1.432$; **d** #86093001, 395 μs , $M_s = 1.415$; **e** #86093008, 415 μs , $M_s = 1.438$; **f** #86092905, 420 μs , $M_s = 1.439$

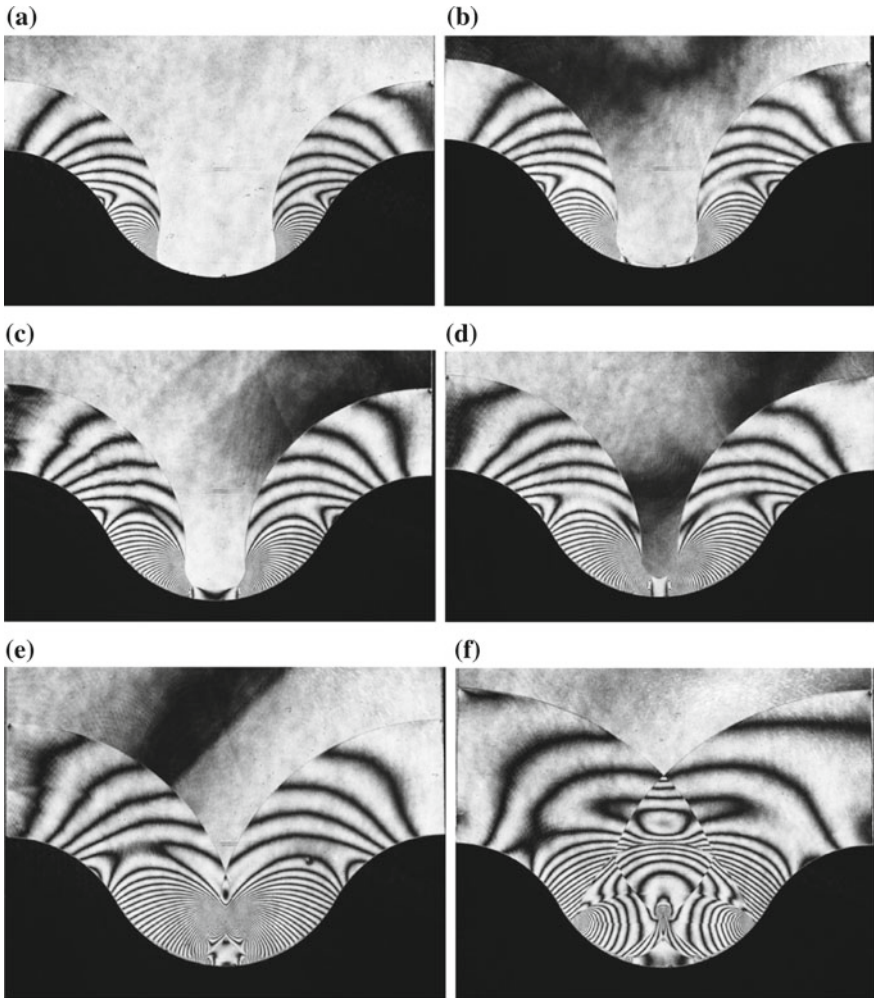


Fig. 5.20 The evolution of shock wave reflection from a convex and concave wall reflector of $R = 42$ mm for $M_s = 1.43$ in atmospheric air at 297.6 K: **a** #86100105, $M_s = 1.425$; **b** #86100107, $M_s = 1.428$; **c** #86100108, $M_s = 1.430$; **d** #86100109, $M_s = 1.431$; **e** #86100111, $M_s = 1.429$; **f** #86100116, $M_s = 1.430$

5.5 Shock Wave Focusing from Area Contraction

Shock waves are strengthened while propagating along ducts having area contraction. In a broad sense, this is a kind of shock wave focusing. When shock waves propagate along a duct having a V-shaped area contraction, the pressure enhancement varies depending on the angle of the area contraction. Figure 5.26 illustrates a V-shaped area contraction installed in the $60 \text{ mm} \times 150 \text{ mm}$

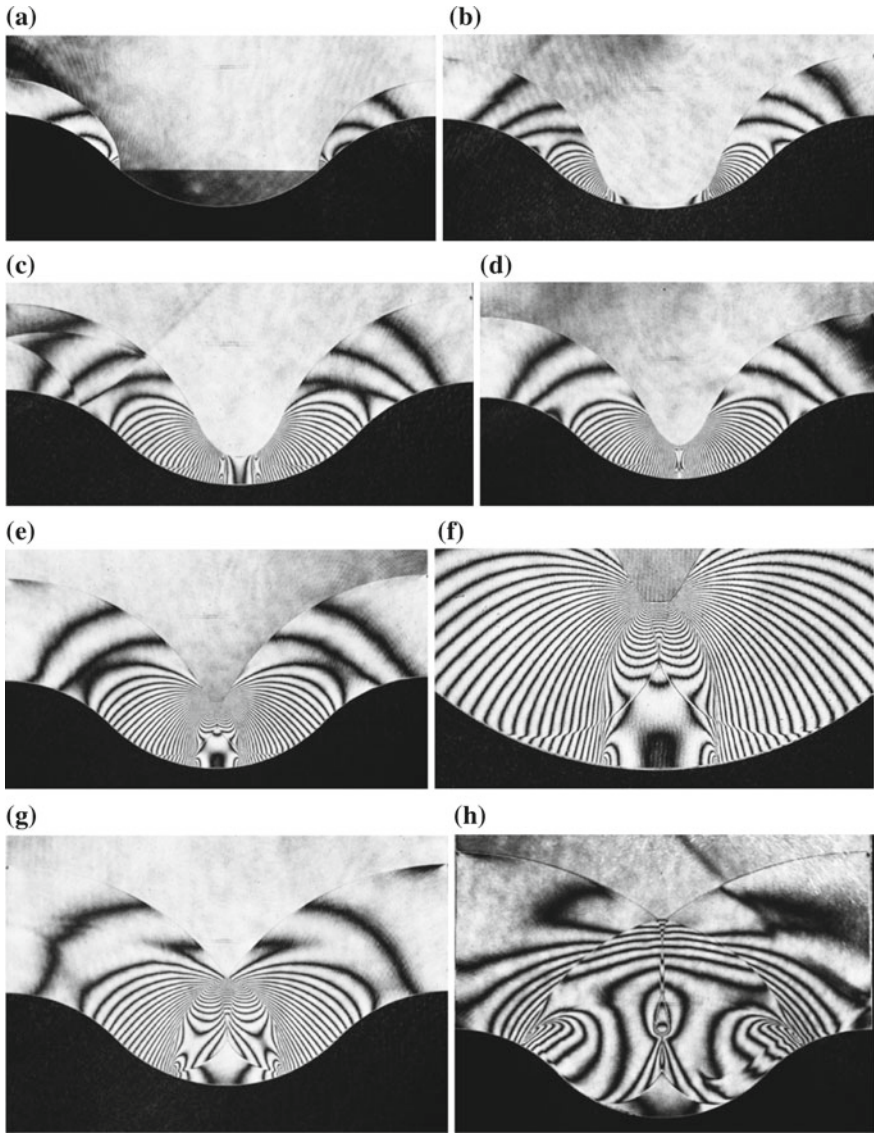
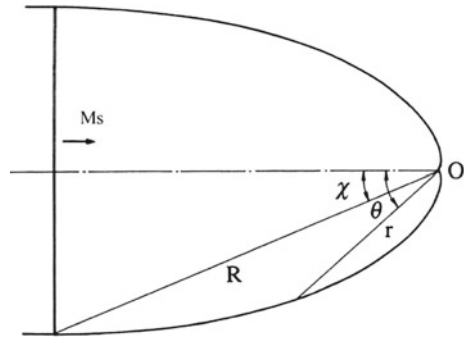


Fig. 5.21 The evolution of the shock wave reflection from a reflector of $R = 94.6$ mm and $H = 31$ mm for $M_s = 1.42$ in atmospheric air at 293.0 K: **a** #86092103, $M_s = 1.421$; **b** #86092105, $M_s = 1.438$; **c** #86092108, $M_s = 1.430$; **d** #86092109, $M_s = 1.435$; **e** #86092111, 410 μ s, $M_s = 1.432$; **f** enlargement of (e); **g** #86092112, $M_s = 1.423$; **h** #86092116, $M_s = 1.443$

Fig. 5.22 Logarithmic spiral shape



conventional shock tube. When the duct inclination angle of θ_w is smaller than the critical transition angle θ_{crit} , the reflection pattern is always a SMR. Hence the triple points of reflected shock waves along the upper and lower walls intersect and eventually merge at the end of the area contraction. Meantime, resulting reflected shock waves RS and slip lines SL repeatedly interact and move toward the end of the V-shaped duct.

5.5.1 V-Shaped Area Contraction

In August 1985, the B747 of JAL Flight 123 clashed against a mountain and over 500 passengers were killed. The B747’s pressure bulkhead was ruptured while cruising, resulting in blown-off of the vertical rudder. The B747 lost control and crashed. The cabin pressure was higher than the pressure at the cruising altitude. The pressure bulkhead worked as a diaphragm in a shock tube sustaining this pressure difference. Therefore, its rupture generated a shock wave, which was not a planar shock wave but propagated into the space inside the vertical tail. As this structure had an area contraction, the pressure there increased high enough to blow-off the vertical rudder.

For checking the dependence of area reduction on the resulting pressure amplification, Shock wave strengths were amplified propagating in a duct of area contractions. V-shaped area contractions of 30° , 60° , 90° , 120° were installed in the $60\text{ mm} \times 150\text{ mm}$ conventional shock tube and tested for various shock strengths. In Fig. 5.27, the SMR is reflected from these area contractions.

5.5.1.1 Angle 30°

Figure 5.27 shows the evolution of the shock wave reflection and focusing along 30° area contraction for for $Ms = 1.30$ in atmospheric air at 289.3 K . Multiple reflections of the triple points and vortices enhanced pressures stepwise are visible in Fig. 5.27f (Figs. 5.28, 5.29).

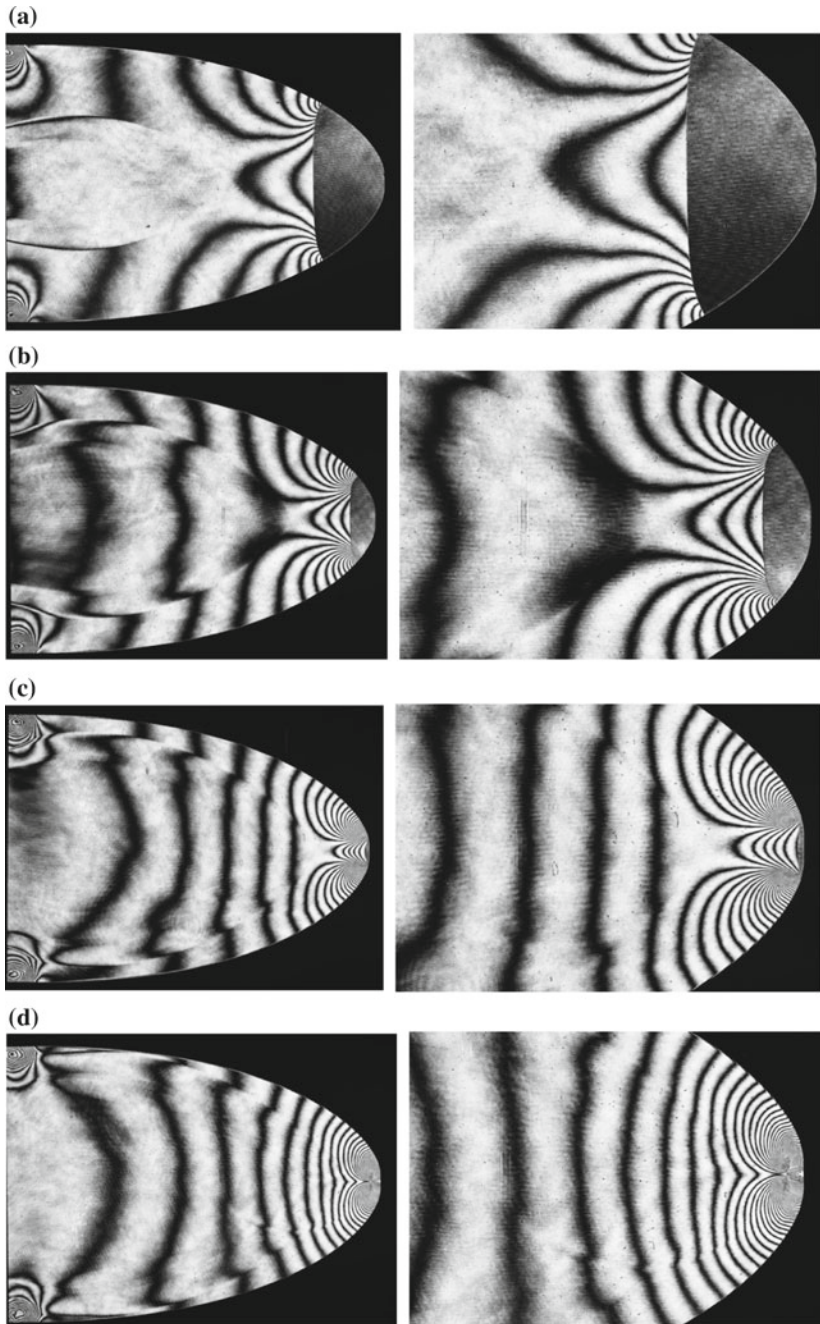


Fig. 5.23 The evolution of shock wave focusing from a log-spiral passage for $M_s = 1.40$ in atmospheric air at 294.8 K, comparison with enlarged images: **a** #86100909, 370 μs from the trigger point, $M_s = 1.396$; **b** #86100803, 390 μs , $M_s = 1.396$; **c** #86100804, 400 μs , $M_s = 1.398$; **d** #86100805, $M_s = 1.383$; **e** #86100808, 407 μs , $M_s = 1.389$; **f** #86100806, 410 μs , $M_s = 1.398$; **g** #86100809, 415 μs , $M_s = 1.390$; **h** enlargement of (**d**)

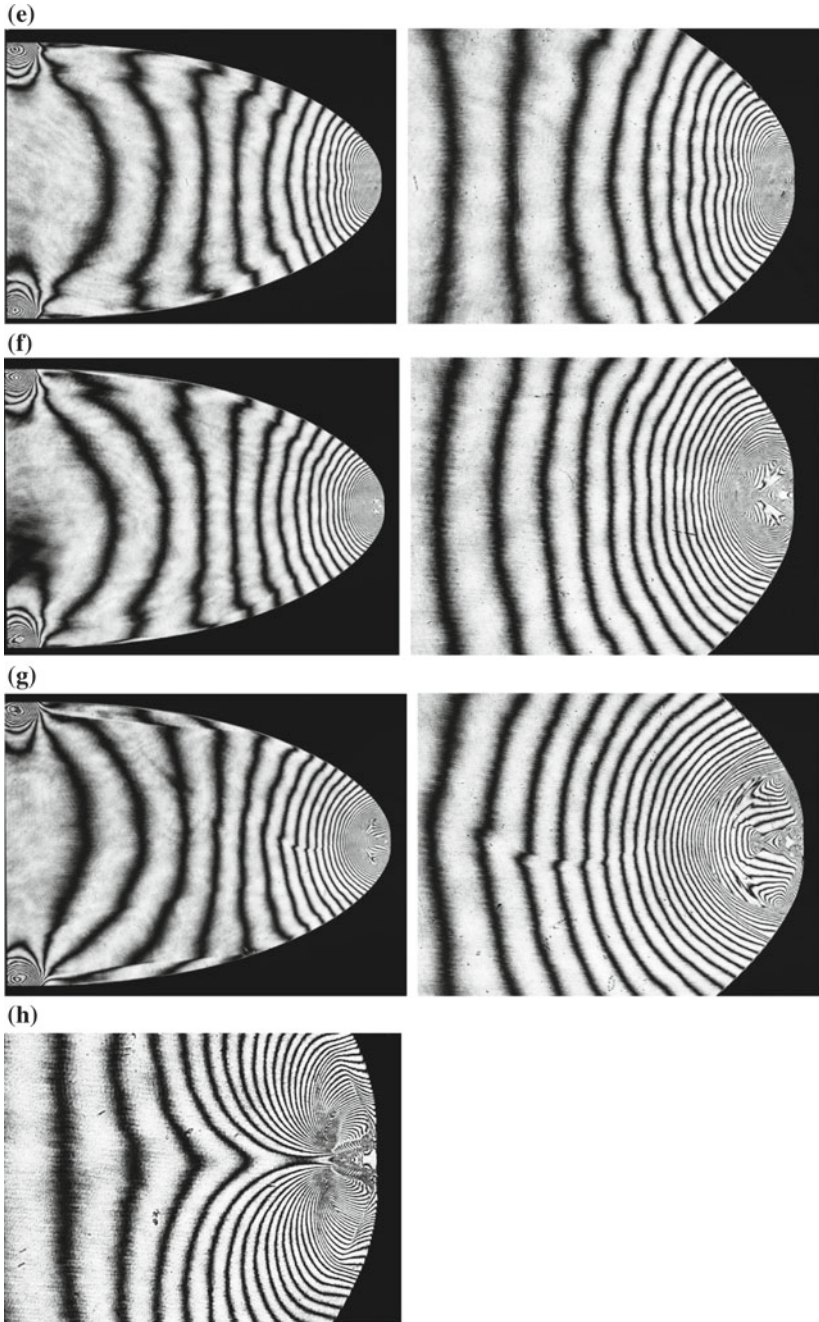


Fig. 5.23 (continued)

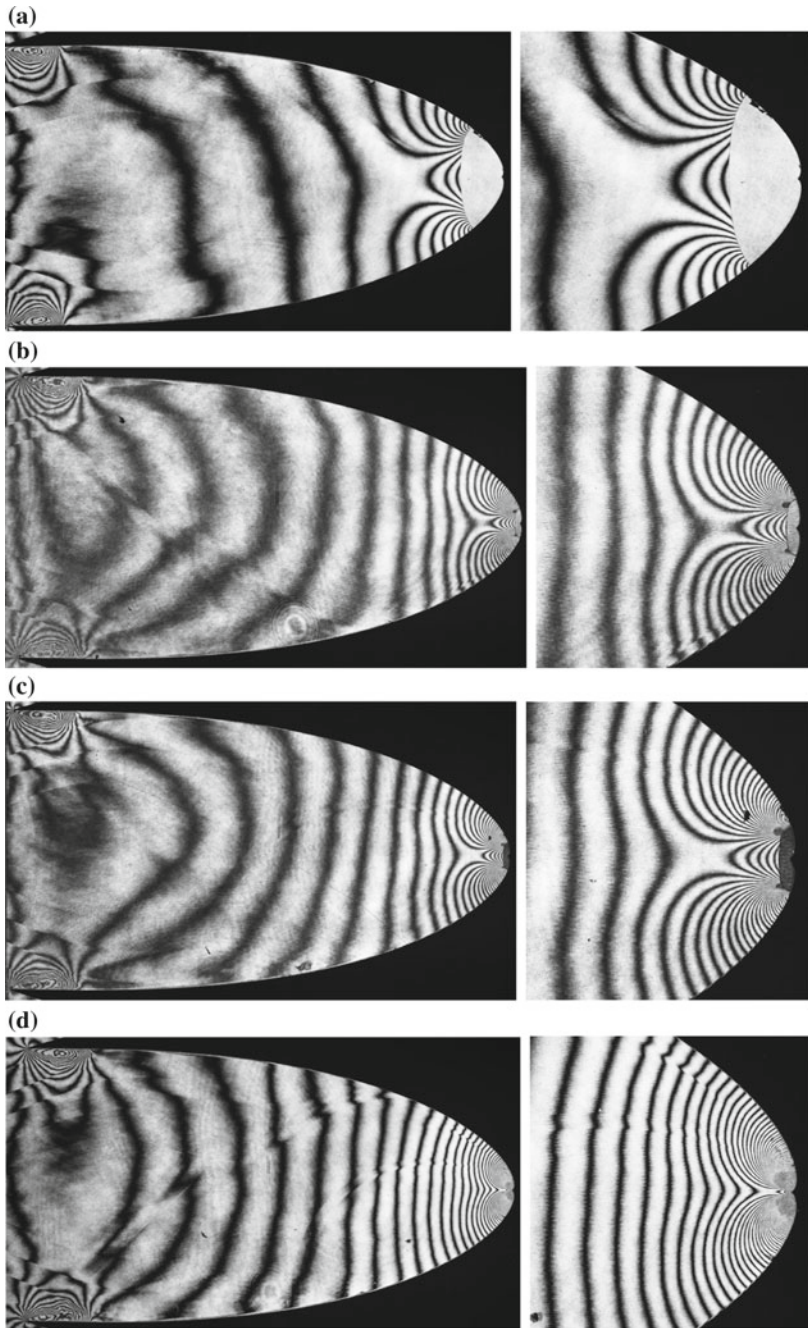


Fig. 5.24 The evolution of the shock wave focusing from a log-spiral passage for $M_s = 1.480$ in air at 900 hPa, 287.1 K: **a** #86112713, 495 μs from trigger point, $M_s = 1.479$; **b** #86112707, 510 μs , $M_s = 1.480$; **c** #86112712, 500 μs , $M_s = 1.476$; **d** #86122711, 505 μs , $M_s = 1.475$; **e** #86122708, 515 μs , $M_s = 1.480$; **f** #86122709, 517 μs , $M_s = 1.276$

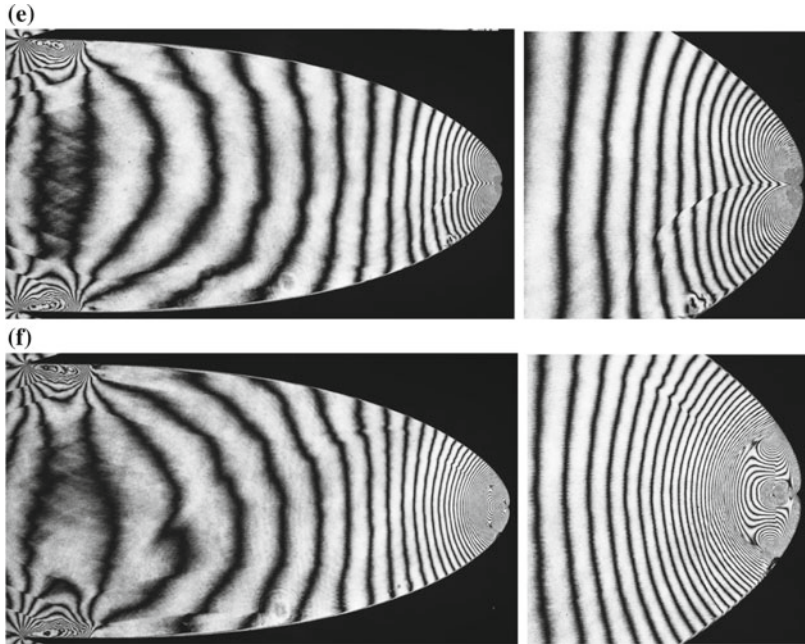


Fig. 5.24 (continued)

5.5.1.2 Angle 60°

Figure 5.30 shows the evolution of the shock wave focusing from 60° area contraction for $M_s = 1.27$ in atmospheric air at 290.3 K. Propagating toward the tip, the transmitting shock waves interacted repeatedly along the upper and lower walls and enhanced the pressure discontinuously behind the interacting shock wave. Although the procedure of shock wave interaction is simple, it contains complex shock dynamic effects. Figure 5.31a–i show the same V-shape angle but higher $M_s = 2.17$. The intersection of the TP from the upper and lower walls accompany SL. The convergence of the SL and their interactions are observed in Fig. 5.31i.

5.5.1.3 Angle 90°

Figure 5.32 show shock wave focusing from a 90° area contraction placed in a 60, 150 mm shock tube for $M_s = 1.27$ in atmospheric air at 287.4 K. The reflection patterns are SbRR and hence the pressure enhancement is caused simply by repeated reflection of oblique shock waves.

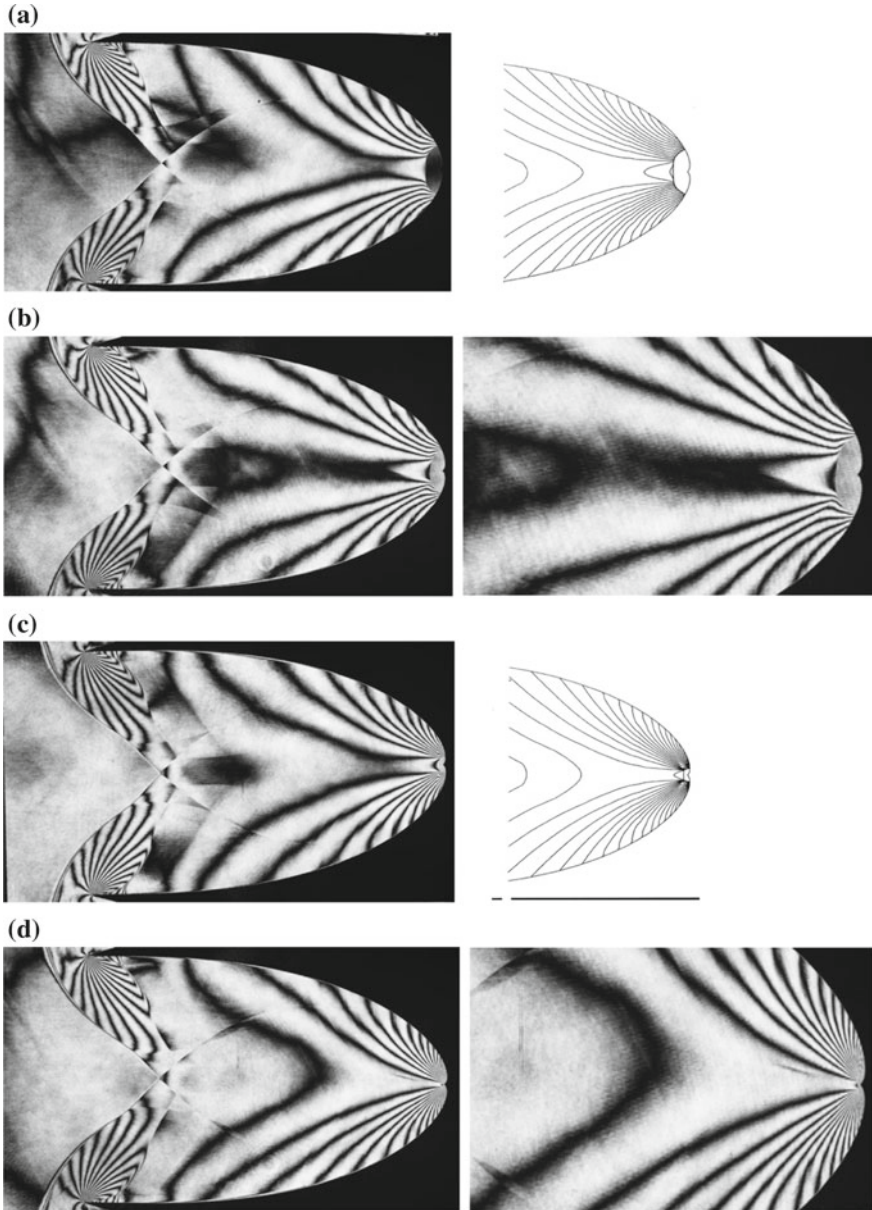


Fig. 5.25 Evolution of shock wave focusing from a log-spiral passage for $M_s = 2.70$ in air at 110 hPa, 287.0 K: **a** #86112812, 510 μs from trigger point, $M_s = 2.722$; **b** #86112808, 500 μs , $M_s = 2.739$; **c** #86112811, 507 μs , $M_s = 2.722$; **d** #86112809, 505 μs , $M_s = 2.698$; **e** #86112813, 510 μs , $M_s = 2.723$; **f** #86112814, 510 μs , $M_s = 2.723$; **g** enlargement of (**f**)

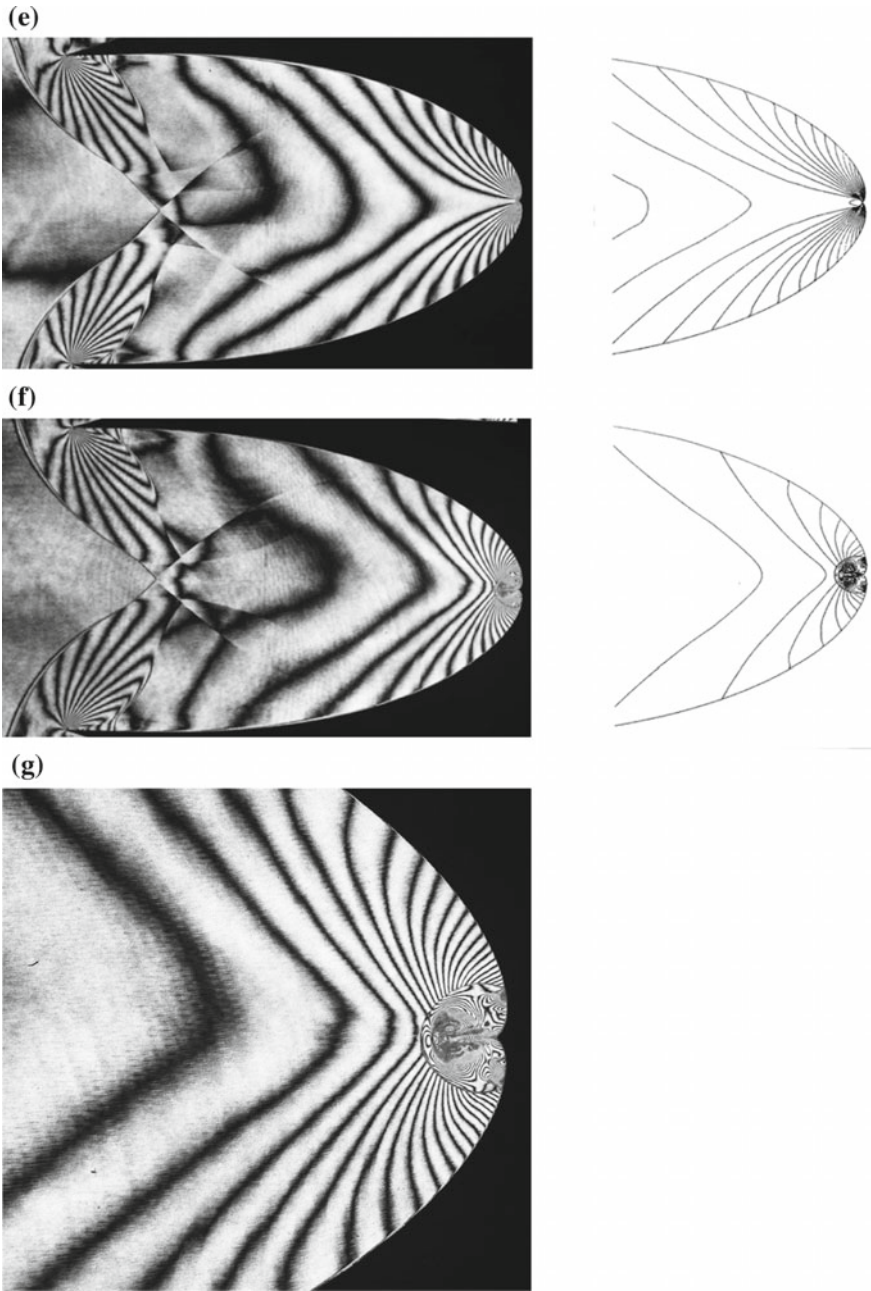


Fig. 5.25 (continued)

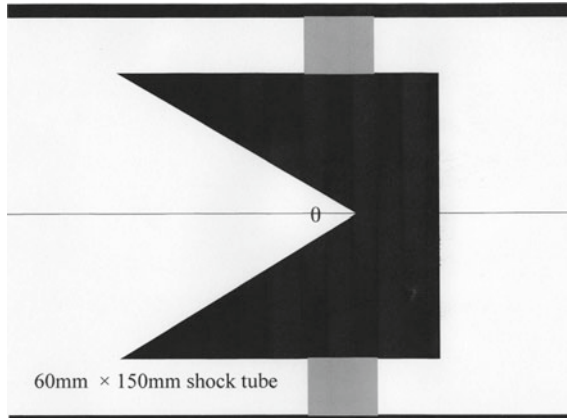


Fig. 5.26 V-shaped duct, $\theta = 30^\circ, 60^\circ, 90^\circ, 120^\circ$

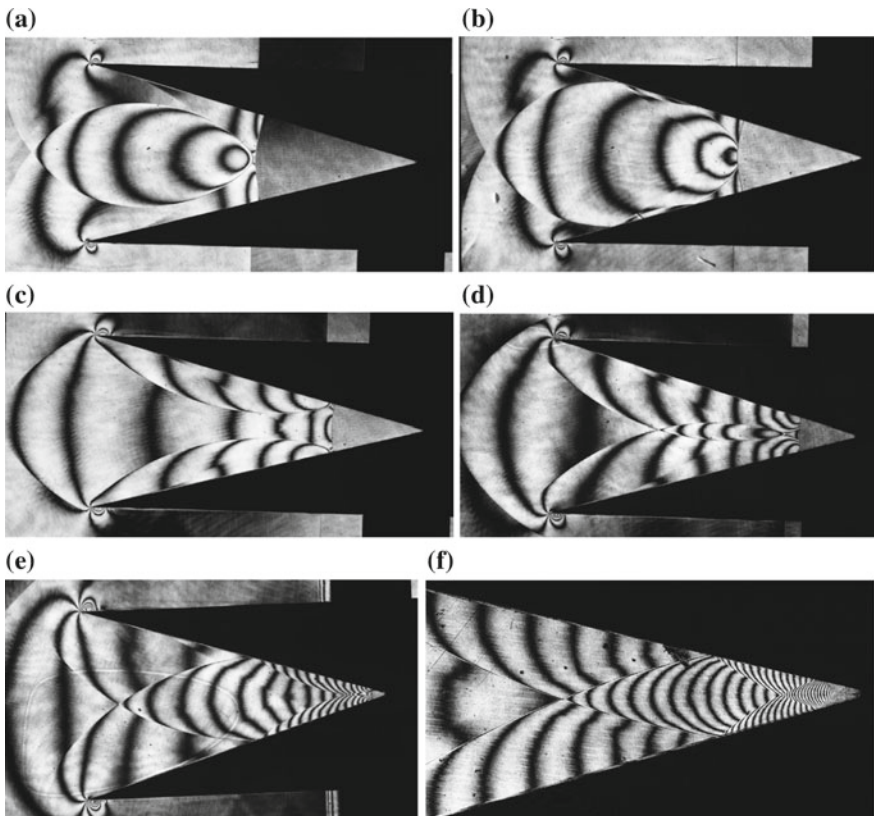


Fig. 5.27 The evolution of the shock wave focusing along 30° shaped area contraction for $M_s = 1.30$ in atmospheric air at 289.3 K: **a** #88020220, 260 μs from trigger point, $M_s = 1.301$; **b** #88020218, 280 μs , $M_s = 1.299$; **c** #88020216, 310 μs , $M_s = 1.301$; **d** #88020224, 330 μs , $M_s = 1.303$; **e** #88020227, 360 μs , $M_s = 1.299$; **f** #88020228, 370 μs , $M_s = 1.301$

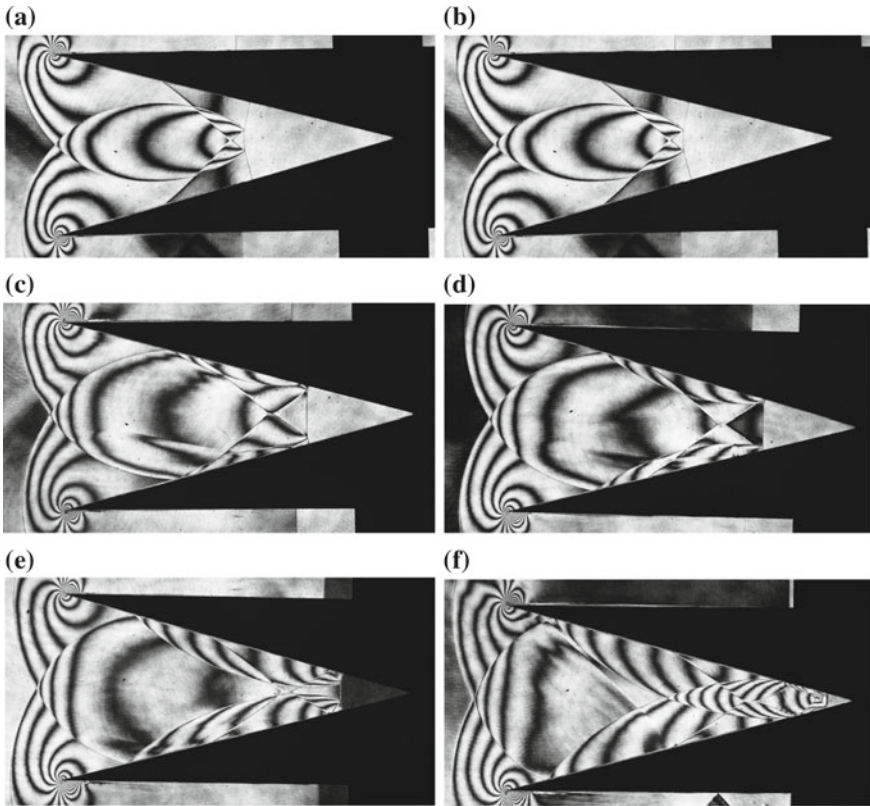


Fig. 5.28 The evolution of the shock wave focusing along 30° shaped area contraction for $M_s = 1.60$ in air at 600 hPa, 289.5 K: **a** #88020301, 80 μs , $M_s = 1.685$; **b** #88020303, 90 μs , $M_s = 1.682$; **c** #88020305, 110 μs , $M_s = 1.686$; **d** #88020307, 120 μs , $M_s = 1.685$; **e** #88020308, 130 μs , $M_s = 1.674$; **f** #88020309, 140 μs , $M_s = 1.607$

5.5.1.4 Angle 120°

In Fig. 5.33, a SPRR appears on the wedge surface. Their reflection pattern created a stepwise pressure enhancement on the wall surface.

5.6 Conical Area Convergence

Figure 5.34 shows a 10° conical area converging section made of acrylic. In order to quantitatively visualize the shock wave propagation through the test section, it has an aspheric lens shape which enables to quantitatively visualize the flows in a circular cross sectional duct. It had 50 mm in diameter and connected to the 50 mm diameter shock tube.

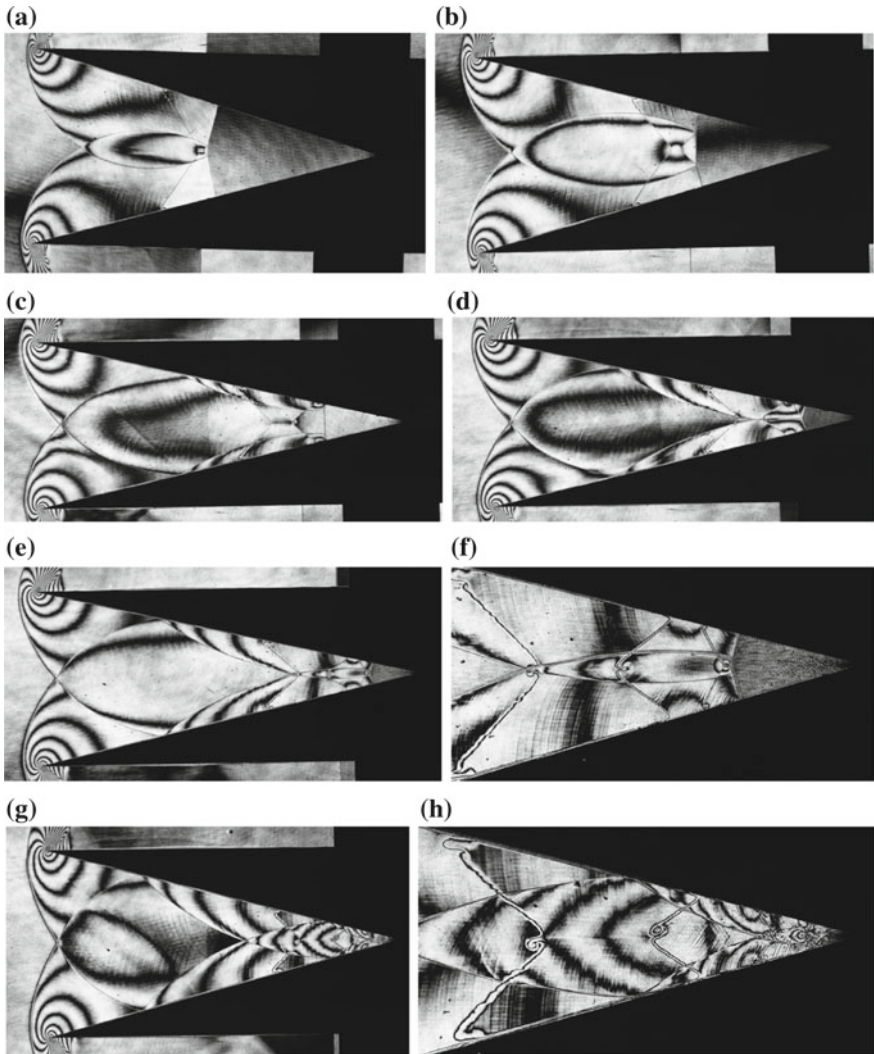


Fig. 5.29 The evolution of shock wave focusing from 30° area contraction for $M_s = 2.10$ in air at 300 hPa, 291.5 K: **a** #88020318, 290 μs from trigger point, $M_s = 2.169$; **b** #88020320, 310 μs , $M_s = 2.142$; **c** #88020321, 320 μs , $M_s = 2.180$; **d** #88020322 350 μs , $M_s = 2.154$; **e** #88020323, 340 μs , $M_s = 2.157$; **f** enlargement of (e); **g** #88020324 350 μs , $M_s = 2.159$; **h** enlargement of (g)

The shock wave propagation in a 10° (half apex angle) conical test section was visualized using double exposure holographic interferometry and diffuse holography as well. The pattern of the transmitting shock wave is, in principle, identical with the shock wave propagation from a shallow V shaped duct. Therefore, the reflection pattern of the shock wave will be a SMR. However, unlike two-dimensional shock tube flows, neither the reflected shock wave, RS, nor the

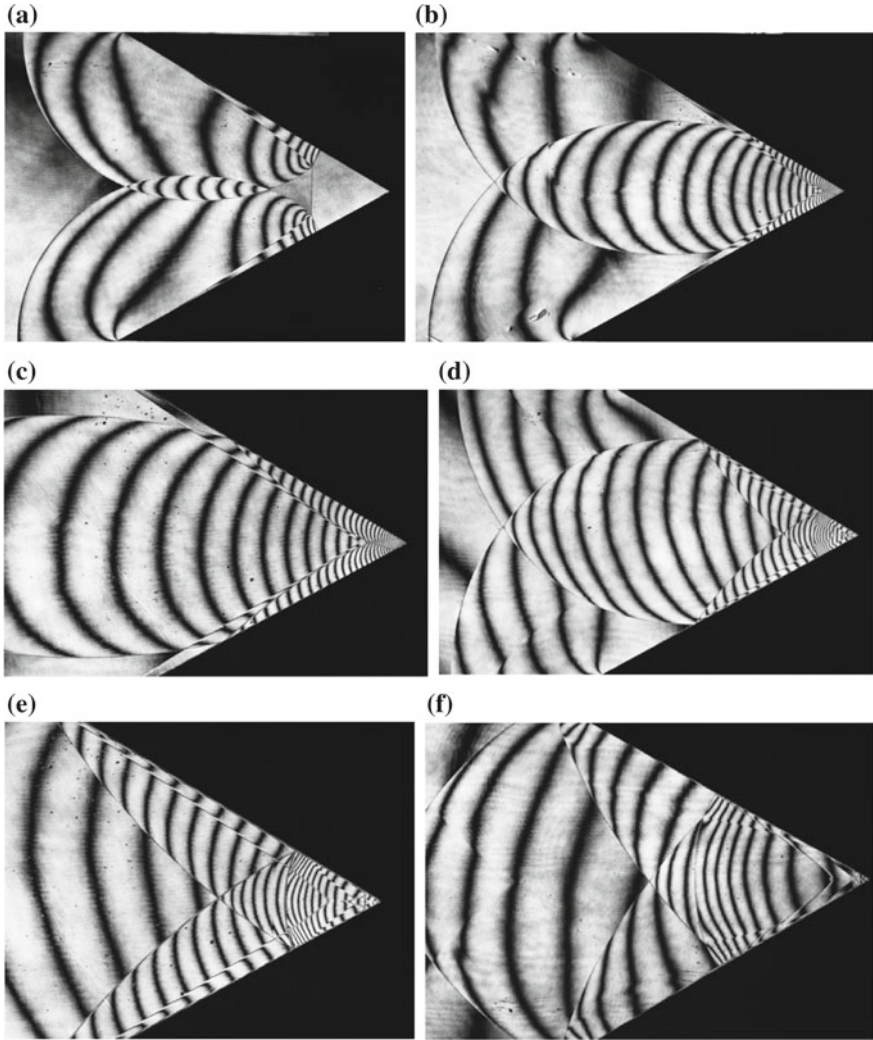


Fig. 5.30 Evolution of shock wave focusing from 60° area contraction for $M_s = 1.27$ in atmospheric air at 290.3 K: **a** #88020202, 330 μs from trigger point, $M_s = 1.274$; **b** #88020206, 380 μs , $M_s = 1.274$; **c** enlargement of **(b)**; **d** #88020209, 410 μs , $M_s = 1.274$; **e** enlargement of **(d)**; **f** #88020214, 500 μs , $M_s = 1.266$; **g** enlargement of **(f)**

slip line, SL are distinctly visible. At the shock front, the loop formed by the intersection of the triple point, TP, and the Mach stem, MS, is the distinctly observed. Hence the trajectories of the TP are recognized correctly as seen in Fig. 5.35a, b. Figure 5.35b is a single exposure interferogram Milton (1989). Figure 5.35c, d shows the second stages of the reflection.

Figure 5.36 summarizes triple point trajectories. The triple points intersect and converge, in other words, focus. Then the shock wave started diverging.

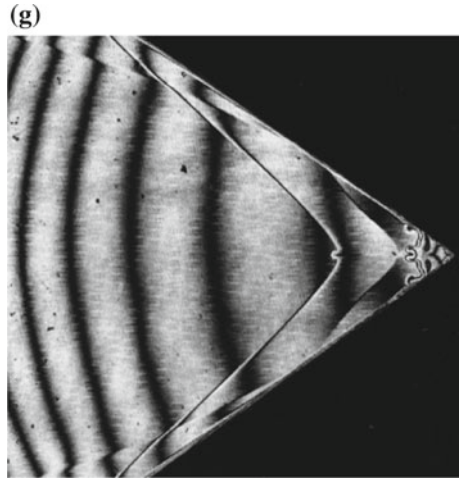


Fig. 5.30 (continued)

Figure 5.35c, d correspond to the stage of diverging shock waves. But the patterns so far observed was not clear. Figure 5.37 shows shock wave convergence in a 10° – 20° combined duct for $M_s = 1.46$ in air.

Figure 5.38 shows the shock wave propagation along a duct having 10° and 20° combined area convergence. Figure 5.38a shows a single exposure interferogram for $M_s = 1.46$ in air at 750 hPa 289.7 K. Figure 5.38b Summarizes the evolution of triple point trajectories for $M_s = 1.46$.

5.7 Circular Co-axial Annular Shock Wave Focusing

5.7.1 Horizontal Annular Co-axial Shock Tube

The convergence of a cylindrical or spherical shock wave into a spot is named an implosion, while the divergence of a shock wave from a point source is called explosion. Guderley (1942) studied analytically the implosion of shock wave and derived a self-similar solution. Perry and Kantrowitz (1951) experimentally investigated the convergence of annular coaxial shock waves. In this experiment, the annular co-axial planar shock wave smoothly diffracted over an axisymmetric tear drop shaped inner core placed at the end of horizontal shock tube. They visualized the converging cylindrical shock waves using shadowgraph system and discussed the stability of converging shock waves.

Regarding the convergence of annular shock waves, experiments were carried out, for example, by Wu et al. (1978), Hoshizawa (1987), Neemeh and Less (1990), Watanabe (1993), and Apazidis et al. (2011). Knystautus and Lee (1971) investigated the convergence of detonation waves in an annular detonation tube, which

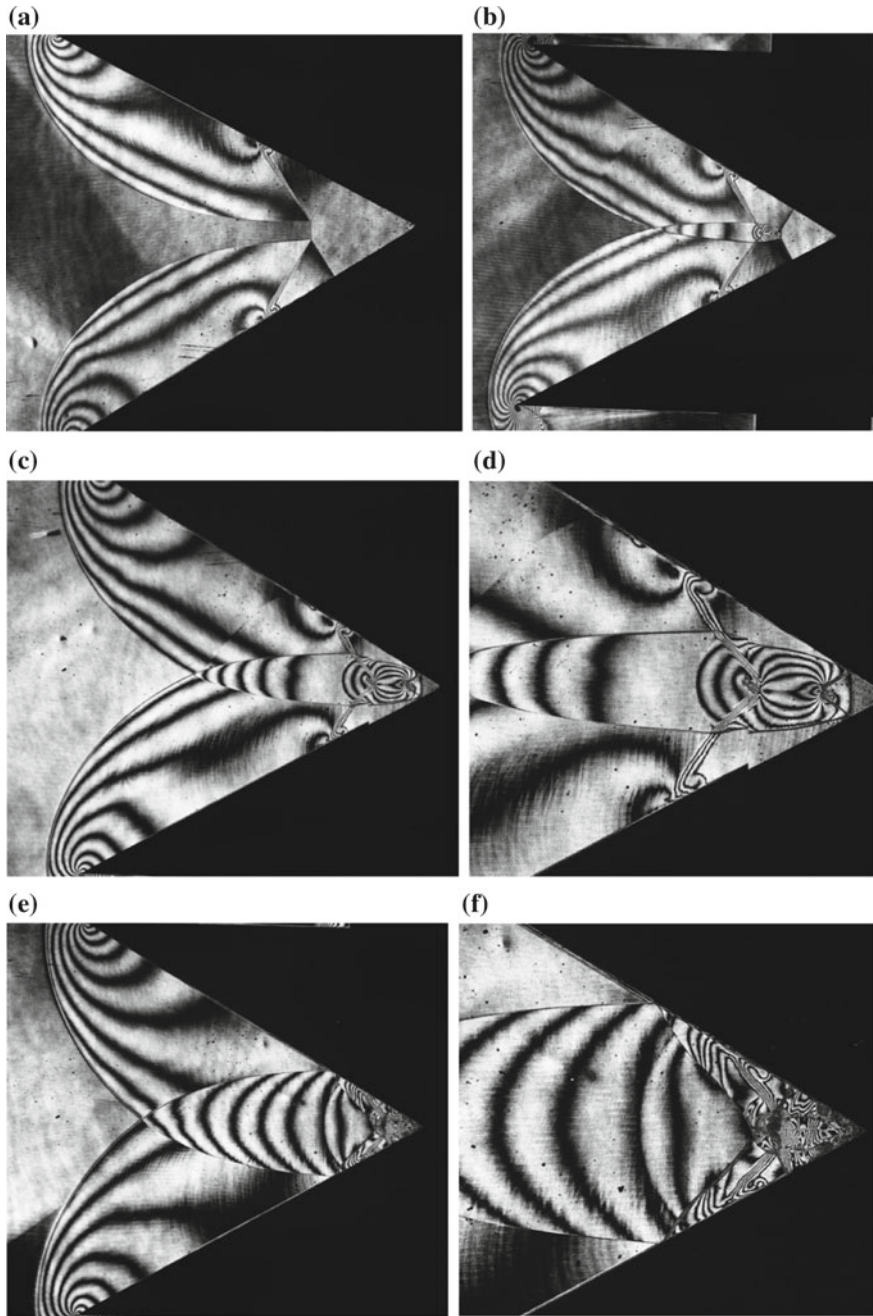


Fig. 5.31 The evolution of shock wave focusing from 60° area contraction for $M_s = 2.17$ in air at 300 hPa, 288.6 K: **a** #88020403, 340 μs from trigger point, $M_s = 2.169$; **b** #88020404, 350 μs , $M_s = 2.152$; **c** #88020405, 360 μs , $M_s = 2.152$; **d** enlargement of (c); **e** #88020406, 370 μs , $M_s = 2.140$; **f** enlargement of (e); **g** #88020409, 370 μs , $M_s = 2.152$; **h** enlargement of (g); **i** #88020411, 400 μs , $M_s = 2.129$

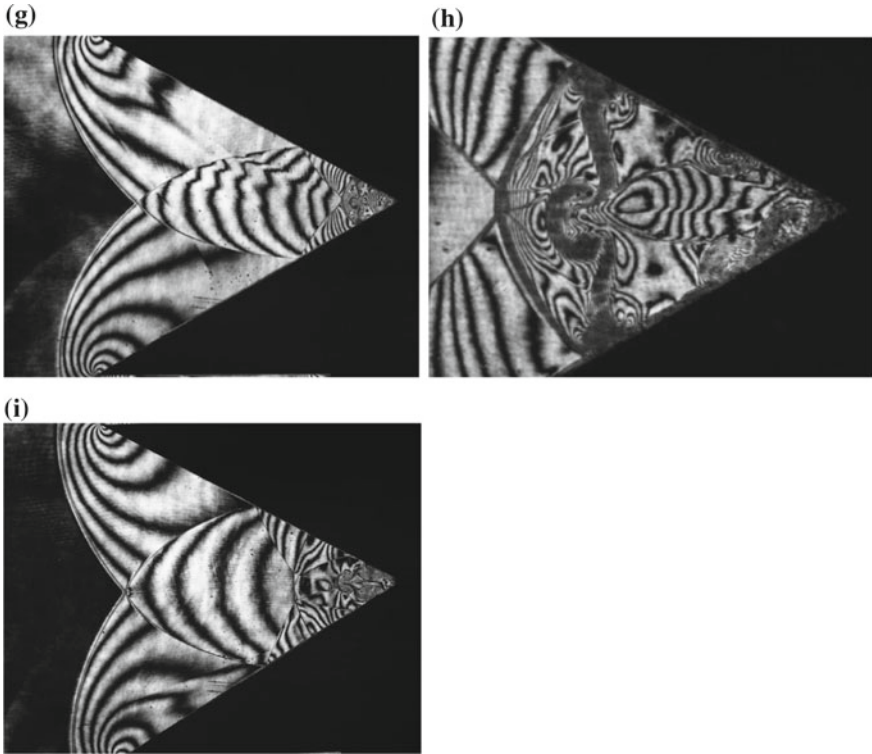


Fig. 5.31 (continued)

had the similar structure to that of Perry and Kantrowitz (1951). They observed the spiral shaped soot patterns over the plane where the detonation wave converged. Using a similar facility reported by Knystautus and Lee (1971), Fujiwara et al. (1979) observed the luminous emission at the center of converging detonation waves. Terao (1973) investigated the converging detonation wave using a very large 800 mm diameter detonation chamber and also observed converging detonation waves propagating at a velocity exceeding the Chapman-Jouget detonation velocity. He witnessed the generation of a very high pressure at the spot of the center of convergence.

Figure 5.38 illustrates a 500 mm long, a 210 mm inner diameter, and a 230 mm outer diameters annular co-axial test section Hoshizawa (1987). It was connected to a 50 mm diameter conventional shock tube was connected via a 45° conical section to the test section. The inner cylinder was supported by two pairs of two-18 mm diameter cylindrical struts located at the S_1 and S_2 , as seen in Fig. 5.38. The struts diffracted the transmitting shock wave and created wakes in the flow behind the transmitted shock wave. Therefore, in order to suppress these flow disturbances, the test section was 500 mm long. Two pressure transducers were installed at the position of P_1 and P_2 .

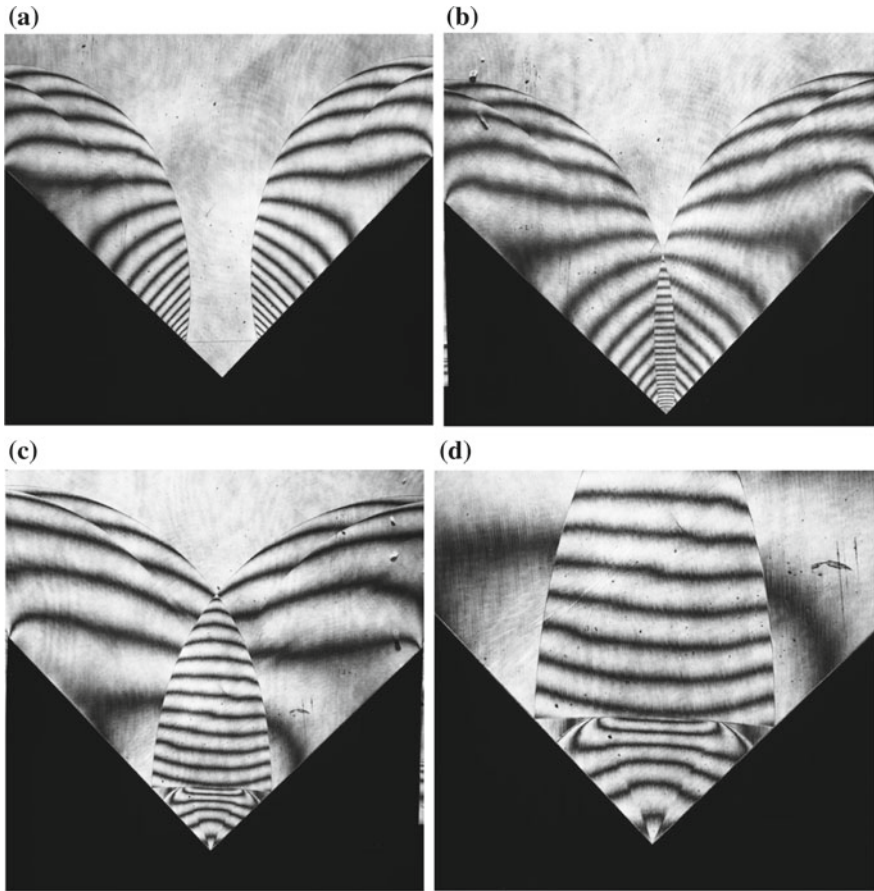


Fig. 5.32 The evolution of shock wave convergence from 90° reflector for $M_s = 1.27$ in atmospheric air at 287.4 K: **a** #88020114, 370 μ s from trigger point, $M_s = 1.282$; **b** #88020114, 370 μ s, $M_s = 1.282$; **c** #88020115 420 μ s, $M_s = 1.275$; **d** enlargement of (c)

The interval between the inner and outer tubes was 10.0 ± 0.02 mm. The blockage ratio of the struts to the annular shock tube cross section was 0.12. At the end of the test section, an annular co-axial 90° bend was connected, its inner and outer radii of which were 2.5 and 12.5 mm, respectively. The result of the previous experiment with the two-dimensional bends Honda et al. (1977) were used for having the optimal shape of the present bend. A 130 mm diameter glass plate was placed on the outside end wall and a 130 mm diameter aluminum plated glass mirror was placed on the inside end wall. In the experiments, the ring shaped shock wave turning 90° and the end of the straight test section eventually became an annular co-axial converging shock wave in a similar manner as described in Perry and Kantrowitz (1951). This arrangement smoothly re-directed a ring shaped shock wave to a co-axial converging shock wave and suppressed the flow non-uniformity the struts created. However, the passage through the co-axial bend diffracted and

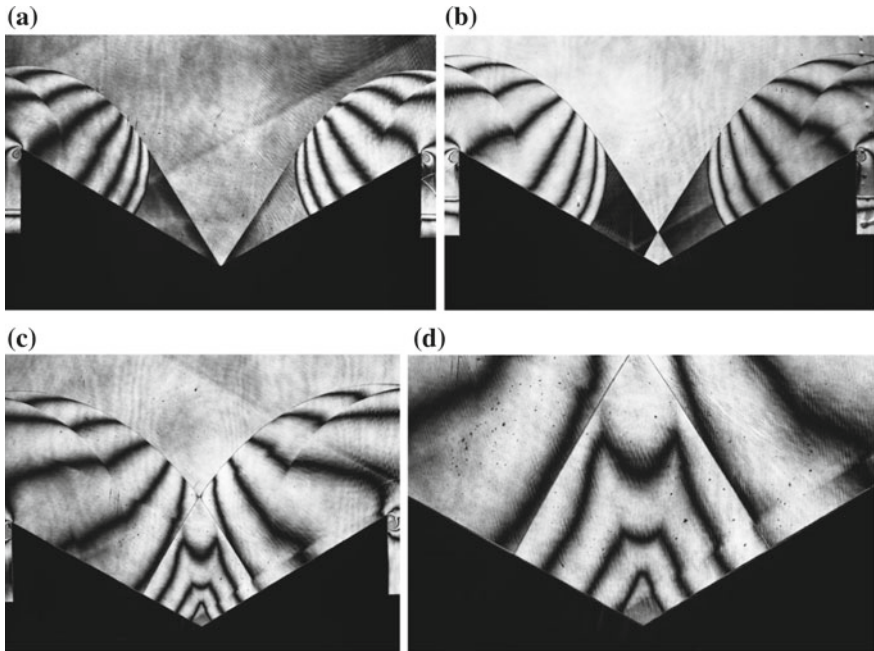
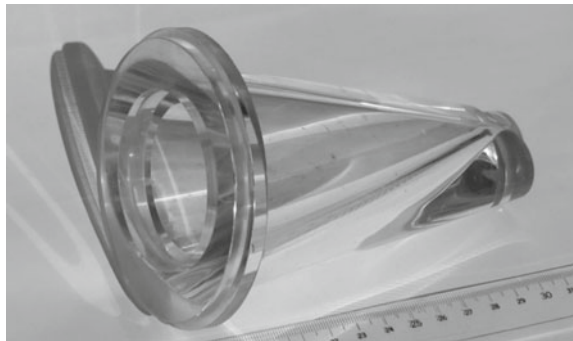


Fig. 5.33 Evolution of shock wave convergence from 120° area contraction for $M_s = 1.16$ in atmospheric air at 287.0 K: **a** #88020106, 460 μs from trigger point, $M_s = 1.153$; **b** #88020107, 470 μs , $M_s = 1.162$; **c** #88020109 520 μs , $M_s = 1.164$; **d** enlargement of (c)

Fig. 5.34 A 10° (half apex angle) conical test section



reflected the transmitting shock wave induced wavelets, which propagated behind the converging shock wave. The test gas was air at the initial pressure ranging from 50 hPa to 100 kPa. Visualization was conducted by double exposure Twyman-Green interferometry Takayama (1983).

Perry and Kantowitz (1951) concluded, from results of their visualization, that the convergence of weak annular co-axial cylindrical shock waves was stable. However, in our double exposure holographic interferometric observations, it was not always achievable. The initial disturbances created by the reflection of shock

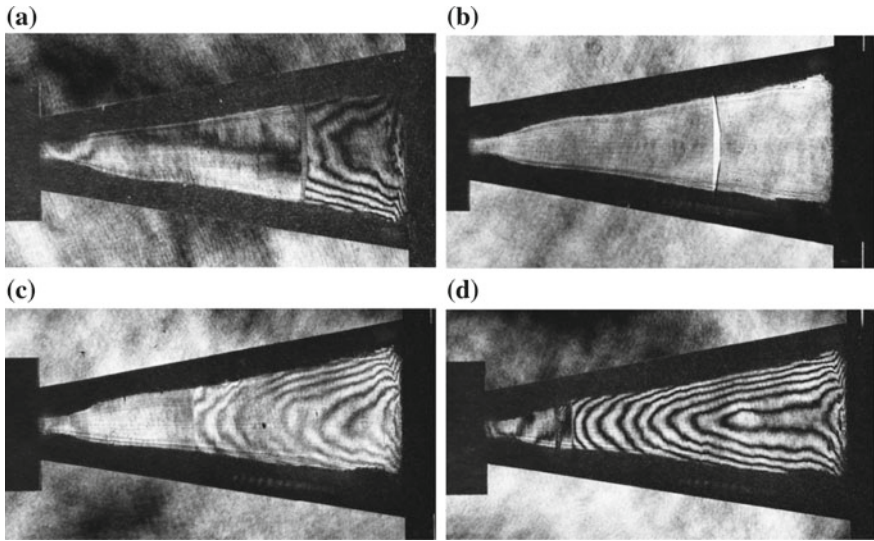
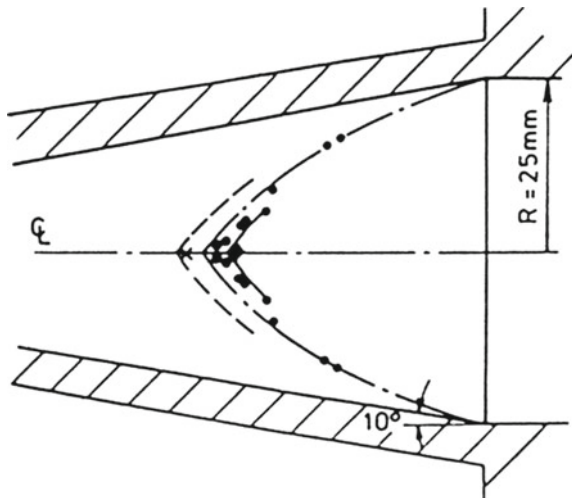


Fig. 5.35 Shock wave propagation along a 10° area convergence for $Ms = 1.74$ in air at 500 hPa, 288 K: **a** #84122701, 60 μs from trigger point. Notice the IS propagating from the right to the left; **b** #84122704, 62 μs , single exposure; **c** #84122605, 120 μs , $Ms = 1.742$; **d** #84122610, 150 μs , $Ms = 1.742$

Fig. 5.36 Triple point trajectories in the 10° area convergence for $Ms = 1.73$ (Milton 1989)



wave reflection from the struts and its connection with wakes hardly disappeared from the flow. These flow perturbations affected the annular shock wave and prevented its focusing. The presence of the four struts resulted in flow instability that prevent proper converging of the annular shock wave.

Figure 5.39 shows the convergence process of annular co-axial shock wave convergence for $Ms = 1.38$ in CO_2 at 400 hPa and 295.0 K. As seen in Fig. 5.39a,

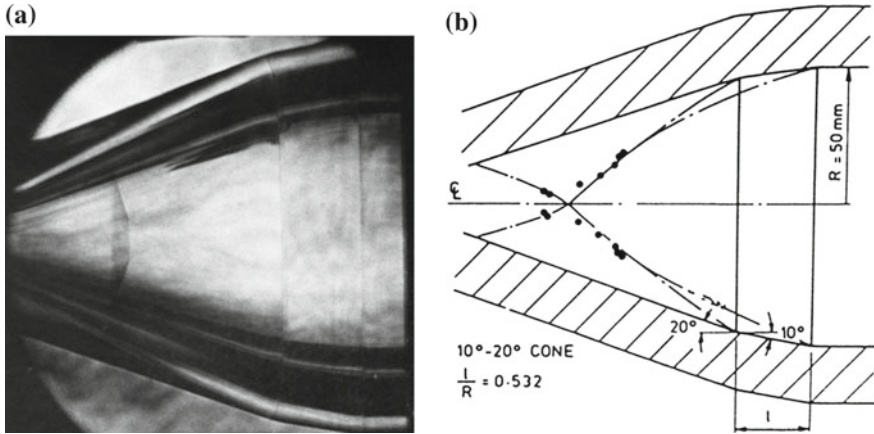


Fig. 5.37 Shock wave propagation along a $10^\circ\text{--}20^\circ$ combined duct and 50 mm diameter area convergence: **a** #84121228, $560 \mu\text{s}$ from trigger point, for $M_s = 1.456$ in air at 750 hPa 289.7 K, single exposure; **b** summary of triple point trajectory for $M_s = 1.46$ (Milton 1989)

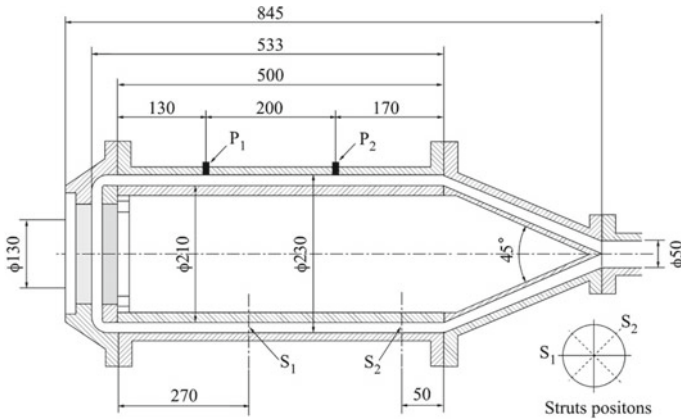


Fig. 5.38 The test section

the shape of the incident shock wave looks nearly cylindrical but shows a sign of mode-four perturbations. Figure 5.39b–d shows the development of the mode four perturbations and the deformation of the circular shock wave toward a square shape although not yet reachable in these interferograms. The four circular fringes attached to the converging shock wave increase their numbers with elapsed time representing the amplification of the initial disturbances. This created four pairs of triple points at the final stage of convergence. In Fig. 5.39e, the transmitted shock wave converged at the center but as the fringes are so densely populated so it is impossible to resolve them. When the transmitted shock wave converged and turned to the cylindrical diverging shock wave. Figure 5.39f shows the cylindrical

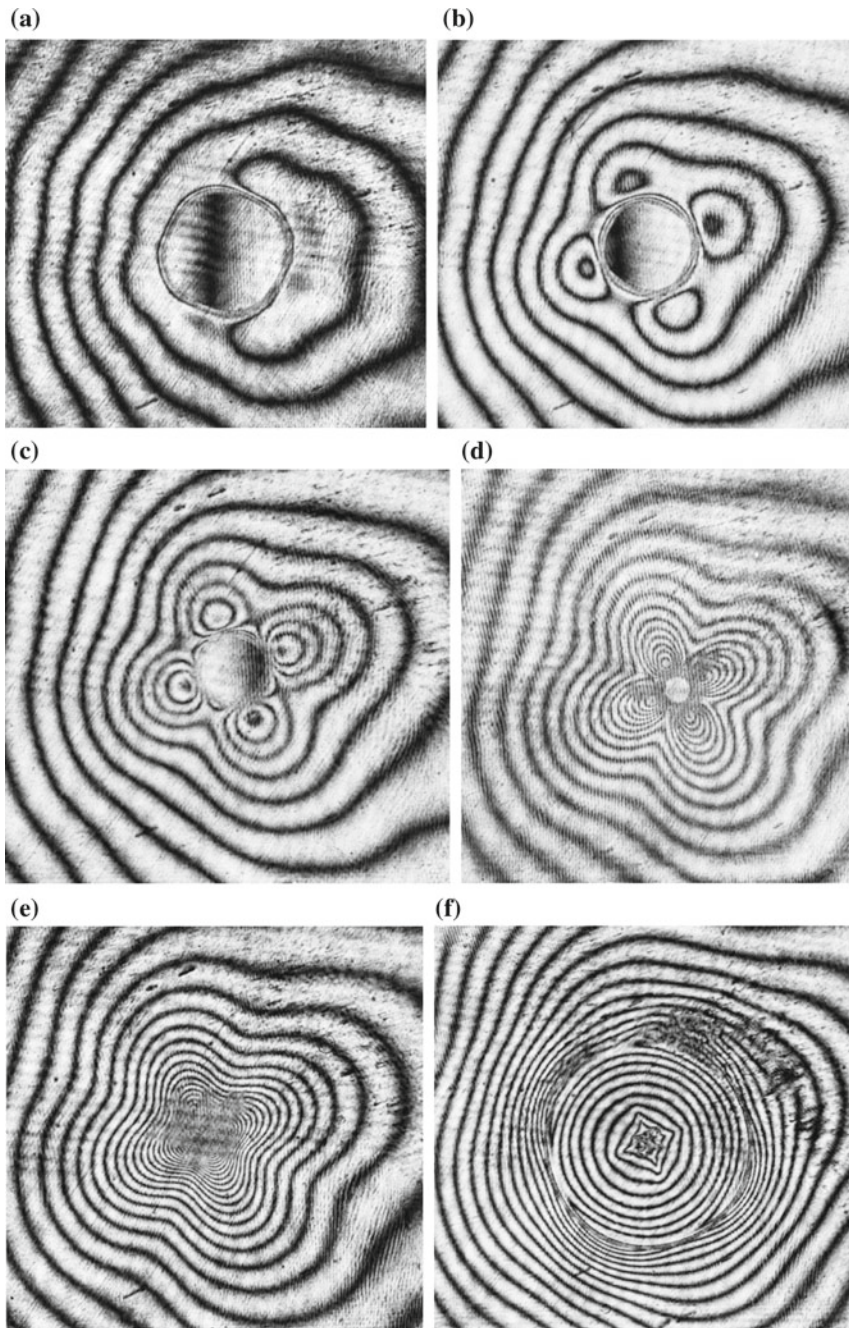


Fig. 5.39 The evolution of shock wave convergence in the test section shown in Fig. 5.37 for $M_s = 1.38$ in CO_2 at 400 hPa, 295.0 K: **a** #82051207, 280 μs from trigger point, $M_s = 1.373$; **b** #82051208, 330 μs , $M_s = 1.373$; **c** #82051205, 283 μs , $M_s = 1.373$; **d** #82051204, 285 μs , $M_s = 1.385$; **e** #82051210, 290 μs , $M_s = 1.386$; **f** #82051211, 310 μs , $M_s = 1.383$; **g** #82051213, 325 μs , $M_s = 1.386$

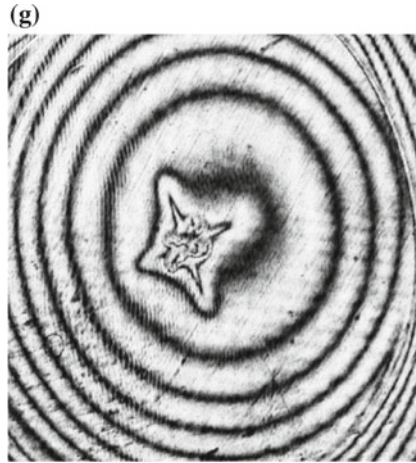


Fig. 5.39 (continued)

diverging shock wave. Behind the diverging shock wave the remnants of the vortices are visible at the center. Figure 5.40g shows the enlarged image. In Fig. 5.39g, the cross shaped remnants of four pairs of vortices are visible far behind the diverging shock wave.

Figures 5.40 show the evolution of a converging shock wave for $M_s = 2.00$ in air at 100 hPa and 298.5 K. In Fig. 5.40a, the shape of the shock wave was slightly deformed affected by mode-four disturbances. In Fig. 5.40b, d, the shock wave reached a square shape being composed of a SMR having four pairs of triple points at the four corners. Figure 5.40c is a magnified image of Fig. 5.40b. Four pairs of triple points consisting of three shock confluence and a slip line are clearly observable in the magnified photo. Figure 5.40e was taken a few μs after taking Fig. 5.40d, when the shock wave was converged and the shock wave just started diverging. The diverging shock wave was always stable. Figure 5.40g shows four pairs of vortices at the center behind the cylindrical diverging shock wave which were generated by the triple point interaction. Each pair of vortices had the same pattern as seen at the shock wave focusing from a concave circular reflector, for example, as seen in Fig. 5.3g.

Guderley (1942) derived a self-similar solution for imploding shock waves in ideal gas; he suggested the following form,

$$r/r_0 = (1 - t/t_0)^n$$

where r and t are averaged radial distance and the elapsed time, respectively. r_0 and t_0 are reference radius and time and n is a self-similar exponent. Streak recordings of shock wave focusing were conducted for incident shock wave for $M_s = 1.10$, 1.50, and 2.10 in air. Figure 5.41a shows the results obtained for $M_s = 1.5$ in air. A 1.0 mm wide slit was attached to, crossing the observation window glass. The

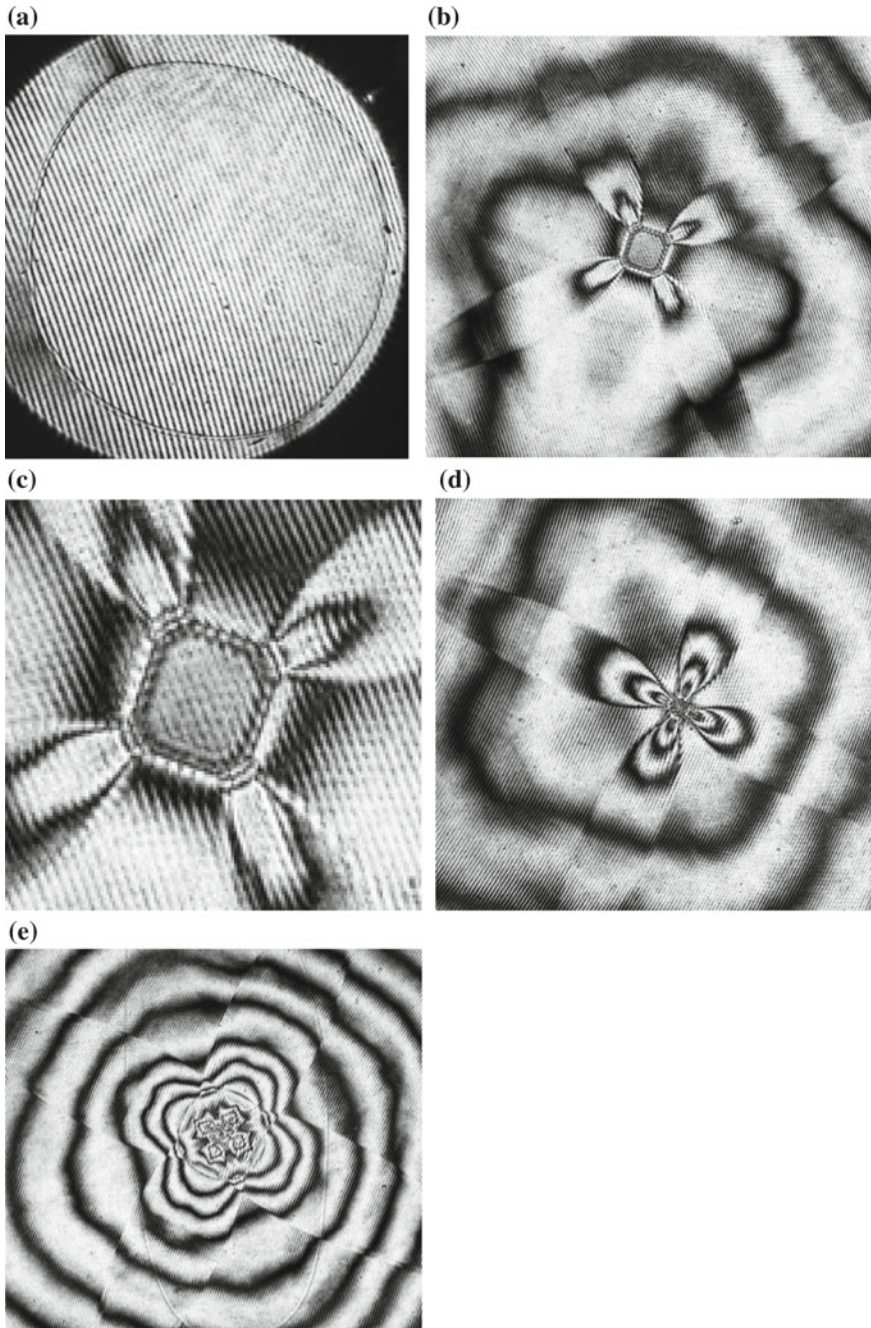


Fig. 5.40 The evolution of the shock wave convergence for $M_s = 2.00$ in air at 100 hPa, 298.5 K; **a** #89060903, 42 μs from trigger time, $M_s = 2.007$; **b** #89060718, 43 μs , $M_s = 2.043$; **c** enlargement of (c); **d** #89060716, 45 μs , $M_s = 2.043$; **e** #89060708, 46 μs , $M_s = 2.050$

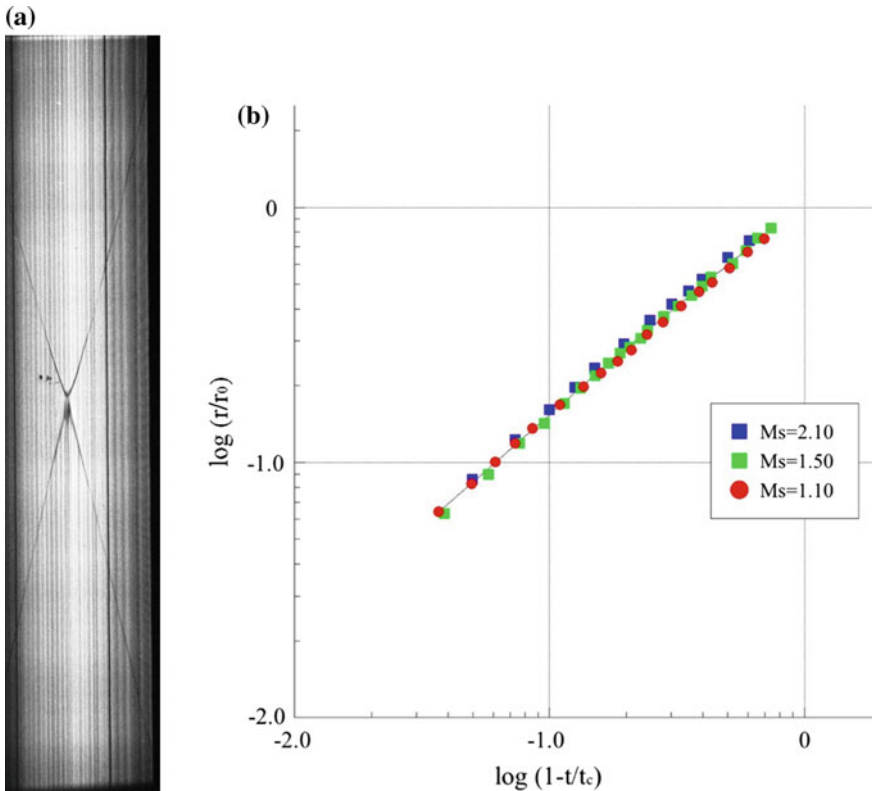


Fig. 5.41 A streak photograph of shock wave convergence: **a** #82061414, for $M_s = 1.5$. **b** Summary of streak recording of time variation of triple point trajectory data were collected from the tests #82061112 to #82061622. The self-similar exponent n varies from 0.828 to 0.833 (Hoshizawa 1987)

light source was an Argon-ion laser equipped with a mechanical shutter having the opening and closing time of about $100 \mu\text{s}$. Direct shadowgraph images of shock waves viewed through the slit were recorded by an ImaCon high speed camera operated in streak mode (John Hadland Ima Con 675). Recording speed was $1 \text{ mm}/\mu\text{s}$. The time is running from the bottom upward. When the shock wave converges, the shock wave diameter decreases quickly toward the point of convergence. The slightly dark shadows gradually generated behind the accelerating converging shock waves would indicate the formation of vortices and their accumulation; this can be observed in Fig. 5.40. Immediately after the implosion, the shock wave turned to a diverging wave. Measurements of the radius-time variations of the converging cylindrical shock waves are shown in the $x-t$ plane presented in Fig. 5.41a; both the radii and the elapsed time were plotted in a logarithmic plane.

Figure 5.41b summarizes the results of the streak recordings conducted from tests #82061112 to #82061622. The ordinate denotes the non-dimensional radius $\log_e(r/r_0)$ and the abscissa denotes the non-dimensional time $\log_e(1 - t/t_0)$. The time variations of the radius are displayed for $Ms = 1.1, 1.5$ and 2.1 in the $x-t$ plane. The self-similar exponents were deduced from this display; n is 0.828 for $Ms = 1.1$, n is 0.830 for $Ms = 1.5$, and n is 0.833 for $Ms = 2.1$, whereas Guderley's (1942) analytically derived $n = 0.835$ for $\gamma = 1.4$. Terao (1973), based on his detonation wave focusing chamber, obtained $n = 0.82$. The present results Hoshizawa (1987) agree well with previous results.

In reality the converging cylindrical shock waves were deformed by the exposure to the perturbation from behind as seen in Fig. 5.40. Hence the shape would be deformed from a circular shape. From the sequential interferograms, deviations of the local radius Δr from the average radius R could be readily obtained. Figure 5.42 summarizes the normalized $\Delta r/R$ during the shock wave convergence. The ordinate denotes the normalized $\Delta r/R$ and the abscissa denotes the averaged radius R in mm for $Ms = 1.1, 1.5$ and 2.1 . As seen in Figs. 5.39, 5.40, $\Delta r/R$ increases with decreasing in R . The trend is nearly independent of the Ms .

5.7.2 Vertical Annular Co-axial Shock Tube

The mode-four instability shown in Fig. 5.42 is a direct result from the presence of four struts which were supporting the horizontal inner core as shown in Fig. 5.38. In order to construct an annular shock tube without using the struts, Watanabe (1993) constructed a vertical annular co-axial shock tube composed from a 230 mm inner diameter and a 210 mm outer diameter tube as seen in Fig. 5.43. The shock tube had a massive and rigid structure sustaining its vertical position by itself. The shock tube had a high pressure driver section and a low pressure channel; a piston

Fig. 5.42 Dimensionless deformation of converging shock waves in air $\Delta r/R$ and averaged radius R (Hoshizawa 1987)

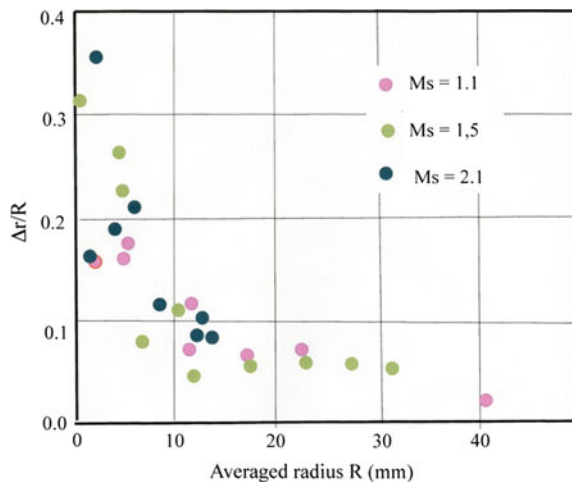
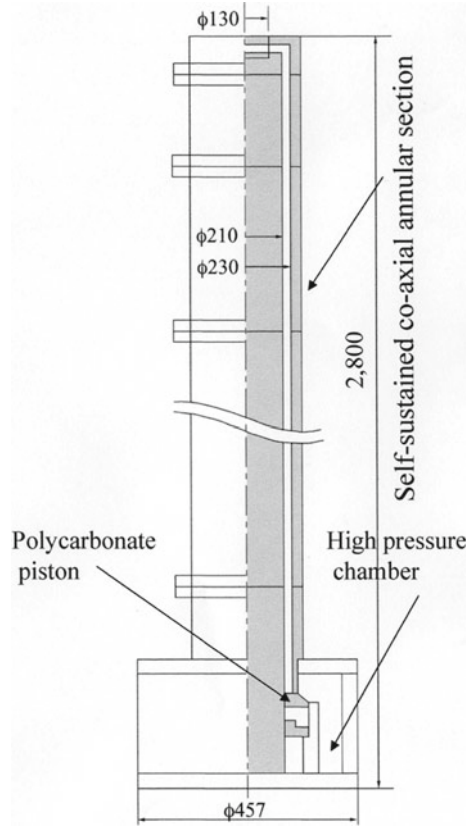


Fig. 5.43 The first generation diaphragm-less vertical annular co-axial shock tube (Watanabe 1993)



driving mechanism was used for separating between the two sections of the shock tube.

The high pressure helium was filled into the driver chamber, from a reservoir that was attached outside the main structure. A light weight ring shaped polycarbonate piston separated the low-pressure channel from the high pressure driver, see in Fig. 5.43. Its quick movement served as replacement of a diaphragm rupturing mechanism. The light weight piston was backed up with a high-pressure auxiliary helium from behind. Its quick movement served as effectively released the high pressure helium into the low pressure channel eventually forming an annular co-axial shaped shock wave. Therefore, this diaphragm-less shock tube produced annular co-axial shock waves associated with a minimal degree of disturbances.

This shock tube system had no inherent mode number and even produced mode number zero, that is $m = 0$. The only possibly created inherited disturbances in this shock tube would be those associated with the wavelets induced by the shock wave diffracting at the corner and reflecting from the 90° bend.

To control mode numbers, disturbances created by the insertions of 2, 3, 4, 6, 8, 12 and 24 pieces of 10 mm long and 10 mm diameter cylinders were examined.

The disturbances generated by small cylinders positioned in equal circumference at the 20 mm distance before the 90° corner resulted in evenly deformed converging cylindrical shock wave.

Watanabe (1993) used his vertical shock tube shown in Fig. 5.43 and observed converging shock waves exposed to the mode four perturbations. He measured the deviation of local radius Δr from the averaged diameter R and as discussed in Fig. 5.42 obtained the growth of perturbed wave shape for $Ms = 2.0$ in air with decreasing the averaged radius at 12.0, 5.7, and 3.0 mm. Figure 5.3 summarized the results for $Ms = 2.0$ in air. The ordinate denotes $\Delta r/R$ and the abscissa denotes the angles in circumference of the circular shock wave from 0 to 2π in radian.

Figure 5.44a shows the distribution of perturbed shock wave at $R = 12$ mm. The four coherent distribution of maximal peaks shows the converging shock is perturbed by the mode-four disturbances. In Fig. 5.43b, the mode-four disturbance was amplified. However, the mode-four disturbance never reached to a catastrophic amplitude; it was suppressed by introduction of the formation of triple points. Previously very densely populated fringe distribution was never maintained continuously but formed a triple point and, in short, a SMR was formed. In Fig. 5.44c, the increase in $\Delta r/R$ resulted in the formation of the triple points. The plateaus in Fig. 5.44c indicated the appearance of Mach stems.

Figure 5.45 shows results of pressure measurements along the test section shown in Fig. 2.43. Pressure transducers Kistler model 603B were distributed along the test section at the radii of 0, 15 mm, 30, and 45 mm. The experiments were conducted in the same initial condition for $Ms = 1.50$ as shown Fig. 5.44. The ordinate denoted the dimension-less pressure, p/p_o , where p_o is atmospheric pressure. The abscissa denotes the elapsed time in μs . Open circles show the measured pressures. Solid lines indicate the results of a numerical simulation solving the Navier-Stokes Equations (Watanabe 1993). Numerical results agree reasonably well with measured pressures. The time variation of pressure at the center ($R = 0$ mm) indicated that when the shock wave converged the pressure exponentially reached maximal value. The pressure jump across the converging shock waves measured at $R = 15$ mm, 30 mm and 45 mm increased linearly toward the center. However, the pressure increased exponentially toward the center.

Immediately after convergence, the converged shock wave turned into a diverging shock wave. The peak pressure started to decrease. Then the diverging shock wave was reflected from the 90° bend and its reflected shock propagated in the reverse direction and converged again at the center. The pressure spikes at the center following the first maximal pressure were caused by these waves.

5.7.2.1 Mode 0

Figure 5.46 shows the evolution of a converging shock wave of $m = 0$ for $Ms = 1.50$ in atmospheric air at 289.0 K. The shock waves were not perturbed and converged toward the center as seen in Fig. 5.46a–c. It was noticed that while

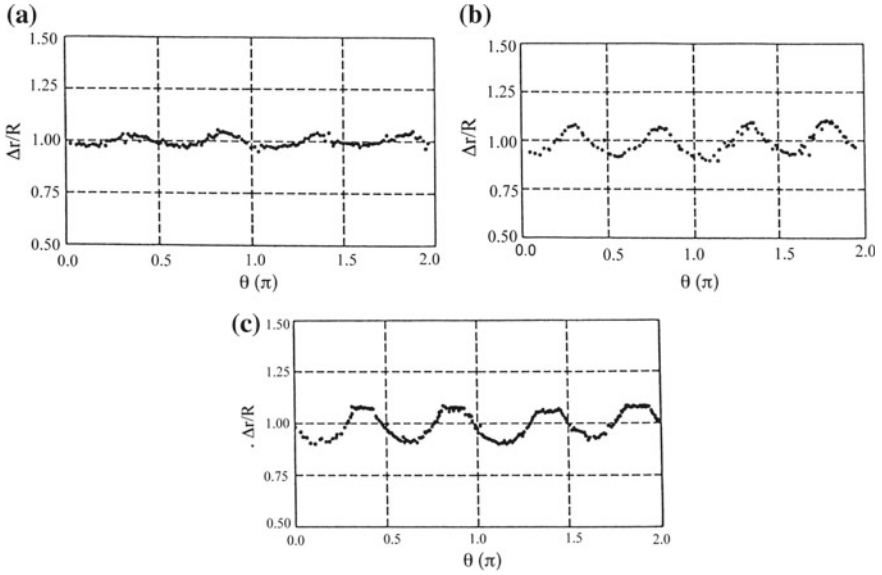
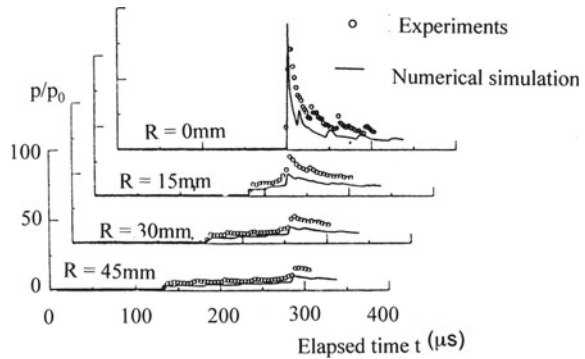


Fig. 5.44 The formation of mach reflections during the shock wave convergence for $M_s = 2.0$ in air, refer to Fig. 5.39: **a** $R = 12.0$ mm; **b** $R = 5.7$ mm; **c** $R = 3.0$ mm (Watanabe 1993)

Fig. 5.45 Time variation of pressures measured at $R = 0, 15, 30,$ and 45 mm for $M_s = 1.50$ in atmospheric air at 289.0 K referred from Fig. 5.43 (Watanabe 1993)



converging, concentric fringes appeared and gradually increased in their number increases. The test section was designed similarly to that in the horizontal shock tube and its interval was exactly set $10.0 \text{ mm} \pm 0.01 \text{ mm}$. However, the outside wall of the the test section was not rigidly fixed to the main shock tube structure. When the converging shock wave was focused in the test section and the high pressure was maintained for a short time, say for $100 \mu\text{s}$, the interval of the test section would be widened very slightly, probably the width of the laser beam wave length. The first exposure was conducted at long time before the arrival of the shock wave at the test section and the second exposure was conducted when the shock

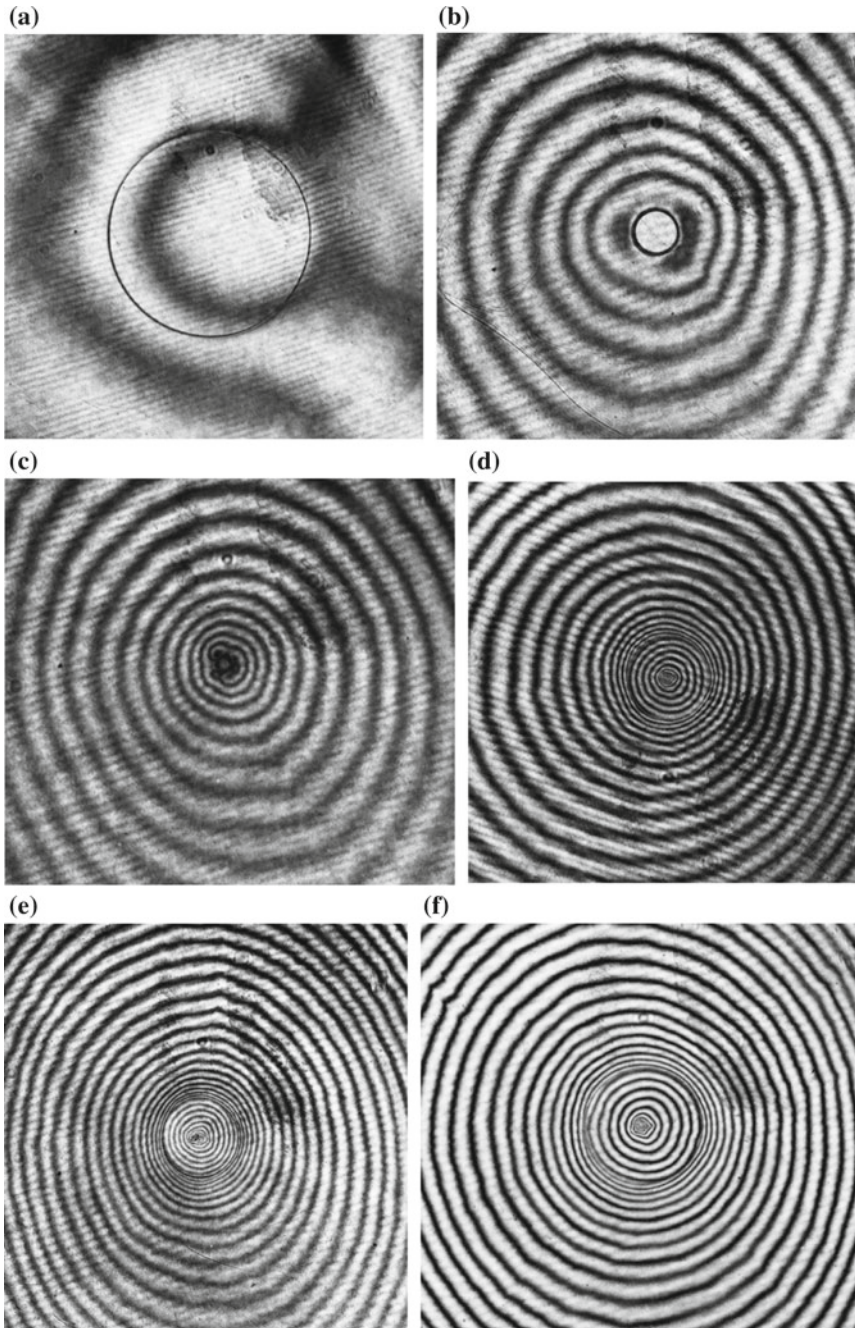


Fig. 5.46 The evolution of an annular co-axial shock wave in a vertical shock tube for $M_s = 1.50$ in atmospheric air at 289.0 K, $m = 0$: **a** #92112908 $M_s = 1.53$; **b** #92112902, $M_s = 1.52$; **c** #92112906, $M_s = 1.54$; **d** #92112802, $M_s = 1.57$; **e** #92112903, $M_s = 1.54$; **f** #92112805, $M_s = 1.53$; **g** enlargement of (**f**)

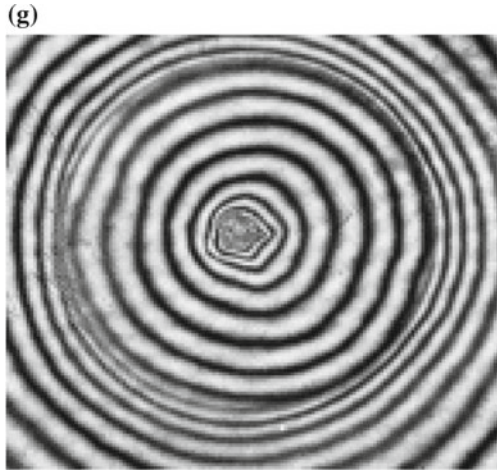


Fig. 5.46 (continued)

wave converged inside the test section. Then the change in the phase angle created the undesired co-axial fringes.

This effect would be a drawback of the present vertical shock tube. In order to overcome this drawback the outer wall should be made of massive metal frame and should be supported by an independent mechanism of the vertical channel. Anyway since the time variation in the fringe number was measurable, in the future experiments, the fringes thus created due to the out wall deformation would be deleted by introducing computer assisted image processing systems.

In Fig. 5.46d, e, the converging shock wave was supposed to converge in the absence of without creating any initial disturbances. So far during the observation until very last stage of the convergence, the fringe patterns looked symmetrical. However, Fig. 5.46f showed that the fringes just behind the diverging shock wave showed asymmetry. Figure 5.46g shows its enlargement. Although a symmetric fringe distribution was observed, the convergence of the shock wave having the mode zero may not be an easy task to achieve.

5.7.2.2 Mode 2

Figure 5.47 shows the convergence of the shock wave having mode two ($m = 2$) disturbance for $M_s = 1.50$ in atmospheric air at 290.0 K. Figure 5.47e shows the enlargement of Fig. 5.47d.

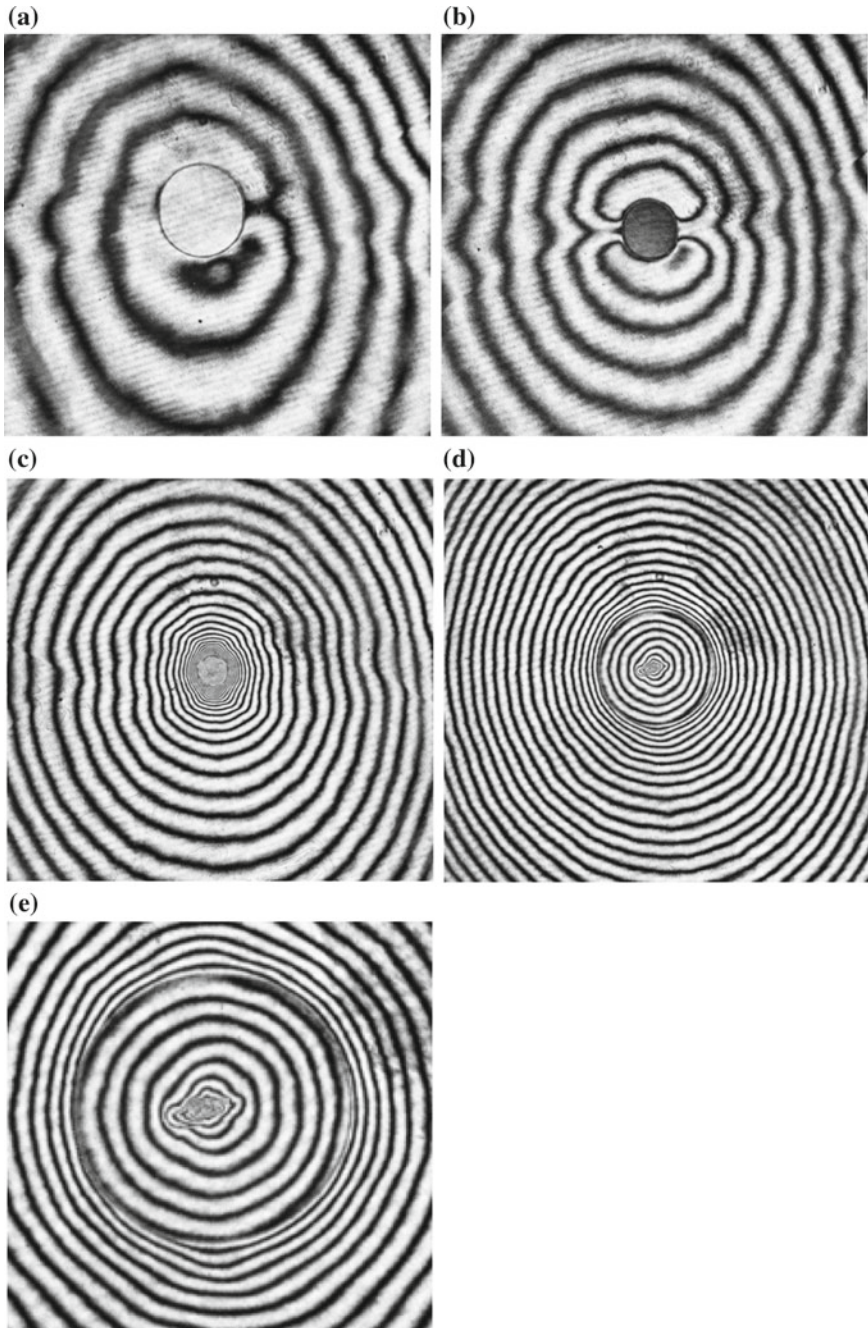


Fig. 5.47 The evolution of converging shock waves having $m = 2$ for $M_s = 1.50$ in atmospheric air at 290.0 K: **a** #92112917 $M_s = 1.53$; **b** #92112914 $M_s = 1.54$; **c** #92112912 $M_s = 1.55$; **d** #92112909, $M_s = 1.55$; **e** enlargement of (d)

5.7.2.3 Mode 3

Figure 5.48 shows the evolution of converging shock wave having $m = 3$ for $M_s = 1.59$ in atmospheric air 290.0 K.

5.7.2.4 Mode 4

Figure 5.49 shows the evolution of converging shock wave having $m = 4$ for $M_s = 1.50$ in atmospheric air 290.0 K. Figure 5.49e shows the enlargement of Fig. 5.49d. Behind the diverging shock wave, the four pairs of vortices were observed.

5.7.2.5 Mode 6

Figure 5.50 shows the evolution of converging shock wave having $m = 6$ for $M_s = 1.50$ in atmospheric air 290.0 K. Figure 5.50e shows the enlargement of Fig. 5.50d. Behind the diverging shock wave, the irregularly shaped remnant of vortices were observed.

5.7.2.6 Mode 8

Figure 5.51 shows the evolution of converging shock wave having $m = 8$ for $M_s = 1.50$ in atmospheric air. It should be noticed that the speed of shock front perturbations differs depending on the mode number. The results will be summarized in Fig. 5.54.

5.7.2.7 Mode 12

Figure 5.52 shows the evolution of the converging shock waves having $m = 12$ for $M_s = 1.50$ in atmospheric air at 290.0 K.

5.7.2.8 Mode 24

Figure 5.53 shows the evolution of the converging shock waves having $m = 24$ for $M_s = 1.50$ in atmospheric air at 290.0 K.

Figure 5.54 summarizes the results from the interferometric observations shown in Figs. 5.46, 5.47, 5.48, 5.49, 5.50, 5.51, 5.52 and 5.53. Variations of the deviated radius of the converging shock waves, Δr from the averaged radius R are measured and normalized by the R for the mode numbers $m = 2, 4, 8, 12,$ and 24 . The ordinate denotes $\Delta r/R$ and the abscissa denotes the radius R in mm. Red filled

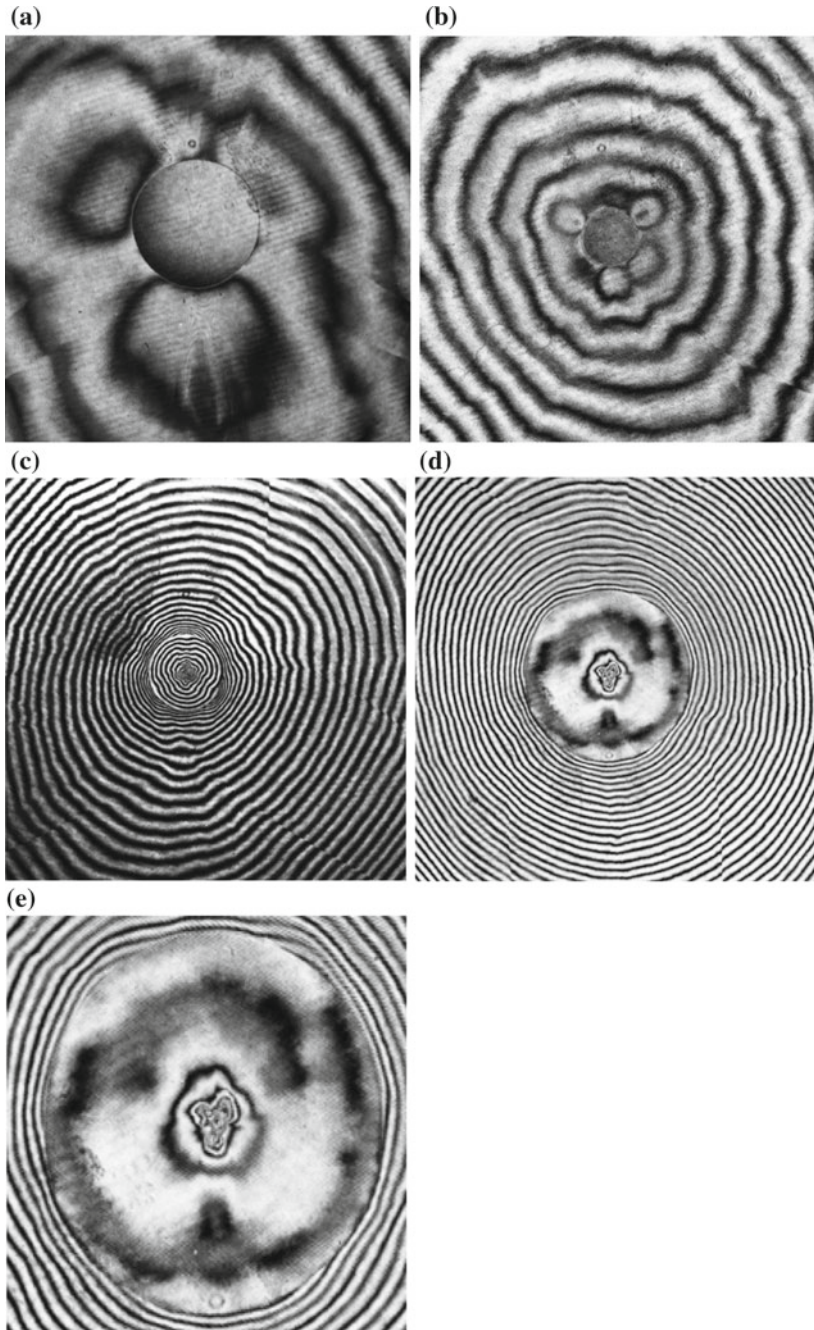


Fig. 5.48 The evolution of converging shock waves having $m = 3$ for $M_s = 1.59$ in atmospheric air 290.0 K: **a** #92120107, $M_s = 1.51$; **b** #92120212, $M_s = 1.51$; **c** #92120109, $M_s = 1.53$; **d** #92120118, $M_s = 1.54$; **e** enlargement of (d)

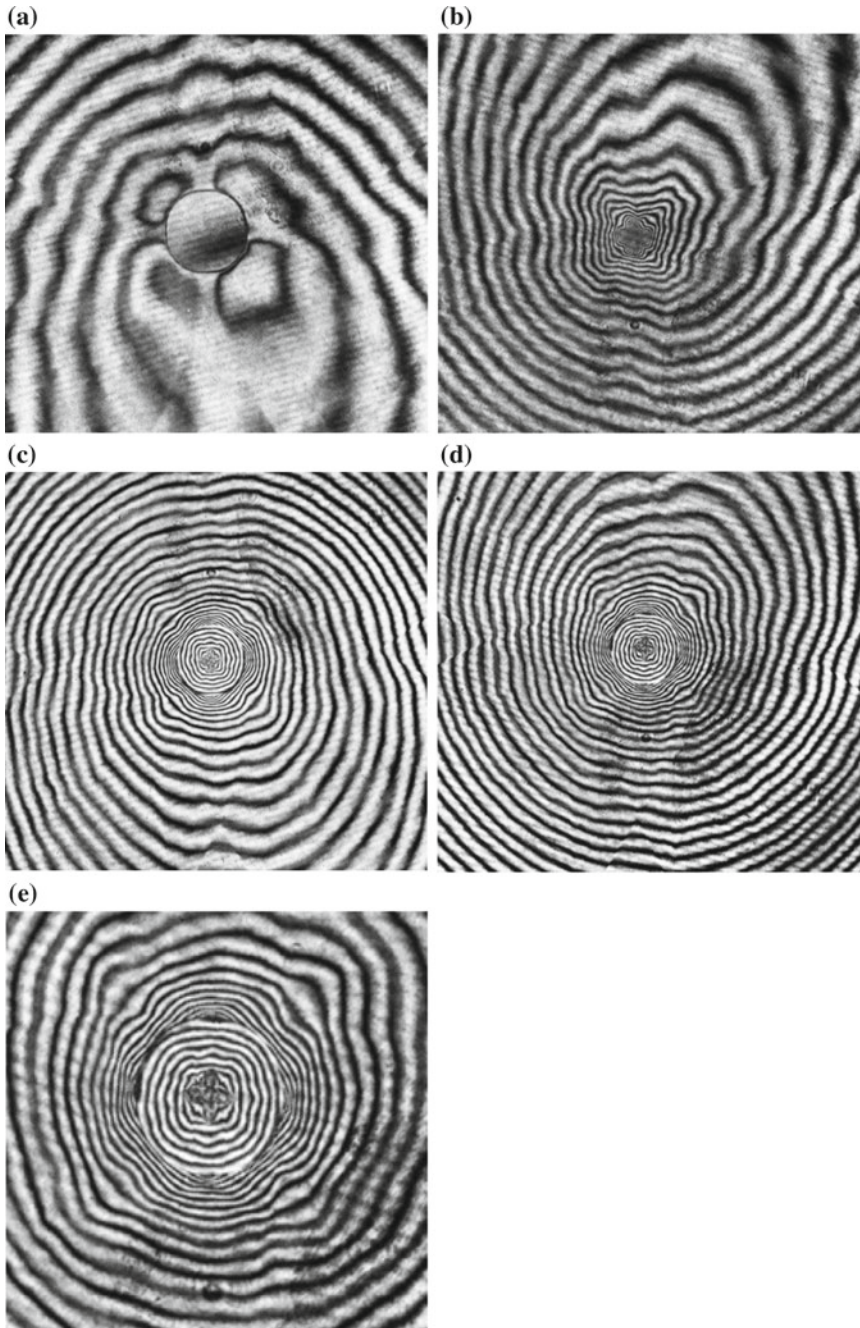


Fig. 5.49 The evolution of converging shock waves having $m = 4$ for $M_s = 1.50$ $m = 4$, in atmospheric air at 290.0 K: **a** #92112925 $M_s = 1.55$; **b** #92112924 $M_s = 1.53$; **c** #92112922 $M_s = 1.55$; **d** #92112923 $M_s = 1.55$; **e** enlargement of (d)

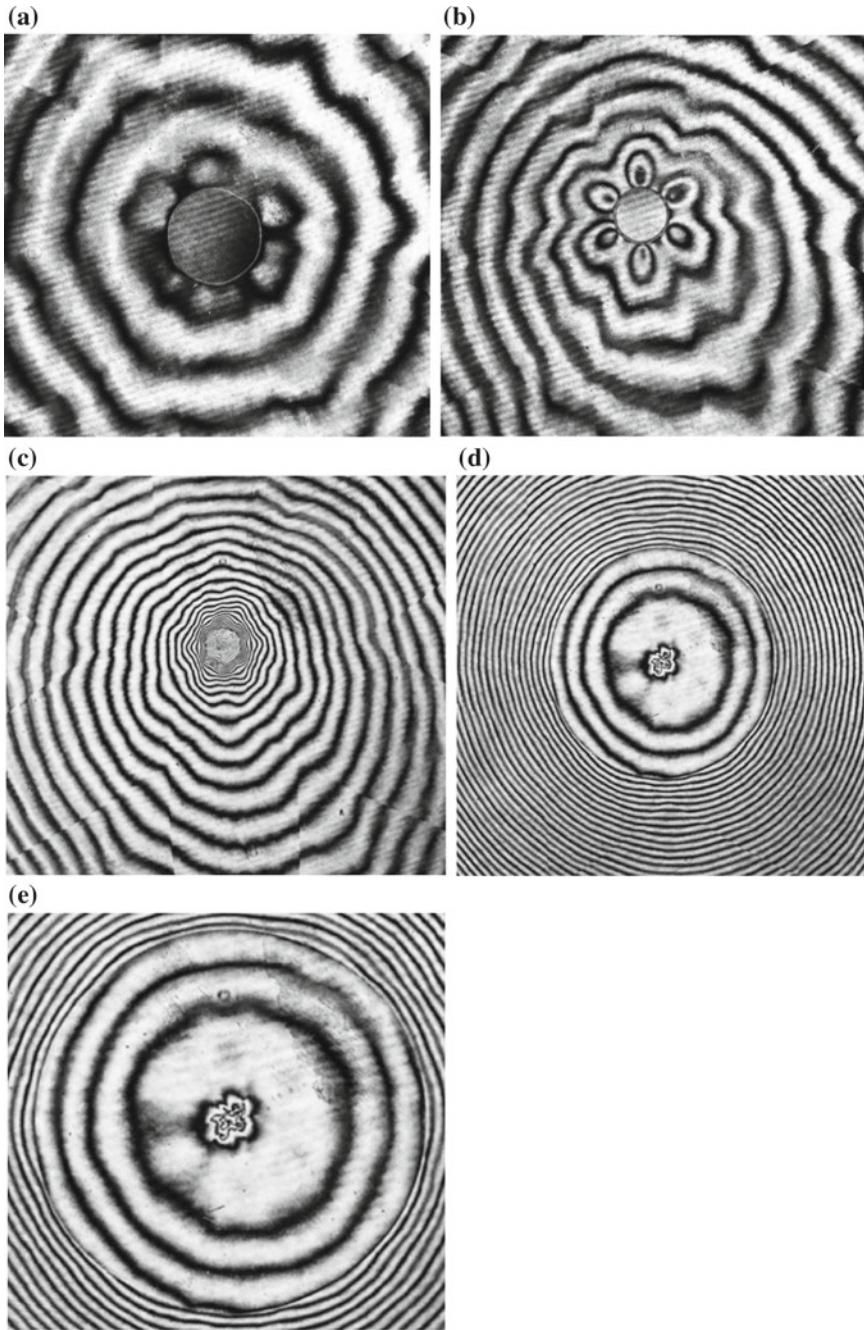


Fig. 5.50 The evolution of the converging shock waves having $m = 6$, for $M_s = 1.50$ in atmospheric air at 290.0 K: **a** #92113028, $M_s = 1.52$; **b** #92113027, $M_s = 1.56$; **c** #92113019, $M_s = 1.54$; **d** #92113023, $M_s = 1.57$; **e** enlargement of (d)

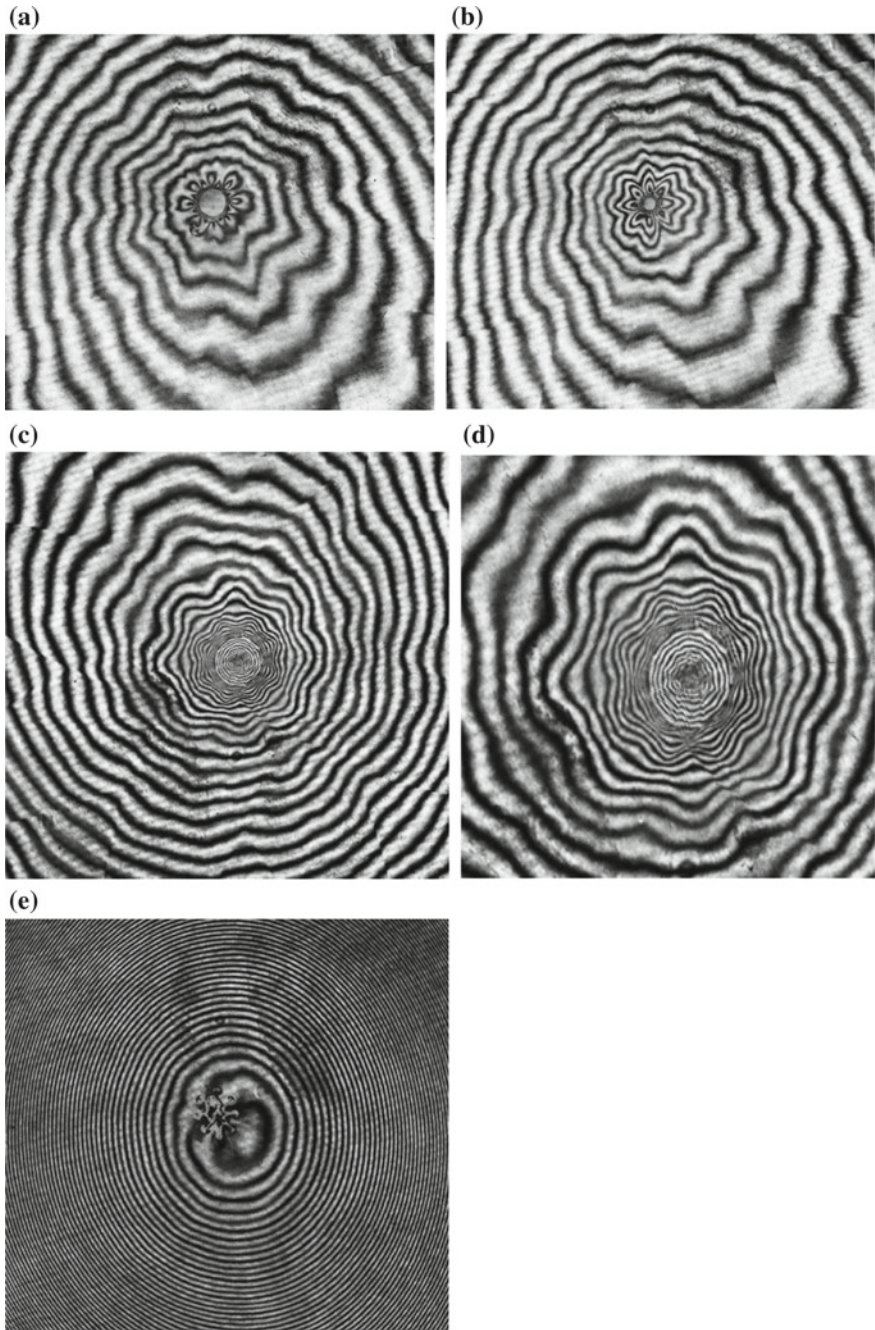


Fig. 5.51 The evolution of the converging shock waves having $m = 8$ for $M_s = 1.50$ in atmospheric air at 290.0 K: **a** #92112935, $M_s = 1.54$; **b** #92112932, $M_s = 1.53$; **c** #92112930, $M_s = 1.52$; **d** enlargement of (c); **e** #92112929, $M_s = 1.67$

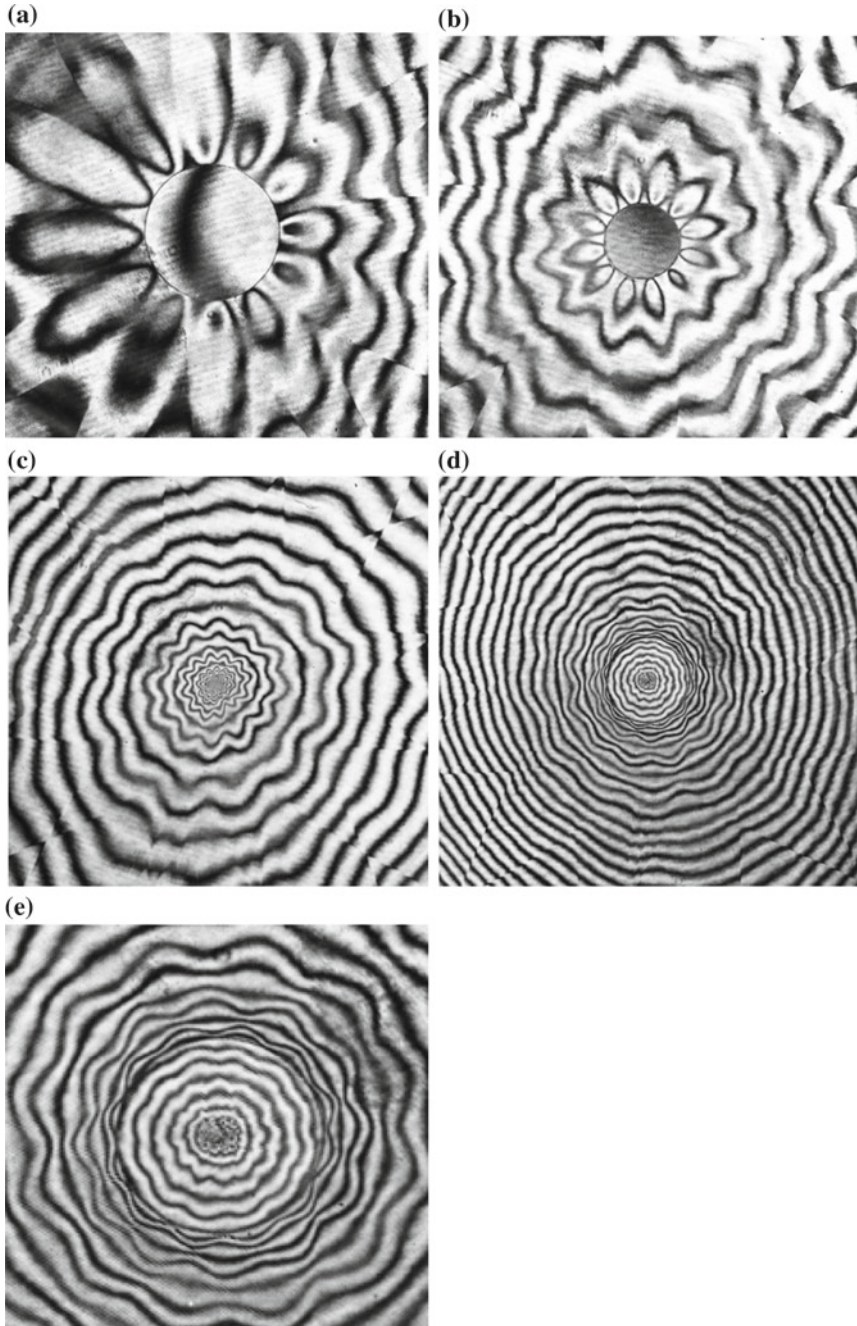


Fig. 5.52 The evolution of the converging shock waves $m = 12$ for $M_s = 1.50$ in atmospheric air at 290.0 K: **a** #92113010, $M_s = 1.52$; **b** #92113009, $M_s = 1.60$; **c** #92113016, $M_s = 1.53$; **d** #92113015, $M_s = 1.53$; **e** enlargement of (d)

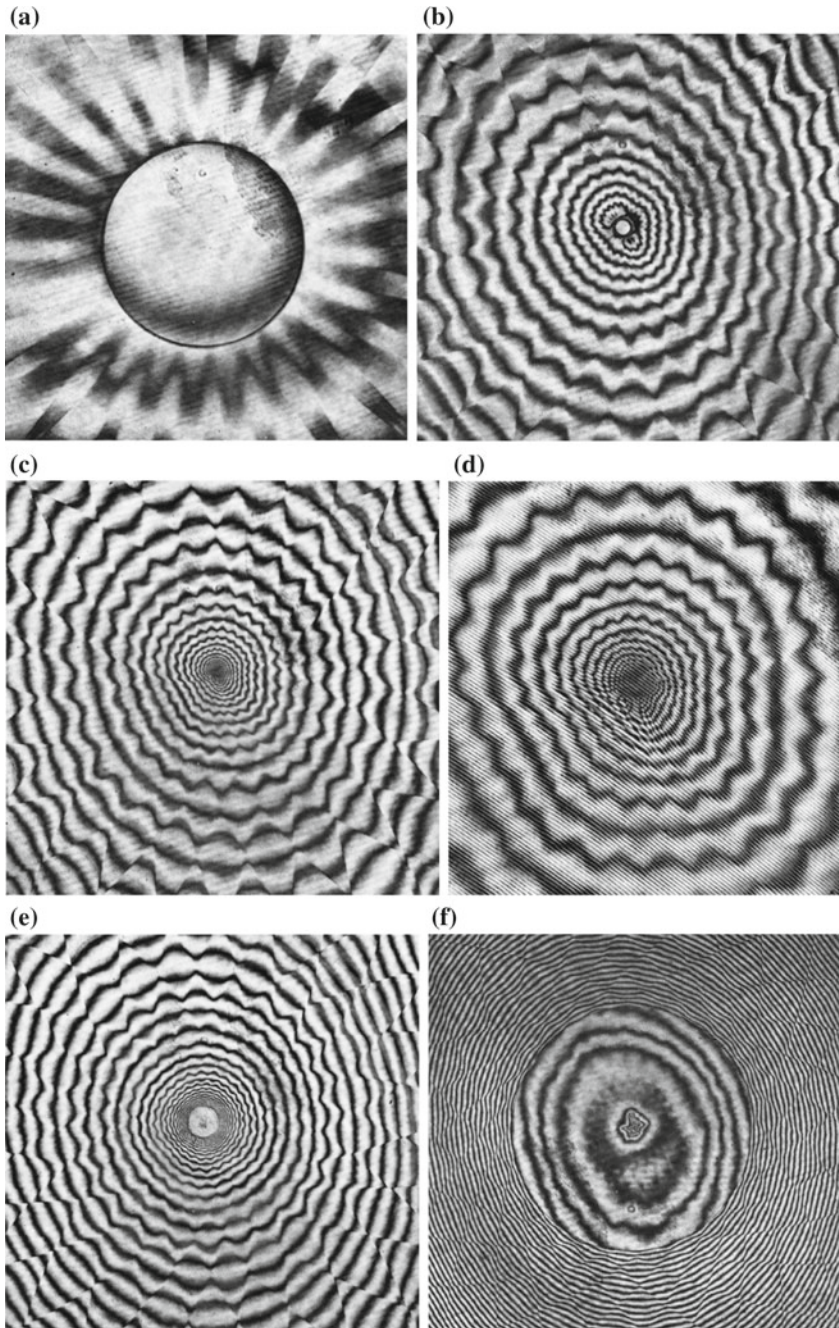


Fig. 5.53 Evolution of converging shock waves having $m = 24$ for $M_s = 1.50$ $m = 24$, in air at 1013 hPa, 290.0 K: **a** #92112937 $M_s = 1.52$; **b** #92113007 $M_s = 1.53$; **c** #92113003 $M_s = 1.53$; **d** enlargement of (c); **e** #92113004 $M_s = 1.52$; **f** #92113005 $M_s = 1.53$

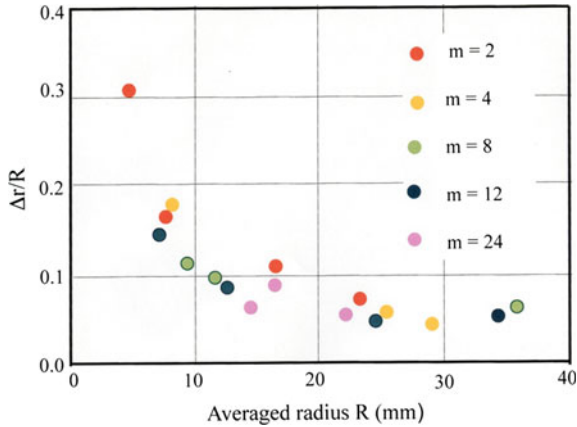


Fig. 5.54 Growth of converging shock wave deformation along radius for $M_s = 1.50$ (Watanabe 1993)

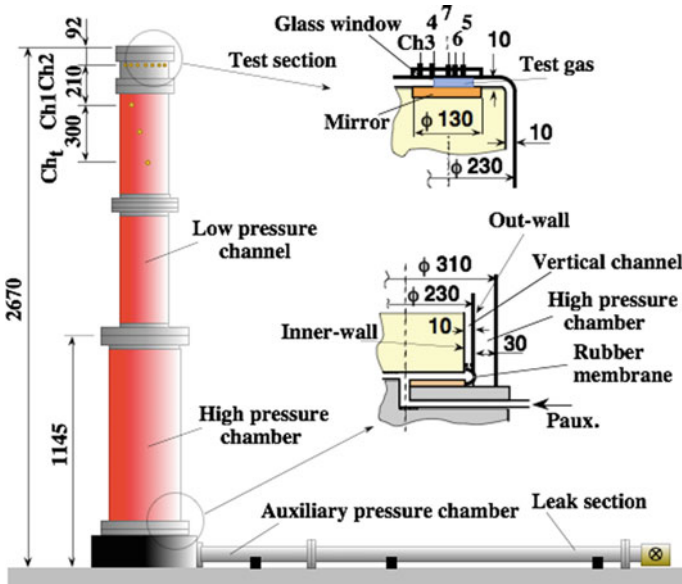


Fig. 5.55 A second generation vertical shock tube in which a rubber membrane serves as a moving diaphragm (Hosseini et al. 1997)

circles refer to $m = 2$, pink filled circles refer to $m = 4$, green filled circles refer to $m = 8$, dark blue filled circles refer to $m = 12$, and pale pink filled circles refer to $m = 24$. In general, the smaller the mode number is, the larger $\Delta r/R$ becomes while approaching toward the center of convergence. In the case of $m = 24$, the remnant of the vortices at the center as seen Fig. 5.53e, is smaller than that seen in the case

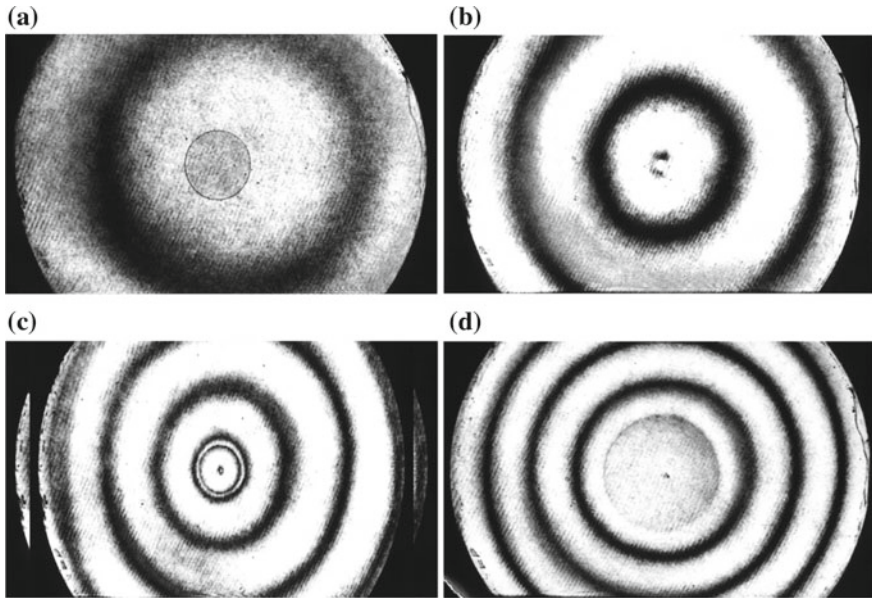


Fig. 5.56 the evolution of the converging shock wave having $m = 0$ for $M_s = 1.50$ $m = 0$ in atmospheric air: **a** 322 μs from trigger time; **b** 332 μs ; **c** 342 μs ; **d** 363 μs , (Hosseini et al. 1997)

of $m = 6$, seen in Fig. 5.50e. This indicates that the deformation $\Delta r/R$ induced by individual mode numbers increases differently. The deformation induced by the larger m develops relatively slowly. This observation empirically agreed with Terao's observation (1973) that the detonation waves converged in a very stable manner. The detonation wave had many cellular structures distributed on its surface, this means that the mode number of the disturbances are numerous.

5.7.3 Vertical Annular Co-axial Diaphragm-Less Shock Tube

Figure 5.55 shows the second generation annular co-axial vertical shock tube constructed in late 1990s. The first generation vertical shock tube shown in Fig. 5.43 successfully eliminated mode number four, which was inherited in the horizontal structure. However, the vertical structure was so delicately designed that unexpected co-axial fringes were generated. Hence, the second generation vertical shock tube had a massive base and was supported rigidly. The high pressure driver chamber and the low pressure channel were sealed with a ring shaped rubber membrane which was a replacement of the polycarbonate ring shaped piston used in Fig. 5.43. The membrane was bulged loading with auxiliary high pressure helium from the other side. Upon the sudden release of the auxiliary helium, the rubber

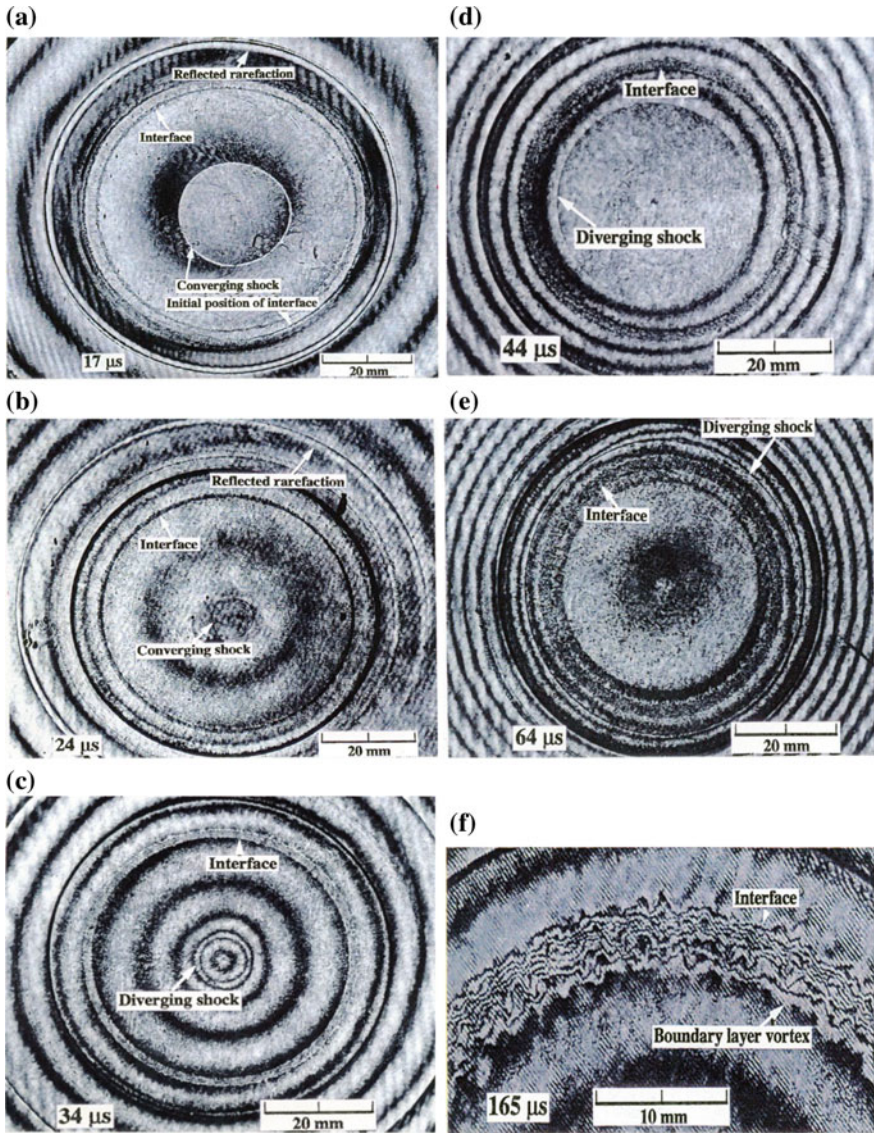


Fig. 5.57 Converging shock wave interaction with helium column for $Ms = 1.21$ in atmospheric air in helium at 1017.8 hPa: **a** 17 μs ; **b** 24 μs ; **c** 34 μs ; **d** 44 μs ; **e** 64 μs ; **f** 165 μs . Enlarged view (Hosseini et al. 1997)

membrane shrank discharging the driver gas instantaneously into the channel. The annular co-axial shock wave was built up while propagating along the channel, turned 90° at the corner, and became a converging shock wave. The increase in number of fringes induced by the movement of the upper wall was minimized.

Nevertheless, this shock tube experienced slight vibrations during its operation at high pressures. Then the attainable shock wave Mach number, M_s was 2.5 in air. The optical arrangement was similar to the Twyman-Greene interferometry applied already in the previously described vertical shock tube shown in Fig. 5.43.

Figure 5.55 shows the evolution of converging shock wave using the vertical shock tube shown in Fig. 5.54 having mode number zero, $m = 0$, for $M_s = 1.50$ $m = 0$ in air. Figure 5.55a, b show perfectly cylindrical shock wave converges. Any signs of asymmetric wavelets were observed. At later stage in Fig. 5.55c, d, during the shock wave convergence and reflection a small dark spot was observed behind the diverging shock wave in Fig. 5.55c. This is a remnant of a density concentration occurred at $342 \mu\text{s}$ from trigger point. In Fig. 5.55d after $21 \mu\text{s}$ from Fig. 5.55c, the sign of the density concentration became faint. The diameter of the density concentration was very localized. Anyway the shock wave focused nearly perfectly at the center (Fig. 5.56).

5.7.3.1 Concentric Helium Column

Figure 5.57 shows the interaction of converging shock wave ($M_s = 1.21$) in atmospheric air with a 50 mm diameter helium column placed in a concentric position. The helium column was made by blowing a soap column with slightly pressurized helium at 1017.8 hPa.

When the converging shock wave impinged on the helium column, a shock wave was transmitted into the helium and an expansion wave was reflection from the helium interface as seen in Fig. 5.57a, b. The transmitted shock wave converged and became a diverging shock wave in Fig. 5.57c, d. The interface is gradually broadened with elapsed time. At the convergence early time, a remnant of density peak was still observable in Fig. 5.57e. Figure 5.57f shows a magnified view at later stage. The broadened interface did not show two-dimensional jagged surface but three-dimensionally deformed interface. This experiment motivates investigating the Richtmyer-Meshkov instability. The time attached to each picture indicates the elapsed time from the moment of the shock wave impingement on the helium column.

5.7.3.2 Eccentric Helium Column

For investigating the Richtmyer-Meshkov instability, a series of experiments were conducted using a vertical shock tube (Hosseini et al. 1997). Figure 5.58 shows the experimental arrangement of a converging shock wave interaction with a helium column positioned in an eccentric position. The helium column was produced in the same way as seen in Fig. 5.57.

Figure 5.59 shows 50 mm diameter helium column impinged by a converging shock wave of $M_s = 1.18$ in atmospheric air. The acoustic impedance in air is 2.5 times as larger as that in pure helium. Although the helium column was

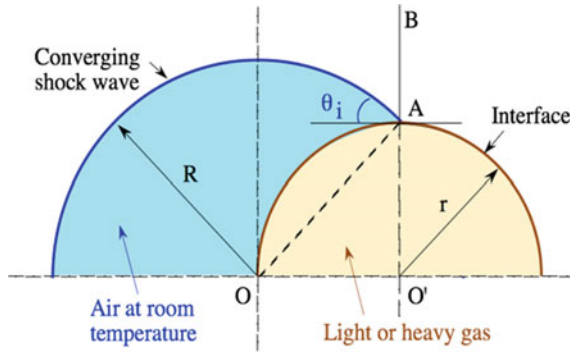


Fig. 5.58 Illustration of shock wave helium column interaction

contaminated by air presumably in at most 20% in volume, the weak shock waves in are reflected wave from the air/helium interface as an expansion wave and the transmitting wave in helium is as a shock wave. Hence the transmitted sock wave in helium is going to converge. Figure 5.59a shows a wave pattern at 30 μs after the impingement of converging shock wave with the helium column. Figure 5.59b shows its enlargement. Figure 5.59e shows a wave pattern at 75 μs after the shock wave impingement. The downstream side of the helium column moved to the center of convergence. At the same time, the helium interface contracts and its center slowly moves toward the center of the convergence. The transmitting shock wave in helium came out of the interface and going to converge. Hence at 177 μs, complex wave interactions occur simultaneously.

5.7.3.3 Focusing of a Transmitted Shock Wave Diffracting Over a Backward Facing Wall

In order to achieve a stable convergence, another compact vertical annular co-axial diaphragm-less shock tube was constructed. Its photograph is presented in Fig. 5.60a, b. A rubber membrane was used for sealing the driver gas and the test gas. In this revised shock tube, the rubber membrane simply moved up and down between two curved grids as illustrated in Fig. 5.60a. Auxiliary high pressure helium bulged the rubber membrane making it attach tightly onto the upper grid. Then the test gas was sealed completely from the driver gas. When the auxiliary gas was quickly reduced, the membrane left from the upper grid and moved onto the lower grid. Meantime the high pressure driver gas rushed vertically into the low pressure channel. The space between two grids was wide enough to minimize pressure losses that usually occur at the diaphragm section of conventional shock tube. Figure 5.60b shows a photograph of the compact vertical shock tube. The exit was coated with fluoresce paint in order to conduct diffuse holographic observation. The height of the low pressure channel was about 1 m.

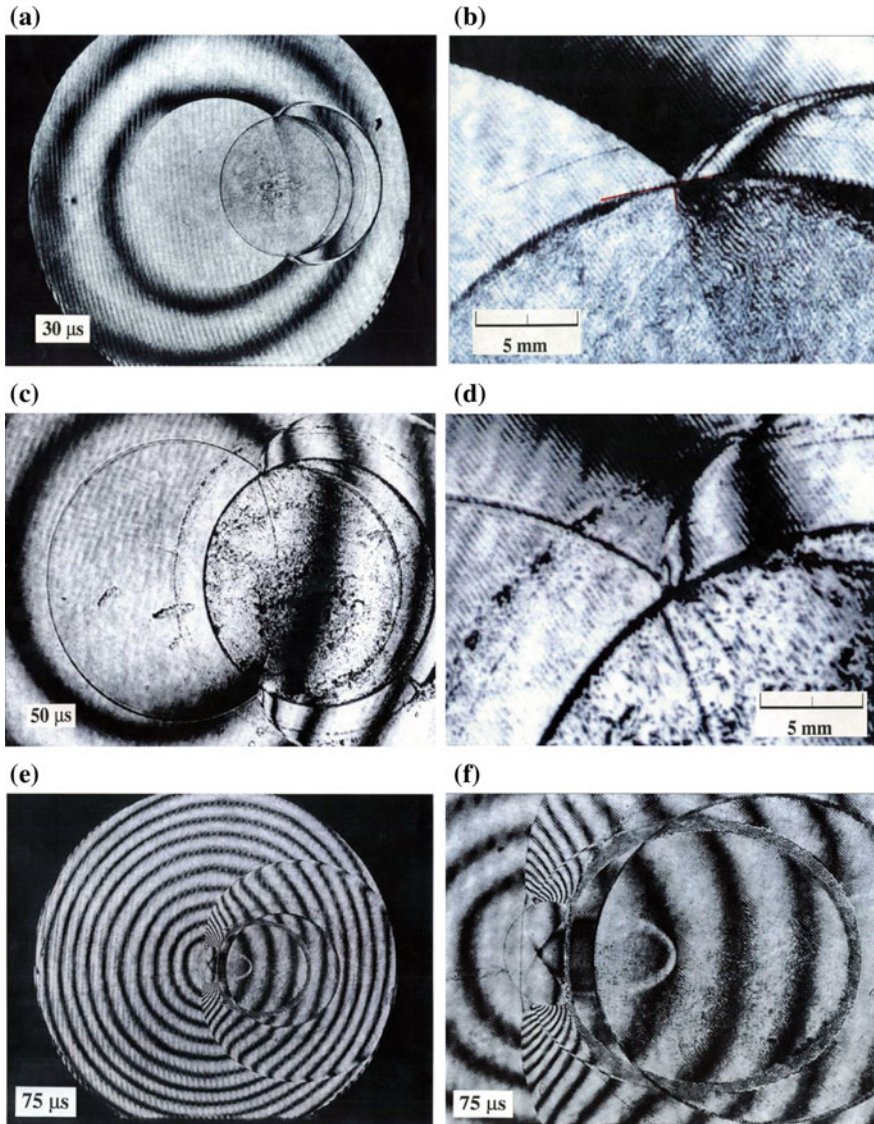


Fig. 5.59 The evolution of the converging shock wave interaction with 50 mm diameter helium soap bubble, $M_s = 1.18$ in atmospheric air: **a** 30 μ s after impingement; **b** enlargement of (a); **c** 50 μ s; **d** enlargement of (c); **e** 75 μ s; **f** enlargement of (e); **g** 177 μ s; **h** 345 μ s

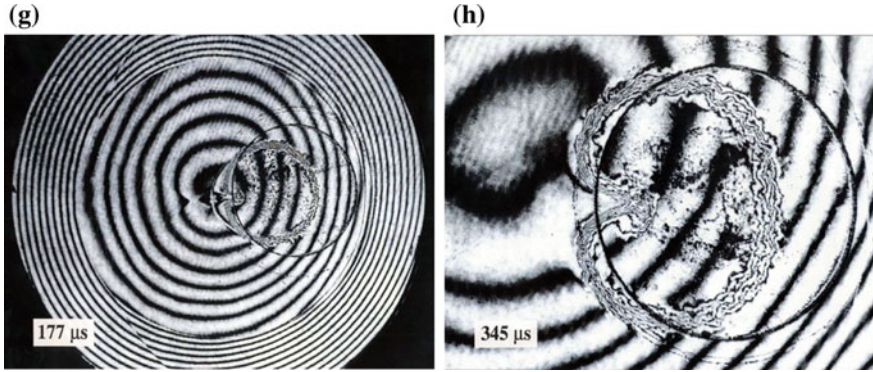


Fig. 5.59 (continued)

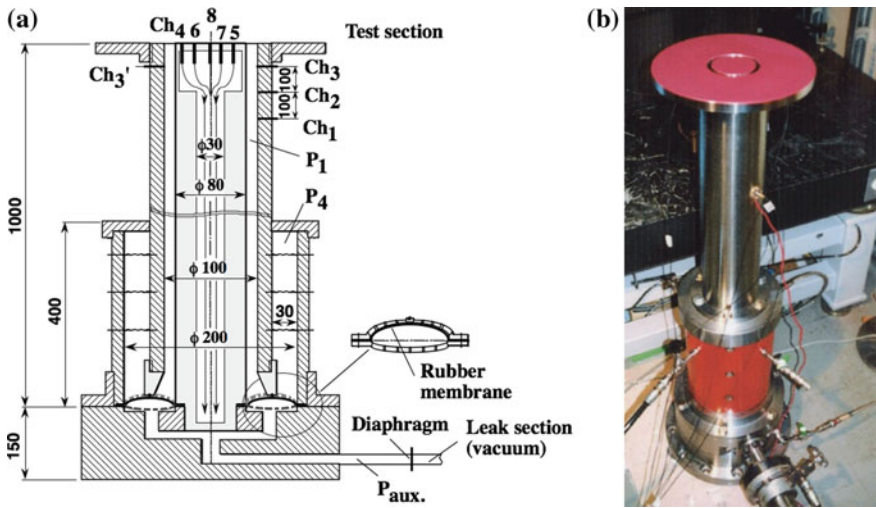


Fig. 5.60 Compact vertical annular shock tube and test section: **a** 80 mm × 100 mm vertical shock tube; **b** Photo of the vertical shock tube (Hosseini et al. 1999)

Figure 5.61 shows characteristic performance of the compact vertical shock tube. The ordinate denotes dimension-less high pressure. The abscissa denotes M_s measured at the end of the low pressure channel. A red broken line denotes numerical results obtained from the simple shock tube theory Gaydon and Hurlle (1963). Black filled circles denote measured M_s . In a relatively limited range of M_s , an excellent agreement between the results is evident in Fig. 5.61 (Hosseini et al. 1999).

Figure 5.62 shows the propagation of the shock wave released from a 10 mm wide ring shaped opening into a 100 mm diameter cylindrical tube. Figure 5.62a, b shows the experimental arrangement and the aspheric lens shaped test section.

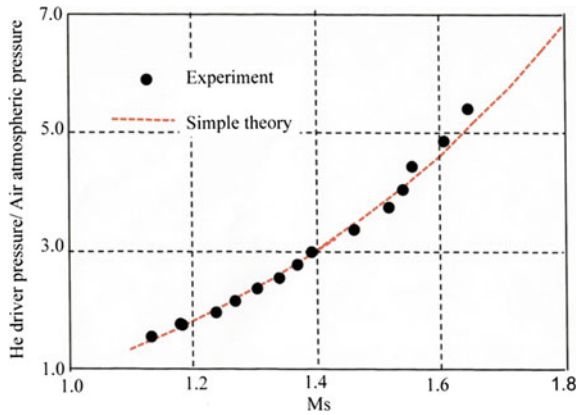


Fig. 5.61 Performance of the vertical compact shock tube shown in Fig. 5.59a (Hosseini et al. 1999)

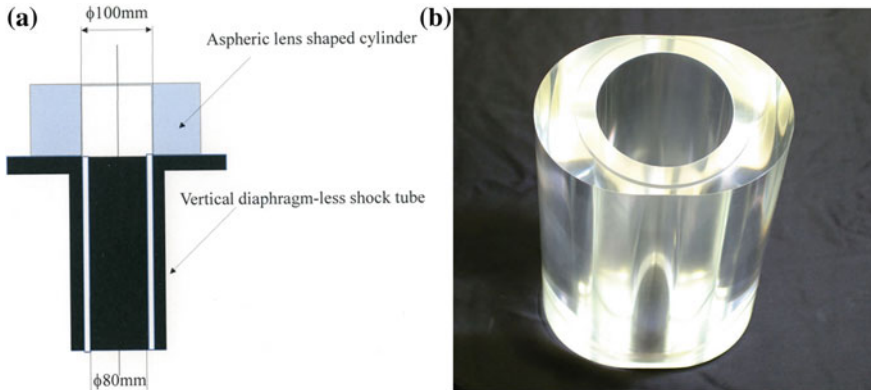


Fig. 5.62 Shock wave focusing released from a 10 mm ring shaped opening shown in Fig. 5.59b: **a** experimental arrangement; **b** 100 mm diameter aspheric lens (Hosseini et al. 1999)

In Chap. 3, the two-dimensional shock wave diffraction over a backward facing step was discussed. Figure 5.63 shows the evolution of an axially symmetric shock wave diffracting at the backward facing step for $M_s = 1.50$ in atmospheric air. In Fig. 5.63a, the images of the transmitted shock waves were superimposed on each other resulted in complex fringe distributions. Nevertheless, the shape of a diffracting shock wave and the resulting formation of corner vortices are well resolved. The circular diffracting shock waves approached toward the center as seen in Fig. 5.62c, d. When the circular diffracting shock waves merged at the center, the angle of their merger is shallow and hence the resulting reflected shock wave pattern is a RR. With elapsed time, the angle at which the reflected shock wave merged gradually increased and the transition to a MR occurred. In Fig. 5.63f the reflection pattern is a MR.

In Chap. 3, the shock wave diffractions from openings of various shapes were visualized using diffuse holographic interferometry. As seen in Fig. 5.60b, the shock wave diffracted from a 10 mm wide circular opening composed of 100 mm outer diameter and 80 mm inner diameter would form at first a toroidal shock wave. With elapsed time, the shock wave would be a diffracting shock wave from a circular cross sectional tube at discussed in Chap. 3. However, the inner part of the toroidal shock wave would converge toward the center of the test section.

The quantitative visualization of three-dimensional shock waves is not simple. Then it was decided to apply diffuse holographic interferometry already applied to shock wave diffraction experiments already shown in Fig. 3.19. The shock tube and its flange were coated with the pink color fluorescent paint as shown in Fig. 5.60b. Then diffuse holographic observations were conducted for $M_s = 1.50$ in atmospheric air by oblique illumination over the coated area with the *OB*. The reflection of the *OB* illuminated a holographic film. The test section was obliquely illuminated twice with the diffused *OB* at appropriate time interval, then double exposure diffuse holographic interferometry was completed (Figs. 5.61, 5.62).

Figure 5.63 shows reconstructed imaged showing the motion of transmitted shock waves. Figure 5.63a shows the shock waves at $30 \mu\text{s}$ from the trigger point. This indicated the time instant at which the second exposure was conducted. The diverging shock wave marked on the photo denotes the diffracting shock wave propagating outward. The imploding SW on the photo denotes the diffracting shock wave at the inner corner and is converging toward the center of the test section, Fig. 5.63b was taken at $50 \mu\text{s}$ after the time instant when Fig. 5.63a was taken. The initial diverging shock wave propagated further outward and a secondary shock wave followed. The converging shock wave was just going to converge at the center. Another secondary shock wave appeared behind the converging shock wave. These secondary shock waves were created as transmitted shock wave was reflected from the inner and outer wall surfaces. Figure 5.63c was taken at $16 \mu\text{s}$ after the time instant when Fig. 5.63b was taken. The diverging shock wave further propagated outward. The converging shock wave and the secondary shock wave imploded. Remnants of vortices were observed at the center. Figure 5.63d shows state long time afterward. The Magnified photo show, although very blurred, the accumulation of fringes (Fig. 5.64).

5.8 Explosion Induced Shock Wave Focusing from a Truncated Ellipsoidal Reflector

An ellipsoidal cavity has two focal points. Constructing a half truncated ellipsoidal cavity, having a geometry of the inner diameter of 135 mm and outer diameter of 190 mm and the aspect ratio is $2^{1/2}$. A spherical shock wave was generated by the explosion of a 10 mg AgN_3 pellet at the first focal point inside the truncated ellipsoidal cavity. Figure 5.65 shows the experimental setup. The resulting shock

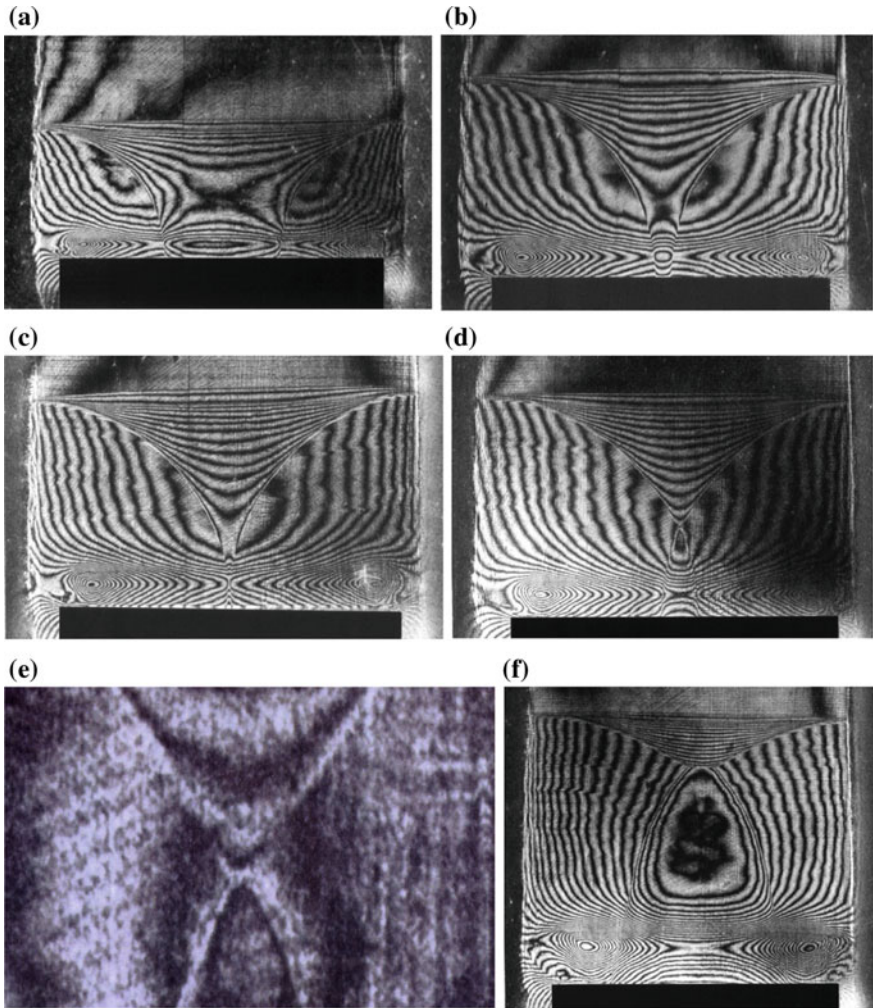


Fig. 5.63 Diffraction and convergence of a toroidal shock wave for $M_s = 1.50$ in atmospheric air: **a** 63 μs ; **b** 92 μs ; **c** 96 μs ; **d** 104 μs ; **e** enlargement of **(d)**; **f** 148 μs

wave is reflected from the truncated ellipsoidal cavity and focuses at another focal point of outside the reflector. If it is an underwater shock wave, the resulting shock wave propagates at sonic speed and then the shock wave would focus at the second focal point. However, in air the shock wave propagates at high speed as $M_s > 1$, then the shock wave will not focus sharply at the second focal point.

Figure 5.66 shows the evolution of a reflected shock wave merging at an area outside the truncated ellipsoidal cavity. The shock wave propagates from right to

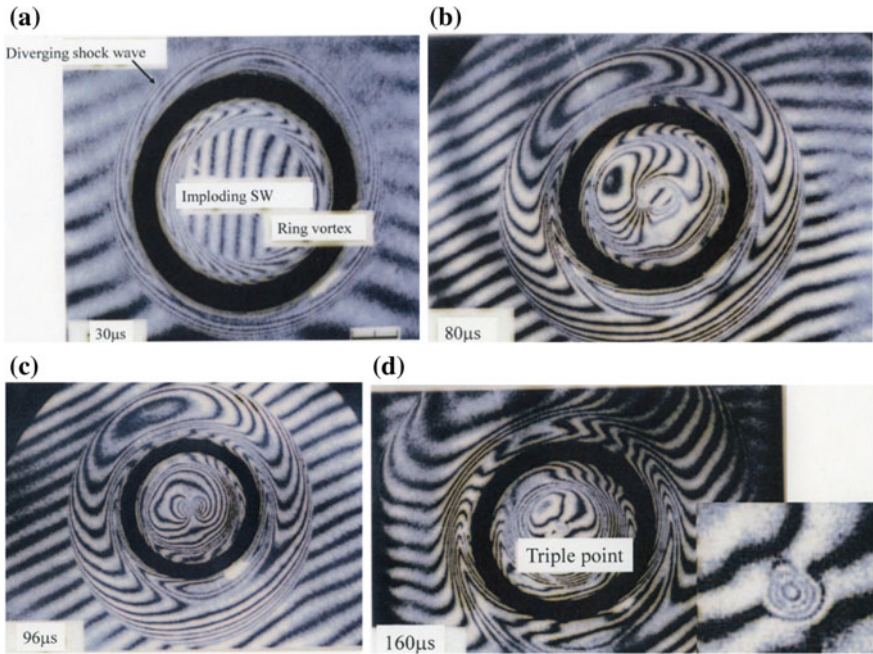


Fig. 5.64 Evolution of hemi-spherical shock wave released from a 10 mm ring shaped opening for $M_s = 1.20$ in atmospheric air: **a** 30 μs; **b** 80 μs; **c** 96 μs; **d** 160 μs

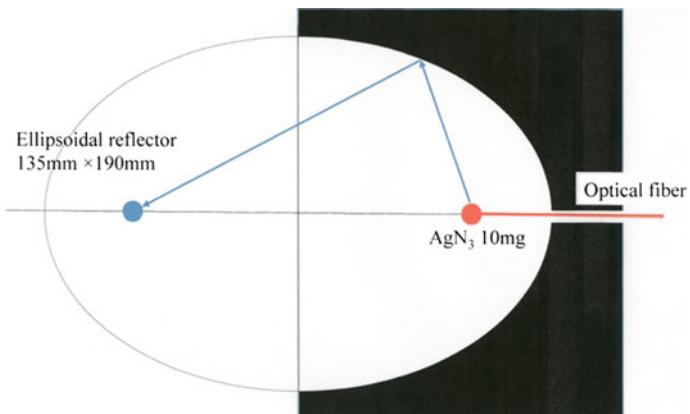


Fig. 5.65 Illustration of a spherical shock wave focusing from a truncated ellipsoidal cavity

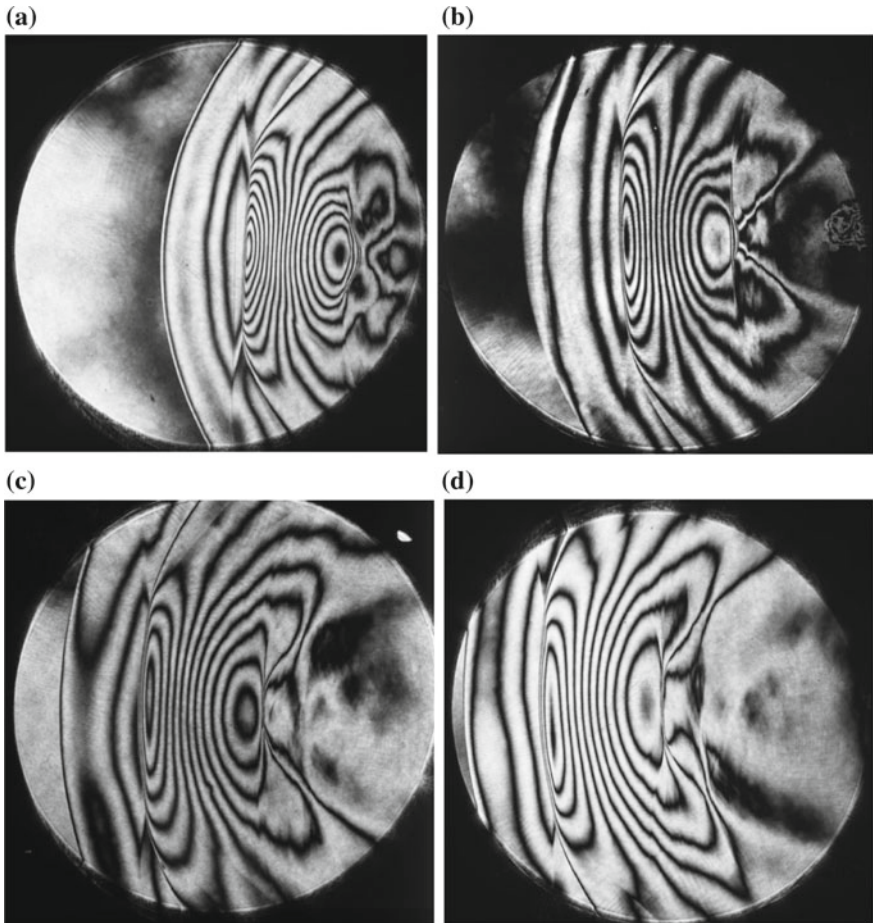


Fig. 5.66 Focusing of a spherical shock wave in air from ellipsoidal cavity, 10 mg AgN_3 in air at 294.0 K: **a** #88072508, 350 μs from trigger point; **b** #88072509, 360 μs ; **c** #88072506, 450 μs ; **d** #88072505, 500 μs

left. In Fig. 5.66a, the direct wave propagates much faster than the reflected wave. The reflection of the shock waves in air from the curved ellipsoidal cavity are very different from the shock wave reflection from the same shape of ellipsoidal cavity. Spherical incident shock waves with moderate strength in air will never reflect from ellipsoidal walls like spherical underwater shock waves. In Fig. 5.66a–d, the attenuation of the direct wave is clearly observed and very diversified patterns of fringes in the vicinity of the second focal point area.

References

- Apazidis, N., Kjellander, M., & Tillmark, N. (2011). High energy concentration by symmetric shock focusing. In: K.Kontis, (Ed.), *Proceeding of 28th International Symposium on Shock Waves* (vol. 1, pp. 99–110). Glasgow.
- Courant, R., & Friedrichs, K. O. (1948). *Supersonic flows and shock waves*. NY: Wiley Inter-Science.
- Fujiwara, T., Sugiyama, T., Mizoguchi, K., & Taki, S. (1979). Stability of converging cylindrical detonation. *Journal of the Japan Society for Aeronautical and Space Sciences*, 21, 8–14.
- Gaydon, A. G., & Hurler, I. R. (1963). *The shock tube high-temperature chemical physics*. London: Chapman and Hall Ltd.
- Guderley, G. (1942). Starke kugelige und zylindrische Verdichtungs Stoesse in der Naehة des Kugelmittelpunktes bzw. der Zylinderachse. *Luftfahrtforschung*, 19, 302–312.
- Honda, M., Takayama, K., & Onodera, O. (1977). Shock wave propagation over 90° bends, Rept Inst High Speed Mech. *Tohoku University* 35, 74–81.
- Hoshizawa, Y. (1987). *Study of converging shock wave* (Master thesis). Graduate School of Engineering, Faculty of Engineering Tohoku University.
- Hosseini, S. H. R., Takayama, K., & Onodera, O. (1999). Formation and focusing of toroidal shock waves in a vertical co-axial annular diaphragm-less shock tube. In: G. J. Ball, R. Hillier, & G. T. Robertz (Eds.), *Proceeding 22nd ISSW, Shock Waves* (vol. 2, pp. 1065–1070). London.
- Hosseini, S. H. R., Onodera, O., Falcovitz, J., & Takayama, K. (1997). Converging cylindrical shock wave in an annular strut free diaphragm-lee shock tube. In: A. F. P. Houwing & A. Paul (Eds.), *Proceeding 21st ISSW, Shock Waves* (vol. 2, pp. 1511–1516). The Great Kepple Island.
- Inoue, O., Imuta, G., Milton, B. E., & Takayama, K. (1995). Computational study of shock wave focusing in a log-spiral duct. *Shock Waves*, 5, 183–188.
- Knystaustus, R., & Lee, J. H. (1971). Experiments on the stability of converging and cylindrical detonation. *Combustion and Flame*, 16, 61–73.
- Milton, B. E. (1989). Focusing of shock waves in two-dimensional and axi-symmetric ducts. In: K. Takayama (Ed.), *Proceeding International Workshop on Shock Wave Focusing* (pp. 155–192). Sendai.
- Milton, B. E., Archer, D., & Fussey, D. E. (1975). Plane shock amplification using focusing profiles. In: G. Kamimoto (Ed.), *Proceeding 10th International Shock Tube Symposium, Modern Developments in Shock Tube Research* (pp. 348–355). Kyoto.
- Neemeh, B. A., & Less, D. T. (1990). Stability analysis of initially weak converging cylindrical shock waves, In: Y. W. Kim (Ed.), *Proceedings of the 17th International Symposium on Shock Wave, Current Topics in Shock Waves* (pp. 957–962). Bethlehem.
- Perry, R. W., & Kantrowitz, A. (1951). Production and stability of converging shock waves. *Journal of Applied Physics*, 22, 878–886.
- Sun, M. (2005). Numerical and experimental study of shock wave interaction with bodies. (Ph. D. thesis). Graduate School of Engineering, Faculty of Engineering Tohoku University.
- Sun, M., Saito, T., Takayama, K., & Tanno, H. (2005). Unsteady drag on a sphere by shock wave loading. *Shock Waves*, 14, 3–9.
- Takayama, K. (1983). Application of holographic interferometry to shock wave research. In *International Symposium of Industrial Application of Holographic Interferometry, Proceeding SPIE 298* (pp. 174–181).
- Takayama, K. (1990). Proceedings of the international workshop on shock wave focusing, Inst High Speed Mechanics, Sendai.
- Terao, K., & Sato, T. (1973). A study of a radially divergent-convergent detonation wave. In D. Bershader, & W. Griffice (Eds.), *Proceedings of the International Symposium on Shock Tube, Recent Developments in Shock Tube Research* (pp. 646–651).
- Watanabe, M. (1993). Numerical and experimental study of converging shock wave (Ph.D. thesis). Graduate School of Engineering, Faculty of Engineering Tohoku University.

- Whitham, G. B. (1959). A new approach to problems of shock dynamics. *Part II Three dimensional problems. JFM*, 5, 359–378.
- Wu, J. H. T., Neemeh, R. A., Ostrowski, P. P., & Elabdin, M. N. (1978). Production of converging cylindrical shock waves by finite element conical contractions, In: Ahlborn, B., Hertzberg, A., Russell, D. (Eds.), *Proceeding of the 11th International Symposium on Shock Tubes and Waves, Shock Tube and Shock Wave Research* (pp. 107–114). Seattle.
- Yamanaka, T. (1972). *An investigation of secondary injection of thrust vector control (in Japanese)*. NAL TR-286T. Chofu, Japan.